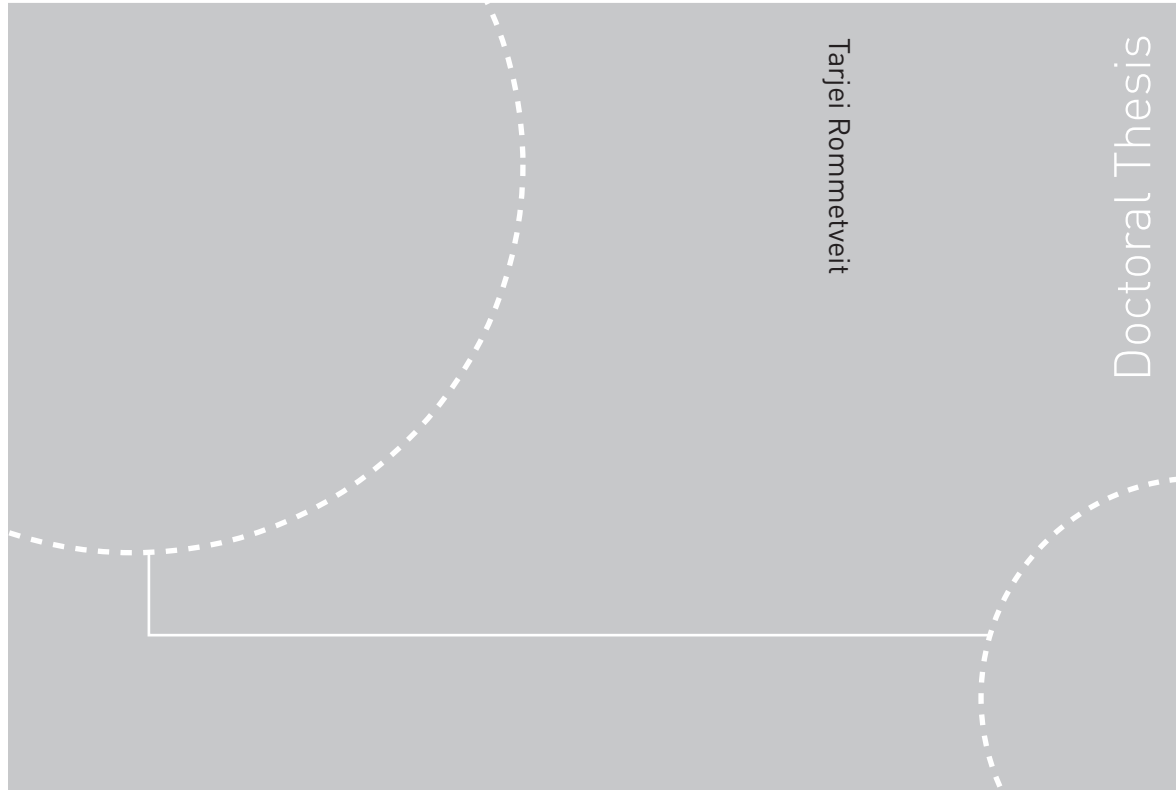


Doctoral theses at NTNU, 2011:254

Tarjei Rommetveit  
**Development of Non-invasive  
Ultrasound Inspection Techniques  
through Steel**



ISBN 978-82-471-3072-8 (printed ver.)  
ISBN 978-82-471-3073-5 (electronic ver.)  
ISSN 1503-8181

NTNU  
Norwegian University of  
Science and Technology  
Thesis for the degree of  
philosophiae doctor  
Faculty of Engineering Science and Technology  
Department of Engineering Design and Materials

Doctoral theses at NTNU, 2011:254

Tarjei Rommetveit

# Development of Non-invasive Ultrasound Inspection Techniques through Steel

Thesis for the degree of philosophiae doctor

Trondheim, October 2011

Norwegian University of  
Science and Technology  
Faculty of Engineering Science and Technology  
Department of Engineering Design and Materials



Norwegian University of  
Science and Technology

**NTNU**

Norwegian University of Science and Technology

Thesis for the degree of philosophiae doctor

Faculty of Engineering Science and Technology  
Department of Engineering Design and Materials

©Tarjei Rommetveit

ISBN 978-82-471-3072-8 (printed ver.)

ISBN 978-82-471-3073-5 (electronic ver.)

ISSN 1503-8181

Doctoral Theses at NTNU, 2011:254

Printed by Tapir Uttrykk



# **Development of Non-invasive Ultrasound Inspection Techniques through Steel**

Tarjei Rommetveit

Institutt for Produktutvikling og Materialer, NTNU

Hovedveileder: Prof. Roy Johnsen

Biveileder: 1. Amanuensis Tonni Franke Johansen

*Ovennevnte avhandling er funnet verdig til å forsvares offentlig for graden philosophiae doctor (ph.d.) i produktutvikling og materialer. Disputas finner sted i Totalrommet i Hovedbygget, Gløshaugen, 13. oktober 2011 kl. 13.15.*



# Abstract

Using normal incident, pulse-echo ultrasound is a well-established approach in the non destructive testing and evaluation community for measuring wall thickness and detecting defects. If the sensors are permanently installed, this opens for a high sensitivity to relatively small changes in the wall thickness. At present, intrusive probe technology is commonly used for rapidly determining the corrosion rate of steel structures. However, non-intrusive methods are often desired. The first part of this thesis focuses on developing a new ultrasound inspection technique in relation to high resolution corrosion monitoring of internal steel surfaces in the presence of thermal variations. The method extracts both the change in steel thickness and temperature from a set of ultrasonic signals in a monitoring setup, eliminating the need for an independent thermometer. The analysis illustrates the importance of temperature compensation and how even small thermal variations can give an erroneous corrosion rate if not corrected for.

In many applications it is required to extract information from materials through steel. Two examples taken from the oil and gas industry are deposits monitoring and cement evaluation through a tubing wall. A challenge when using pulse-echo ultrasound for such applications is the high impedance ratio between the steel and the material under observation causing most of the energy to reverberate back and forth in the steel structure. Signal interference together with a large contrast ratio between the steel reverberations and the desired echo may complicate the detection scheme. It is therefore a need for further development of robust techniques addressing such issues. The second part of this thesis hence deals with feature extraction from materials through steel. It is entirely related to a new bi-layer transducer design or to a dual frequency technique which can be applied with the new transducer. The dual frequency technique is based on transmitting two pulses with a frequency separation of about 1:10 simultaneously and coaxially. The low frequency (LF) pulse manipulates the acoustic properties of the medium nonlinearly, while the high frequency (HF) imaging pulse propagates under the influence of the

LF pulse. In order to transmit such pulse complexes, the transducer consists of two piezoceramic elements which have a common aperture. In the second paper the HF part of such a transducer is characterized, and a methodology for characterizing paraffin wax deposited on steel is presented. The method is based on modeling the electro-acoustic channel of the transducer when only the HF element is active. The model is then fitted to measured data which in turn facilitates inversion of wax parameters. The third paper investigates the same transducer when both elements are active. A method for detecting water films through steel by applying radiation pressure is then presented as well as the modeling and suppression of acoustic crosstalk from the LF to the HF element. The next paper analyzes the two-way dual frequency wave propagation in a plane layer when assuming normal incident, plane wave propagation. In particular, it is discussed how a nonlinear delay between two HF pulses propagating on opposite polarity of the LF pulse accumulates for different boundary conditions and layer properties. This is important for the last paper, where a refined design and prototype testing of the dual frequency transducer is discussed. Experimentally, nonlinear delays are obtained from a water layer both in transmission mode and in pulse-echo mode. It is also illustrated how these delays can be used for suppressing the reverberations in steel relative to the desired echo signal.

# Preface

This thesis has been submitted in partial fulfillment of the requirements for the degree *philosophiae doctor* (ph.d.) at the Faculty of Engineering Science and Technology of the Norwegian University of Science and Technology (NTNU). The research was funded by the Norwegian Research Council and by the partners in the SmartPipe project. It was carried out under the supervision of Professor Roy Johnsen at the Department of Engineering Design and Materials, NTNU, and Assistant Professor Tonni F. Johansen at the Department of Circulation and Medical Imaging, NTNU.

## Acknowledgments

First of all I want to thank my supervisors, Assistant Professor Tonni F. Johansen and Professor Roy Johnsen for giving good guidance and showing great interest in my work.

Assistant Professor Tonni F. Johansen has been invaluable to my ph.d. project with his enthusiastic spirit and his deep knowledge of both the theoretical and practical aspects of ultrasound. He is always available for discussion and has had many good solutions to my problems.

Professor Roy Johnsen has been very important for the completion of the thesis as he always ensured that I made the necessary progress. He has helped me planning the work and his positive attitude has always boosted my morale.

I would like to thank Professor Bjørn Angelsen and my colleagues, Anders Løvstad, Thor Andreas Tangen, Tung Mahn, Jochen Deibele, Halvard Kaupang and Øyvind Standal, for the discussions we have had and for any contributions to my thesis. I am also grateful to Ketil Joner and Stig Tore Svee for their help with the transducer prototypes. The earlier colleagues at Sensorlink AS, Arne Solstad, Øystein Baltzersen, Arve Skjetne, Tor Inge Waag, Vegard Fiksdal and Ibrahim Karaga has also helped me a lot, and I am thankful to them.

Finally, I would like to thank my dear Janne for her love and understanding during these years.



# Contents

Abbreviations . . . . .	13
<b>Introduction</b>	<b>15</b>
1.1 Background . . . . .	15
1.1.1 Wall thickness measurements and corrosion monitoring.	16
1.1.2 Methods for feature extraction from materials through steel. . . . .	17
1.2 Objectives and tasks . . . . .	18
1.3 Estimation of material parameters from layered structures using plane wave analysis . . . . .	19
1.4 Modeling of piezoceramic ultrasound transducers . . . . .	23
1.5 Dual frequency ultrasound . . . . .	26
1.6 Summary of thesis . . . . .	28
1.6.1 Thesis outline . . . . .	30
1.6.2 General discussion and future work . . . . .	31
1.7 Contributions . . . . .	34
References . . . . .	37
<b>A A combined approach for high-resolution corrosion monitoring and temperature compensation using ultrasound</b>	<b>43</b>
A.1 Introduction . . . . .	44
A.2 Theory . . . . .	46
A.2.1 Effect of temperature . . . . .	46
A.2.2 Sub-sample delay estimation . . . . .	47
A.2.3 Derivation of the proposed method (CMTC) . . . . .	48
A.2.4 Corrosion rate vs. rate of change in temperature . . . . .	53
A.3 Experimental procedure . . . . .	54
A.4 Results and discussion . . . . .	57
A.4.1 Error introduced if no temperature compensation is performed . . . . .	57

A.4.2	Test 1: Constant temperature experiment . . . . .	58
A.4.3	Test 2: Varying temperature experiment . . . . .	60
A.4.4	Test 3: Low corrosion rate experiment . . . . .	63
A.4.5	Verification with contact micrometer . . . . .	63
A.4.6	Error due to linearization . . . . .	64
A.4.7	Uncertainty analysis . . . . .	64
A.5	Conclusions . . . . .	66
	References . . . . .	69
<b>B</b>	<b>Using a multi-layered transducer model to estimate the properties of paraffin wax deposited on steel</b>	<b>73</b>
B.1	Introduction . . . . .	74
B.2	Overview of the multi-layered structure . . . . .	76
B.3	Theory . . . . .	77
B.3.1	1D modeling of a multi-layered transducer structure and transceiver circuit . . . . .	77
B.3.2	FE modeling of a multi-layered transducer structure . . . . .	80
B.3.3	Isolation of wax signal . . . . .	82
B.3.4	Inversion procedure . . . . .	83
B.3.4.1	Fitting of Reference Signal . . . . .	84
B.3.4.2	Estimation of acoustical parameters from wax . . . . .	84
B.4	Experimental procedure . . . . .	85
B.5	Results and discussion . . . . .	86
B.5.1	Effect of isolation layer . . . . .	86
B.5.2	Fitting of reference signal . . . . .	87
B.5.3	Isolation of wax signal . . . . .	89
B.5.4	Estimation of parameters from wax layer . . . . .	91
B.6	Conclusions . . . . .	93
	References . . . . .	95
<b>C</b>	<b>A dual frequency transducer applied for fluid film detection through steel using radiation force</b>	<b>99</b>
C.1	Introduction . . . . .	100
C.2	Overview of the layered transducer structure . . . . .	100
C.3	Theory . . . . .	102
C.3.1	Water film detection using radiation force . . . . .	102
C.3.2	1D modeling of acoustic crosstalk . . . . .	103
C.3.3	FE modeling of acoustic crosstalk . . . . .	105
C.4	Methods . . . . .	106
C.4.1	Simulations . . . . .	106

C.4.2	Measurements . . . . .	106
C.5	Results and discussion . . . . .	107
C.5.1	Crosstalk simulations . . . . .	107
C.5.2	Crosstalk suppression . . . . .	107
C.5.3	Water film detection . . . . .	109
C.6	Conclusion . . . . .	110
	References . . . . .	113
<b>D</b>	<b>Two-way nonlinear manipulation in plane materials using dual frequency band pulse complexes</b>	<b>117</b>
D.1	Introduction . . . . .	118
D.2	Theory . . . . .	119
D.2.1	Background; Forward Propagation . . . . .	119
D.2.2	Derivation of the proposed pulse echo model . . . . .	121
D.2.2.1	Special case: Standing LF waves . . . . .	124
D.3	Methods . . . . .	124
D.3.1	Measurements . . . . .	124
D.3.2	Simulations . . . . .	126
D.3.2.1	The SEM tool . . . . .	126
D.3.2.2	Verifying the linear model for broadband LF pulses . . . . .	127
D.3.2.3	The SW situation . . . . .	128
D.4	Results and discussion . . . . .	128
D.4.1	Measurements vs. linear 1D model . . . . .	128
D.4.2	1D Model vs. SEM - Broadband LF pulses . . . . .	130
D.4.3	Nonlinear distortion of $y_{HF}$ . . . . .	131
D.4.4	Influence of HF pulse length . . . . .	132
D.4.5	SW simulations . . . . .	133
D.5	Conclusions . . . . .	135
	References . . . . .	137
<b>E</b>	<b>Design and test of a dual frequency band transducer for extracting nonlinear propagation effects through steel</b>	<b>141</b>
E.1	Introduction . . . . .	142
E.2	Theory of the dual frequency band method and its implications on transducer design . . . . .	143
E.2.1	Generation of nonlinear delays . . . . .	143
E.2.2	Design of the transducer stack . . . . .	145
E.2.2.1	Frequency selective isolation layer . . . . .	145
E.2.2.2	LF energy transfer through steel . . . . .	148

E.2.3	Two-way nonlinear delay in a plane, partial standing LF wave (SW) situation . . . . .	149
E.2.4	A proposed imaging method through steel . . . . .	150
E.3	Methods . . . . .	151
E.3.1	Simulations . . . . .	151
E.3.2	Prototype fabrication . . . . .	153
E.3.3	Measurements . . . . .	154
E.4	Results and discussion . . . . .	155
E.4.1	Characterization of LF part of transducer . . . . .	155
E.4.2	Simulation of delays and on-axis pressure in the NLL . . . . .	157
E.4.3	Nonlinear delays in water tank . . . . .	158
E.4.4	Two-way nonlinear delays in pulse-echo mode . . . . .	159
E.5	Conclusions . . . . .	163
	References . . . . .	165

# Abbreviations

- 1D** One dimensional
- BC** Boundary Conditions
- CMTC** combined Corrosion Monitoring and Temperature Compensation
- CW** Continuous Wave
- DC** Direct Correlation
- E/M** Electro-Mechanical
- EG** Ethylene-Glycol
- ER** Electrical Resistance
- FE** Finite Element
- FEM** Finite Element Model (Finite Element Method)
- FOV** Field Of View
- FSIL** Frequency Selective Isolation Layer
- FSM** Field Signature Method
- HF** High Frequency
- LF** Low Frequency
- LPR** Linear Polarization Resistance
- MLE** Maximum Likelihood Estimator
- NDE** Non Destructive Evaluation

**NDT** Non Destructive Testing

**NLL** NonLinear Layer

**NLM** NonLinear Medium

**PML** Perfectly Matched Layer

**SEM** Spectral Element Model (Spectral Element Method)

**SNR** Signal to Noise Ratio

**SURF** Second order Ultrasound Field

**SW** Standing low frequency Waves

**tof** time-of-flight

# Introduction

Tarjei Rommetveit

Department of Engineering Design and Materials, NTNU

## 1.1 Background

The current trend in offshore petroleum industry is to move into deeper water and more extreme environments. This leads to higher expenses related to, amongst others, inspection, replacement and maintenance of pipes, tubes and process equipment. In order to reduce such costs, there is an increasing demand for online monitoring of failure mechanisms and other parameters for better control and planing of related measures.

The SmartPipe project [1] addresses some of the above mentioned issues by intending to develop a concept for real time monitoring of the technical state of offshore pipelines. The main idea of SmartPipe is to mount distributed sensor packages with local power supply and wireless communication onto the pipeline. Only non-invasive sensors should be used. The following sensor types are integrated in the sensor package:

1. *Thermistors* for measuring temperature.
2. *Accelerometers* for measuring vibrations and inclination.
3. *Strain gauges* for measuring internal pressure and deflection.
4. *Ultrasound transducers* for measuring wall thickness.

The sensor data will be transmitted to a centralized database for storage, analysis and visualization. By combining the measurements with advanced simulation tools, both local and global degradation effects can be monitored. The

first phase of the SmartPipe project focused on the general development of the system and verification. It resulted in a demonstrator showing the feasibility of the concept (summer 2009.) It is aimed at running a second phase of the project ending with a full scale pilot installation.

This ph.d. project is one out of two which is funded through the SmartPipe project. Both ph.d. projects addresses ultrasound inspection methods, but while the other deals with acoustic guided wave technology, this thesis focuses on the development of normal incident pulse-echo inspection techniques through steel with permanently installed sensors related to the following themes:

1. Wall thickness measurements and corrosion monitoring.
2. Methods for feature extraction from materials through steel.

### **1.1.1 Wall thickness measurements and corrosion monitoring.**

For high resolution corrosion monitoring in lab experiments and process control applications, a method denoted Linear Polarization Resistance (LPR) is commonly used [2]. This is an intrusive method based on electrochemical principles. The LPR method and its variants are regarded as very accurate measuring methods with a rapid time response. Limitations with this approach are that it requires continuous water phase and that the probes have a restricted lifetime. Since continuous water phase is required, LPR is usually not suitable for corrosion monitoring in the petroleum industry.

Another intrusive measuring principle is based on Electrical Resistance (ER) which measures the increasing resistance as the probe corrodes [2]. Again a restriction is the limited sensor lifetime which decreases as a function of sensitivity. The ER method does not require a continuous water phase, but it has a slower time response than the LPR principle.

The Field Signature Method (FSM) [3] is a variant of the ER technology which measures the change in current flow and electrical resistance in the pipe by applying a voltage over several pins connected to the pipe. A constant current is fed through the pipe and by measuring the potential drop between the different pin pairs, the internal corrosion pattern can be calculated.

Using ultrasound is a well established approach in the non destructive testing (NDT) community for measuring wall thickness and detecting defects [4]. The ultrasound normal incident pulse-echo approach is based on transmitting an ultrasound pulse from a transducer and into the steel as seen in Figure 1.1 a), and receiving the reflected echoes with the same transducer. The resulting waveform is shown in Figure 1.1 b) and it is characterized by a sequence of

decaying echoes due to the reverberations in steel. Given the sound speed,  $c$ , in steel, the wall thickness,  $L$ , is calculated as

$$L = (\text{tof} \cdot c)/2 \quad (1.1)$$

where  $\text{tof}$  is the time-of-flight between two subsequent echoes. In this way, the wall thickness is measured directly and non-intrusively. By observing the wall thickness over time, the corrosion rate can be estimated.



Figure 1.1: a) Typical setup for measuring wall thickness. b) Received waveform.

The Smartpipe project aims at a sensitivity of  $0.01\text{mm}$  ( $= 10\mu\text{m}$ ) from the wall-thickness measurements. The sensitivity is related to the signal to noise ratio (SNR) of the wall thickness measurements which in turn are directly related to how fast one can estimate a reliable corrosion rate. Several factors will affect the SNR and sensor response. Some examples are amount and type of coating, eventual deposits, roughness of different interfaces, temperature variations, transducer type and the electronics. In this thesis, the resolution of wall-thickness measurements is studied in relation to corrosion rates and temperature effects.

### 1.1.2 Methods for feature extraction from materials through steel.

'Looking' through steel is desired in many situations. One example is during oil- and gas recovery and production, where formation of deposits such as wax, scale and hydrate can cause large production losses due to restricted fluid flow and possible plugging. The need for actions in order to remove deposits, such as operational shut-downs, pigging operations and chemical treatment, leads to great expenses for the petroleum industry. Further, if the composition of

the deposits is unknown, the chemical treatment is to a large extent based on guesswork. This may lead to chemical wastage which further enhances the deposit-related costs. If robust detection and characterization schemes are present, preventive actions can be taken at an earlier point in time.

With ultrasound pulse-echo systems 'looking' through steel is feasible, but there are some challenges. The main issue is usually the large impedance ratio which may occur between the steel and the material under observation. This causes most of the energy to reverberate back and forth inside the steel (as seen in Figure 1.1 b) and only a fraction will be transmitted into and reflected back from the layer of interest. If the strong reverberations from steel overlaps with the weak echo of interest, feature extraction is further complicated.

Several approaches for detecting deposits have been suggested. In [5], an apparatus for measuring the Doppler shift from the flowing fluid inside the pipeline is described. The idea is then to extract the deposit-thickness from the time-gate of the Doppler shift. In [6], guided waves are employed for extracting information about eventual deposits by studying changes in the cut-off frequencies and group velocity of different modes. A method for estimating the thickness of wax deposits as well as identifying hydrates through gas pipelines, based on a standard pulse-echo technique is presented in [7]. At the Robert Gordon University in Aberdeen, a group has produced several publications related to ultrasonic deposit monitoring [8–11]. By using the fact that at an interface between two materials, a certain amount of acoustic energy will be reflected based on the difference in characteristic impedances, one is able to characterize the deposit based on the decaying echo sequence in steel. Fluid film detection through high impedance materials [12, 13] is another area with many of the same challenges as for deposits monitoring. For pipelines a potential application of detecting water films can be to identify areas exposed to CO<sub>2</sub> corrosion.

## 1.2 Objectives and tasks

The main objective of the project has been to improve and develop ultrasound pulse-echo techniques for permanently installed, normal incident sensors related to corrosion monitoring of internal steel walls and feature extraction from materials through steel.

When investigating the issue of corrosion monitoring, existing transducer technology and traditional pulse-echo methods have been used. In relation to feature extraction from materials through steel however, a dual frequency technique requiring a new, bi-layer, transducer design has been studied. The

dual frequency technique is based on transmitting two pulses with a frequency separation of about 1:10 coaxially and simultaneously. The high frequency (HF) pulse is then supposed to propagate under the influence of the low frequency (LF) pulse. This may lead to observable  $2^{nd}$  order effects from the material under observation which can be utilized for new imaging modalities. During the test phase of the transducer, the need for a thorough characterization of its behavior through measurements and modeling was identified. This has in turn triggered the work with parameter estimation through modeling and inversion of the complete electro-acoustic channel based on linear acoustics (i.e. without using the LF manipulation pulse). It has also been necessary to study the dual frequency wave propagation in plane materials and to prove the dual frequency concept through steel. Based on this, the following subtasks have been identified during the course of work:

1. Improve and develop techniques for high resolution corrosion monitoring in the presence of temperature variations.
2. Design and characterize bi-layer transducers to be used for feature extraction through steel. This includes modeling and measurements.
3. Develop a technique for estimating the properties of wax deposited on steel based on linear acoustics.
4. Investigate the possibility of detecting water films through steel using radiation force.
5. Formulate a theory for the accumulative nonlinear propagation effects in a plane layer using the dual frequency method.
6. Prove the nonlinear propagation effects through steel with the bi-layer transducer.

### **1.3 Estimation of material parameters from layered structures using plane wave analysis**

All waves are in reality three-dimensional and have to some extent curved phase fronts. Plane waves are a simplification which assumes plane phase fronts and a one-dimensional (1D) energy propagation. For normal incident beams transmitted into layered structures where the phase fronts are nearly parallel with the interfaces, plane waves are however a good approximation.

### 1.3 Estimation of material parameters from layered structures using plane wave analysis

---

When analyzing plane, linear, wave propagation, we can first consider the broadband pressure pulse,  $p_{m+}(z, t)$ , which propagates in material  $m$  in the positive  $z$ -direction according to:

$$p_{m+}(z, t) = p_{m+}(z - c_m t) . \quad (1.2)$$

Here  $z$  is the position,  $t$  is the time variable and  $c$  is the sound speed. The subscript letter denotes the material. It is often convenient to consider the beams in frequency domain:

$$P_{m+}(z, \omega) = P_{m+}(\omega) e^{-jk_m z} . \quad (1.3)$$

Here  $\omega = 2\pi f$  is the angular frequency,  $k$  is the wave number,  $f$  is the frequency,  $P_{m+}(\omega)$  is the frequency dependent complex envelope while  $j = \sqrt{-1}$ . Further, frequency domain variables are related with time domain variables through the Fourier transform pair. The forward Fourier transform is given by:

$$P_{m+}(z, \omega) = \int_{-\infty}^{\infty} p_{m+}(z, t) e^{-j\omega t} d\omega . \quad (1.4)$$

The inverse Fourier transform is given by:

$$p_{m+}(z, t) = \frac{1}{2\pi} \int_{-\infty}^{\infty} P_{m+}(z, \omega) e^{j\omega t} d\omega . \quad (1.5)$$

If  $P_{m+}$  hits an interface at normal incidence between material  $m$  and material  $n$ , some of the energy are transmitted into material  $n$  while some of the energy is reflected back to material  $m$  as seen in Figure 1.2.

The transmitted and reflected pressure waves are given at  $z = 0$  as

$$\begin{aligned} P_{n+} &= T_{m,n} \cdot P_{m+} \\ P_{m-} &= R_{m,n} \cdot P_{m+} \end{aligned} \quad (1.6)$$

where  $T_{m,n}$  and  $R_{m,n}$  are the pressure transmission- and reflection coefficients from material  $m$  to material  $n$  respectively. These are given by:

$$\begin{aligned} T_{m,n} &= \frac{2Z_n}{Z_m + Z_n} \\ R_{m,n} &= \frac{Z_n - Z_m}{Z_m + Z_n} \end{aligned} \quad (1.7)$$

Here  $Z = \rho c$  is the characteristic impedance of the material while  $\rho$  is the density. As the pulse travel through the medium, it is attenuated due to power

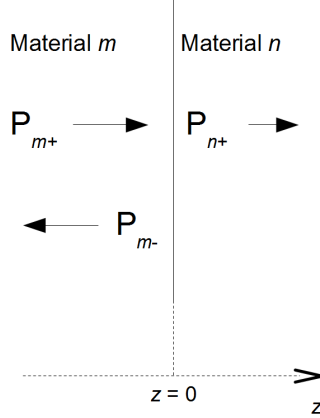


Figure 1.2: Reflection and transmission of the plane, normal incident wave  $P_{m+}$  at an interface.

absorption and scattering losses [14]. It is often a sound approximation to assume that the attenuation increases linearly with frequency by incorporating a loss factor,  $\eta$ , into the wave number:

$$k_m = \frac{\omega}{c_m} \left( 1 - \frac{j\eta_m}{2} \right). \quad (1.8)$$

In general,  $\eta = 1/Q$  where  $Q$  is the mechanical  $Q$ -number.

In a pulse-echo setup, the reflectivity,  $R(\omega)$ , is an important parameter as this relates the incoming pulse to the total reflected signal. For an  $N$ -layer medium it may be challenging to achieve any closed form expressions for  $R(\omega)$ . An alternative is to calculate  $R(\omega)$  by analyzing the frequency dependent acoustic impedance,  $Z_{AI}(\omega)$  iteratively using the formula:

for  $i = 1$  to  $N$

$$Z_{AI,i}(\omega) = Z_i \frac{Z_{AI,i-1} + jZ_i \tan(k_i L_i)}{Z_i + jZ_{AI,i-1} \tan(k_i L_i)} \quad (1.9)$$

end

Here  $Z_{AI,i}$  and  $L_i$  are the spatial dependent acoustic impedance seen into layer  $i$  and thickness of layer  $i$  respectively. In order to initialize the iteration  $Z_{AI,0} = Z_L$  where  $Z_L$  is the characteristic impedance of the load. The concept is illustrated in Figure 1.3. The reflectivity is now given as

$$R(\omega) = \frac{Z_{AI,N}(\omega) - Z_{N+1}}{Z_{AI,N}(\omega) + Z_{N+1}}. \quad (1.10)$$

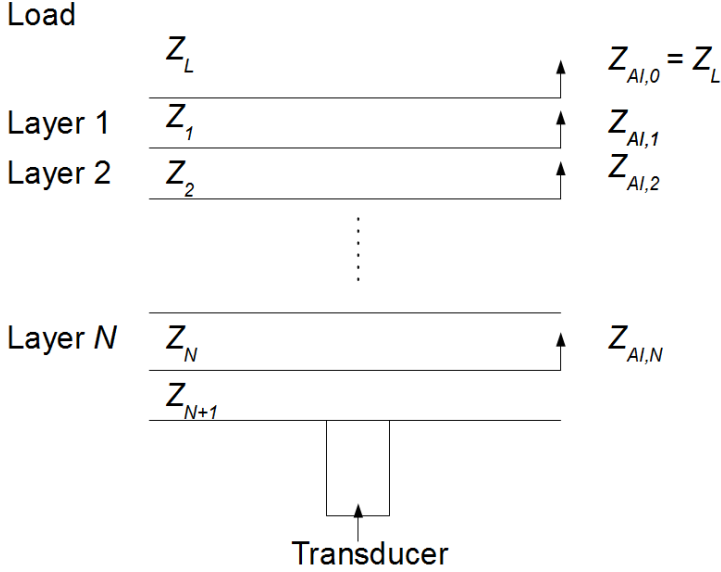


Figure 1.3: Impedances seen into layered medium.

Here  $Z_{N+1}$  is the characteristic impedance of the medium between the sensor and the layered structure.

Eqs. (1.2)-(1.10) can define the building blocks when formulating the forward model for a given problem. The forward model can be used in order to predict the behavior of a system, but it can also be employed to invert acoustical parameters and layer thicknesses from measurements. Then the objective is to estimate some true parameters,  $\mathbf{p}$ , through a comparison of a measured data set,  $d$  and the forward model,  $\bar{d}$ . The best estimate of  $\mathbf{p}$  is the one that minimizes an objective function,  $\varphi$ , which typically is a variant of the squared error sum between  $\bar{d}$  and  $d$ :

$$\varphi(\mathbf{p}) = \|\bar{d}(\mathbf{p}; \omega) - d(\omega)\| . \quad (1.11)$$

Here  $\|\cdot\|$  denotes the L2 norm. The formulation of the inversion problem thus becomes:

$$\hat{\mathbf{p}} = \arg \min_{\mathbf{p}} \varphi(\mathbf{p}) \quad (1.12)$$

Here  $\hat{\mathbf{p}}$  is the estimated value of  $\mathbf{p}$ . Note that the estimation scheme also can be formulated in time-domain.

Much work regarding parameter estimation from layered media is reported in the literature for which a brief discussion follows. The problem of esti-

mating attenuation, group velocity and phase velocity in specimens with sub-wavelength thickness in both pulse-echo and transmission mode is addressed by Kinra and Dayal [15]. The ratio of a reference signal and the received signal is then examined in the frequency domain in order to extract the desired parameters. In [16], Zhu and Kinra has developed a technique to determine thin plate properties using only time domain information. The simultaneous determination of ultrasound velocity and plate thickness from the analysis of thickness resonances is presented by Alvarez-Arenas [17] while the evaluation of thin coatings on thick substrates by using a frequency domain inversion scheme is given in [18].

Characterization of three-layered structures, where up to six parameters are estimated simultaneously using resonant frequencies, is presented by Yapura *et al.* [19]. Raisutis *et al.* has used an iterative deconvolution technique to estimate material properties from the individual layers both in a three-layer aluminum foam precursor material [20] and in a three-layer plastic material [21].

In this thesis parameter estimation based on plane wave analysis is employed both with respect to corrosion monitoring applications, where a maximum likelihood estimator is used, and for estimating layer thicknesses and wax properties in a multi-layered transducer structure, where a genetic algorithm inversion scheme is used.

## 1.4 Modeling of piezoceramic ultrasound transducers

Transducer modeling is an important aspect of sensor development. Through modeling, new ideas can be tested and optimized before moving to the next step of prototyping. As transducer fabrication in many cases is precision work, small deviations relative to the design specification readily occur. Regarding prototyping, modeling in combination with measurements is therefore a vital tool in order to identify such differences and relate them to e.g. layer thicknesses or material parameters.

Transducer modeling is in this thesis divided into finite element method (FEM) modeling and 1D modeling analogous to the plane wave analysis for layered media. The piezoelectric materials will have a polarization normal to the vibrating faces, causing it to operate in thickness mode. A 1D model is a good approximation for layered plate structures where the transverse dimensions are much larger than the wavelength at the desired resonance. We then assume that the strain normal to the propagation is zero leading to a transversally clamped material. One limitation with a 1D model is that transversal modes in general occur in addition to the thickness mode due to finite dimen-

sions. The fundamental transverse mode is in general present at a much lower frequency than the thickness mode, a fact which limits its influence. However, in some cases it is necessary to study how the different modes interact or how complicated geometries affect the transducer behavior. In such situations a FEM model should be employed.

There exist several 1D transducer models. The most common are perhaps the approaches of Mason [22], Redwood [23] and Krimholtz *et al.* [24]. In the current work, the Mason model is employed. The piezoelectric element can then be represented with a three-port lumped circuit as seen in Figure 1.4. Two of the ports represent the acoustical vibrating faces with pressures  $P_1$  and  $P_2$  and particle velocities  $U_1$  and  $U_2$ , while the third port represents the electrical interface with voltage  $V_1$  and current  $I_1$ .

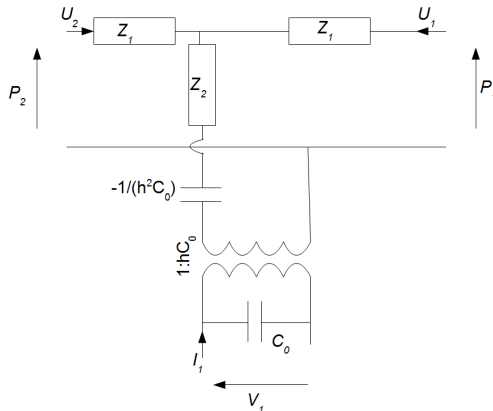


Figure 1.4: Mason equivalent of piezoelectric element.

Mathematically Figure 1.4 can be represented with a matrix representation:

$$\begin{pmatrix} P_1 \\ P_2 \\ V_1 \end{pmatrix} = -j \begin{pmatrix} Z_1 & Z_2 & h/\omega \\ Z_2 & Z_1 & h/\omega \\ h/\omega & h/\omega & 1/(\omega C) \end{pmatrix} \begin{pmatrix} U_1 \\ U_2 \\ I_1 \end{pmatrix} \quad (1.13)$$

Here  $Z_1 = Z/\tan(kL)$  and  $Z_2 = Z/\sin(kL)$  where  $Z$  is the characteristic impedance,  $k$  is the wave number and  $L$  is the thickness of the piezoelectric element. Further,  $C$  is the clamped capacitance and  $h$  is the piezoelectric constant of the element. Eq. (1.13) acts as a basis for transducer modeling, and by terminating the ports with electrical and mechanical impedances, the electro-acoustic behavior of multi-layered structures can be analyzed. For stacks with  $N$  piezoelectric layers, the Mason model can be extended to a multi-port

transducer model governed by an admittance matrix model:

$$\begin{pmatrix} I_1 \\ \vdots \\ I_N \\ U \end{pmatrix} = \begin{pmatrix} Y_{11} & \cdots & Y_{1N} & H_{tt,1} \\ \vdots & \ddots & \vdots & \vdots \\ Y_{N1} & \cdots & Y_{NN} & H_{tt,N} \\ H_{tt,1} & \cdots & H_{tt,N} & Y_M \end{pmatrix} \begin{pmatrix} V_1 \\ \vdots \\ V_N \\ 2F_i \end{pmatrix} \quad (1.14)$$

Here  $Y_{mn}$  is the mutual electrical admittance between port  $m$  and  $n$ , when all ports but  $m$  and  $n$  are shorted.  $H_{tt,m}$  is the transmit transfer function given as  $H_{tt,m} = U/V_m$  when  $V_n = 0 \forall m \neq n$ .  $Y_M = 1/(Z_L + Z_{sM})$  where  $Z_{sM}$  is the mechanical impedance into the surface of the transducer when all electrical ports are shorted. Further,  $U$  is the particle velocity and  $F_i$  is the incoming wave force on the surface of the transducer. Eq (1.14) is derived by Angelsen in [14], ch. 3, and examples of its use related to transducer characterization is given in [25, 26]. Another framework for transducer characterization is presented by Lopez-Sanchez and Schmerr [27] where the transducer's sensitivity and electrical impedance is determined in a pulse-echo setup. A related framework can be used for determining the electro-acoustic path of a measuring setup, where electro-acoustic refer to the combined modeling of the electrical network, the transducer and the acoustic propagation path [28].

In FEM models, the active element may use the piezoelectric material model governed by the stress-charge equations which express the relation between the stress, strain, electric field, and electric displacement field:

$$\begin{aligned} \mathbf{T} &= [c_E] \mathbf{S} - [e^T] \mathbf{E} \\ \mathbf{D} &= [e] \mathbf{S} + [\varepsilon_S] \mathbf{E} \end{aligned} \quad (1.15)$$

Here,  $\mathbf{T}$  is the 6x1 stress vector,  $\mathbf{E}$  is the 3x1 electric field vector,  $\mathbf{S}$  is the 6x1 strain vector and  $\mathbf{D}$  is the 3x1 electric displacement field vector.  $c_E$ ,  $e$  and  $\varepsilon_s$  are the 6x6 elasticity matrix, the 3x6 coupling matrix and the 3x3 permittivity matrix of the material respectively. The subscript  $E$  indicates a zero, or constant, electric field; the subscript  $S$  indicates a zero, or constant, strain field; and the superscript  $T$  stands for transposition of the matrix. Isotropic and anisotropic subdomains (e.g. matching layers, epoxy layers etc.) are governed by Hooke's law,  $\mathbf{T} = [c] \mathbf{S}$  where  $[c]$  is the 6x6 elasticity matrix. In general, 3D FEM models are time consuming to solve and symmetries are often sought for. One example is given in [29] where Frijlink and Torp have simulated a linear array with a 2D FEM model and with the use of symmetry planes. Also in [30], a 2D FEM model is used by Azuma *et al.* in order to analyze unwanted excitation of lamb waves in a bi-layer transducer array. A thorough FEM study

of the general behavior of piezoelectric elements and transducers, is given by Kocbach [31].

In this thesis both 1D models and FEM models have been developed in order to study and characterize a new transducer design consisting of two piezoelectric layers with a frequency separation of about 1:10 stacked on top of each other. The underlying way of thinking, has been plane wave propagation for both elements. The modeling have shown that a 1D model is sufficient for the HF ceramic, while it is not necessarily so for the LF ceramic.

## 1.5 Dual frequency ultrasound

Dual frequency ultrasound is mainly used for extracting  $2^{nd}$  order effects such as nonlinear propagation effects or nonlinear scattering effects. The idea is in general that a LF pulse, which is transmitted only, manipulates the acoustic properties of the medium or the local scattering properties, and that a HF pulse, which is both transmitted and received, is nonlinearly manipulated by the LF pulse. This introduces new degrees of freedom which can lead to new imaging modalities compared to single frequency band methods. In the literature the LF pulse is also denoted manipulation pulse or pump wave, while the HF pulse may be denoted probe pulse or imaging pulse.

Several dual frequency methods have been developed in relation to estimation and imaging of the nonlinearity parameter  $B/A$ . In [32, 33], the LF wave is transmitted perpendicular to the HF pulse and  $B/A$  is estimated from the accumulated HF phase shift. A theoretical study of a reflection mode imaging approach of  $B/A$  is given by Cain [34]. Then the nonlinear interaction between the HF pulse and the LF pulse propagating in opposite directions, causes a phase shift which can be derived. A pulse-echo approach where the LF pulse and HF pulse is transmitted simultaneously and coaxially is given in [35]. The HF pulse is then positioned on the flank of the LF pulse causing a nonlinear frequency shift which is used for estimating  $B/A$ .

In relation to non destructive evaluation (NDE) applications, it has been shown that local scattering properties of cracks and micro-cracks behave nonlinearly. By letting the probing pulse interact with a mechanically generated LF modulation wave, these nonlinear effects are intensified and opens for increased detectability of such damages [36, 37]. In medial applications, a similar approach denoted sonoelasticity [38] where elastic properties of tissue are estimated by applying a LF vibration source to the imaging region, has been developed.

*Second order Ultrasound Field* (SURF) is another technique developed for

medical application. It utilizes dual frequency-band pulse complexes with a frequency ratio of about 1:(7-10). Examples of such pulses are shown in Figure 1.5.

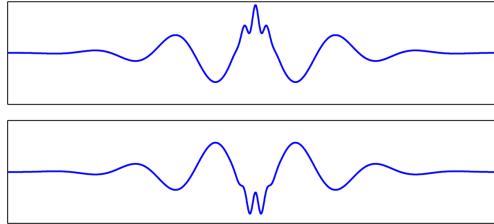


Figure 1.5: Positively (upper) and negatively (lower) manipulated SURF complex.

An important relation for SURF imaging is that between sound speed,  $c$ , and pressure,  $p$ :

$$c(p) \approx c_0 / \sqrt{1 - 2\beta_n \kappa p} \quad (1.16)$$

Here  $c_0$  is the constant linear sound speed,  $\beta_n$  is related to the  $B/A$  parameter as  $\beta_n = 1 + B/(2A)$  and  $\kappa$  is the compressibility of the medium. When transmitting SURF complexes, the aim is to manipulate the elasticity of the propagation medium with the LF pulse. The HF pulse will then propagate under the influence of the of the LF pressure. Because of the effect of nonlinearity on sound velocity, the positively manipulated HF pulse will propagate faster than the negatively manipulated HF pulse. This will cause a nonlinear delay,  $\tau$ , between the two HF pulses which can be expressed as [39]:

$$\tau = \int_{\Gamma} (1/[c_0(1 - \beta_n \kappa p(z))] - 1/[c_0(1 + \beta_n \kappa p(z))]) dz \quad (1.17)$$

where  $\Gamma$  is the propagation path and the spatial dependence of  $p$  is taken into account. This accumulative effect can e.g. be utilized for suppressing reverberations in the ultrasound image [40, 41]. Another application of SURF is that of contrast agent imaging [42, 43] where the nonlinear scattering behavior of contrast bubbles is utilized.

In this thesis, a dual frequency concept based on SURF is studied but with the aim of adapting it to NDE applications for feature extraction from materials through steel. The dual frequency wave propagation has been analyzed from the point of view of plane wave propagation and in relation to the bi-layer transducer which has been developed during this project.

## 1.6 Summary of thesis

This subsection contains a summary of the contributions included in the present thesis.

### **Paper A: A combined approach for high-resolution corrosion monitoring and temperature compensation using ultrasound**

This paper discusses a method for extracting both the steel thickness and the temperature from a set of ultrasonic signals in a monitoring setup, eliminating the need for an independent thermometer. The method can be applied for thickness monitoring in temperature-varying environments.

The main idea is to use an immersion transducer with a well-defined stand-off. If the temperature dependence of the sound speed in the immersion fluid is known a-priori, it is possible to use that knowledge for estimating the temperature which in turn can be used for estimating the temperature compensated steel thickness. A linearized maximum likelihood estimator (MLE) is employed and combined with a sub-sample delay estimation scheme for predicting the optimal values of the temperature and steel respectively. Experimental validation of the proposed technique shows a good correspondence between theory and measurements.

*This paper was published in the IEEE Transactions on Instrumentation and Measurements, vol. 59, issue 11, 2010.*

### **Paper B: Using a multi-layered transducer model to estimate the properties of paraffin wax deposited on steel**

This paper discusses an ultrasound methodology for estimating the acoustical properties of paraffin wax on the surface of steel. A challenge is the large impedance ratio, introducing difficulties in observing the weak echoes received from wax in the presence of the strong reverberations from steel. The presented method is based on modeling and inversion of the complete electro-acoustic channel. Both a 1D model and a FEM model of the structure are developed. The models relate the transmitted voltage over the active piezoelectric element with the received voltage resulting from the acoustic reverberations in the multi-layered structure. By using a reference signal, the wax signal is isolated from the steel reverberations. The isolated wax-signal is then fitted to a corresponding model, facilitating parameter inversion from the wax layer. The models agree well with measurements and it is shown that up to three parameters can be

inverted from the wax simultaneously.

*This paper was published in Ultrasonics, vol. 51, issue 1, 2011.*

### **Paper C: A dual frequency transducer applied for fluid film detection through steel using radiation force**

In the third paper the transducer already presented in Paper B is used for detecting water films through steel by applying radiation force. The method is based on manipulating the water film surface with the low frequency (LF) radiation pressure, while the high frequency (HF) pulse images the film. Acoustic crosstalk from the LF to the HF element introduces unwanted noise. A theoretical framework for evaluating such crosstalk is therefore presented. For the measurements, an empirical approach to crosstalk reduction is performed, and it is shown that the crosstalk suppression is about 15-20dB. The measurements also show that, by applying the radiation force, it is possible to isolate the water film echo from the strong steel reverberations *in situ*, hence making it possible to estimate film thicknesses without the use of any reference signals.

*This paper is being prepared for submission as a short paper.*

### **Paper D: Two-Way Nonlinear Manipulation in Plane Materials using Dual Frequency Band Pulse Complexes**

In the fourth paper a one dimensional model based on plane wave, linear acoustics is derived. It is used to estimate the two-way nonlinear delay,  $\tau$ , obtained in a plane layer using a dual frequency band method where two pulses with a large frequency separation are transmitted simultaneously and coaxially. The model handles broadband LF pulses as well as the continuous wave situation. When continuous waves are transmitted, standing low frequency waves (SW) are generated in the layer. For SW, the location of the HF pulse relative to the LF pulse is investigated. The model then finds the phase relationship which maximizes  $\tau$  given the boundary conditions (BCs) and the linear acoustic parameters of the layer in addition to the incoming pressure. A one dimensional nonlinear simulation tool based on the spectral element method is used to verify the suggested model, and the results show a good correspondence between the two. An experiment is performed to study  $\tau$  as a function of the BCs in a water layer. The measurements are compared with simulations and it is shown how  $\tau$  is related to the nonlinearity parameter  $B/A$ .

*Portions of this work were presented in the Proceedings of the IEEE Ultrasonics Symposium, San Diego, 2010.*

### **Paper E: Design and Test of a Dual Frequency Band Transducer for Extracting Nonlinear Propagation Effects through Steel**

In this paper, the design and test of a dual frequency-band transducer that can be utilized for extracting nonlinear propagation effects from low impedance materials through steel is discussed. Based on the interaction between the HF pulse and the LF manipulation pulse, it is aimed at generating a nonlinear delay from the nonlinear medium beneath steel which in turn is used for suggesting a pulse-echo imaging modality. This modality suppresses the internal reverberations in the transducer and steel relative to the echo of interest. One hypothesis that has to be fulfilled for this method to work, is that the observed nonlinearity should be much larger in the low impedance material than in the transducer and steel.

The transducer design is based on a bi-layer solution where two piezoelectric layers are stacked on top of each other, resulting in a coaxial solution with common aperture for the two frequency bands. In order to transmit sufficient LF energy through steel, a narrowband LF pulse that generates resonance in the transducer and steel is transmitted. Results from finite element method simulations and water tank measurements show that approximately plane LF waves are generated in a narrow frequency band where the LF part of the transducer operates in thickness mode. This is important in order to obtain the correct manipulation of the HF pulses. Experimentally, nonlinear delays are obtained through steel both in the water tank and in pulse-echo mode from a water layer. In pulse-echo mode, the delay is a function of the water layer thickness. The delay is then characterized by a series of periodic peaks due to resonance in the layer. This effect is illustrated in simulations and validated through measurements. The suggested pulse-echo imaging modality works well, and the unwanted reverberations are considerably suppressed relative to the echo of interest.

*This paper is being prepared for submission.*

#### **1.6.1 Thesis outline**

In addition to the introductory chapter, the thesis includes the full-length articles summarized above. Note that for the already published papers, slight corrections can have been made relative to the journal papers. Also note that

as each article should be possible to read as an independent paper, some of the theory may be restated several times.

### **1.6.2 General discussion and future work**

The current work has been categorized into corrosion monitoring and feature extraction through steel. In relation to the former, which is presented in Paper A, the pulse-echo measuring principle has been utilized assuming 1D propagation, linear acoustics and standard single element immersion transducers. Using this well-established approach as a basis, signal processing techniques has been combined with modeling in order to develop a framework for high resolution corrosion monitoring in the presence of temperature variations. The work has focused on small temperature variations. As corrosion attacks in general are slow processes, the results demonstrate that even a slight temperature shift will cause large errors in the estimated corrosion rate if not compensated for. In steel, a  $1\mu\text{m}$  variation corresponds to about 0.01 radians phase change at 5MHz. When investigating changes in the (sub-) micrometer range, the results will therefore be sensitive to various noise terms and other factors. Some examples are e.g. formation of rust deposits and other deposits, changes in surface roughness and temperature gradients. To further enhance the robustness of the method, future work should address such issues. Further, in a concept such as SmartPipe, it may be more appropriate to use viscoelastic elastomers (e.g. polyurethane or epoxy) instead of fluids as the coupling material between the transducer and steel. In the current work, low-attenuating fluids have been used and zero absorption is assumed. Elastomers often exhibits a complex temperature dependence in terms of attenuation and dispersion effects [44] which must be corrected for in a corrosion monitoring setup. An example of a 'clamp-on' design where an elastomer is used as coupling medium, is given in [45].

It is also a need to consider larger temperature variations. This will have an increased impact on the pulse form due to temperature dependent diffraction as a result of sound speed changes, and because the piezoelectric parameters of the transducer may change with temperature. Last but not least a more thorough uncertainty analysis which takes into account more of the aforementioned effects should be performed. This will help identify the parameters introducing most uncertainty into the estimates which again will aid in designing a better measuring setup [46].

The work with feature extraction from materials through steel has been related to the bi-layer transducer and the dual frequency technique. The design presented in Paper B in this thesis was the first out of two transducer concepts developed during this project and the work carried out there can be considered

from two different viewpoints. The first is that it is an independent work dealing with the electro-acoustic modeling and characterization of layered transducer structures in general, with the particular application of parameter inversion from paraffin wax. The second point of view, not directly mentioned in the article, is that it characterizes the HF element and investigates the feasibility of transmitting well-defined broadband HF pulses for this design. Hence Paper B is also a critical part of the characterization for the dual frequency transducer concept.

Although not discussed in any of the papers, the design in Paper B was also tested in order to extract nonlinear propagation effects through steel. This was not achieved. However, another 2<sup>nd</sup> order effect was observed; the effect the acoustic radiation force has on thin water films. This is discussed in Paper C. Two shortcomings were identified regarding the transducer design presented in Paper B. The first was that of the geometry of the LF element, with a thickness (10mm) to diameter (30mm) ratio of 1:3. The large thickness of the element made it challenging to generate a sufficient electrical field which again limited the output pressure. The small ratio made it more demanding to generate the desired plane LF waves. It is also unclear if the nearfield region was sufficient large. The second was that the HF ceramic and LF ceramic had apertures of equal size. This undermined an even manipulation pressure across the HF beam because the LF beam profile decreased much faster in the lateral direction than the HF beam profile. Hence, the center part of the HF pulse would experience a much higher manipulation pressure than the rest of the beam, violating the plane wave terminology used herein. In Paper E, the shortcomings have been addressed by changing the thickness (6mm) to diameter (44mm) ratio of the LF element to 1:7.3 and by decreasing the HF aperture (10mm) relative to the LF aperture (44mm). The design can still be improved. One example is the LF stack which in Paper E consists of 3 elements glued together and electrically connected in series. By connecting these electrically in parallel instead, an increased manipulation pressure will be achieved given the same transmit voltage due to the elevated electrical field. In the current work, they were connected in series due to time constraints.

In the beginning of this project, it was aimed at developing a simple transducer prototype relatively fast, and work more with dual frequency wave propagation and testing of different materials. However, the need for a thorough understanding of the transducer was quickly identified, leading to much work related to modeling, prototyping and characterization. This left little time left for testing experimentally how the nonlinear delay changes with different boundary conditions and materials. To be more specific; in Paper D the theo-

retical two-way nonlinear delay in a plane layer is analyzed for continuous LF waves. It is distinguished between the two boundary conditions where the reflection coefficient,  $R$ , between the layer and load is above and below zero. This categorization is important because when  $R > 0$ , the HF pulse will experience the same polarity of the manipulation pressure both forwards and backwards. However, when  $R < 0$ , the HF pulse will experience the opposite polarity on the way back from the reflecting interface. This complicates the observation of the nonlinear effect because the accumulated delay obtained on the way forwards to the reflector will decrease when the HF pulse propagates back. The analysis still reveals the feasibility of obtaining nonlinear delays for  $R < 0$  and in particular around the resonance peaks of the LF wave.  $R < 0$  is a particularly important case in relation to the detection of deposits. E.g. for a wax-gas interface,  $R \approx -1$ , while for a scale-oil interface  $R \approx -0.6$ . A more detailed experiment should therefore be carried out in order to analyze these scenarios.

One of the limitations with the dual frequency transducers has been acoustic crosstalk from the LF element to the HF element generating unwanted noise in the HF frequency band. The hypothesis is that the LF element, even though excited with a CW wave, also transmits small stress components in the HF frequency band. Even though these components are 60dB down relative to the components at the LF centre frequency, they will contribute to the recorded HF signal. This limits the detectability of small nonlinear delays and it also degrades the results of the suggested imaging modality presented in Paper E. A framework for the theoretical modeling and empirical crosstalk suppression is discussed in Paper C, but it is still a need for better characterizing and compensating for such effects.

## 1.7 Contributions

What follows is a list of contributions made during the time as a ph.d. candidate.

### Peer reviewed papers

1. **Tarjei Rommetveit**, Tonni F. Johansen and Roy Johnsen, "A combined approach for high-resolution corrosion monitoring and temperature compensation using ultrasound," *IEEE Transactions on Instrumentation and Measurements*, vol. 59, issue. 11, 2010
2. **Tarjei Rommetveit**, Tonni F. Johansen and Roy Johnsen "Using a multi-layered transducer model to estimate the properties of paraffin wax deposited on steel," *Ultrasonics*, vol. 51, issue. 1, 2011

### Conference proceedings

1. **Tarjei Rommetveit**, Roy Johnsen and Øystein Baltzersen, "Using low-noise ultrasound measurements for real-time corrosion monitoring of pipelines," *Proc. of 31st Scandinavian Symposium on Physical Acoustics*, 2008.
2. **Tarjei Rommetveit**, Roy Johnsen and Øystein Baltzersen, "Using ultrasound measurement for real-time process control of pipelines and process equipment subjected to corrosion and/or erosion," Paper 08285, *NACE Corrosion*, New Orleans, 2008.
3. **Tarjei Rommetveit**, Tonni F. Johansen, Roy Johnsen and Øystein Baltzersen, "High resolution ultrasound wall thickness measurements through polyester coating and real-time process control," Paper 09452, *NACE Corrosion*, Atlanta, 2009.
4. Øystein Baltzersen, **Tarjei Rommetveit**, Erik Strand and Øyvind Dahle, "Ultrasonic System for Monitoring of Corrosion in Real Time," *Proc. of the 13th Middle East Corrosion Conference*, Bahrain, 2010.
5. Tonni F. Johansen and **Tarjei Rommetveit**, "Characterization of ultrasound transducers," *Proc. of 33rd Scandinavian Symposium on Physical Acoustics*, 2010.
6. **Tarjei Rommetveit**, Tonni F. Johansen, Jochen Deibele, Halvard Kaugang and Bjørn Angelsen, "Two-Way Nonlinear Manipulation in Plane

Materials using Dual Frequency Band Pulse Complexes," *Proc. IEEE Ultrasonics Symposium*, San Diego, 2010.

**Other Talks and Presentations**

1. **Tarjei Rommetveit**, Anders Løvstad, "Structural Health- and Corrosion Monitoring of Pipelines Using Ultrasound," *Seminar for strategisk inspeksjonsstyring 2008*



# References

- [1] SmartPipe project. [Online]. Available: <http://www.sintef.no/Projectweb/SmartPipe/>.
- [2] V. S. Agarwala and S. Ahmad, "Corrosion detection and monitoring a review," in *Proceedings of NACE Corrosion 2000, Orlando*, pp. 00271.1–00271.19, 2000.
- [3] A. Daaland, *Investigation and modelling of corrosion attacks for developing the FSM technology*. Dr. ing. thesis, Norwegian University of Science and Technology, Trondheim, Norway, 1994.
- [4] J. Krautkramer and H. Krautkramer, *Ultrasonic Testing of Materials*. Springer-Verlag, 1983.
- [5] W. Han, J. Birchak, C. L. Richards, V. V. S. Vimal, S. H. Bruce, R. M. Amin, R. J. Selvaggi, and L. A. Pearlstein, "Method and apparatus for pulsed ultrasonic doppler measurement of wall deposition." US patent no. 20020166383, 2002.
- [6] J. Kochback, R. A. Kippersund, and P. Lunde, "Time Domain Finite Element Modeling of SH-mode propagation in elastic plates with deposits," in *Proceedings of the 33rd Scandinavian Symposium on Physical Acoustics*, 2010.
- [7] C. E. Woon and L. D. Mitchell, "Ultrasonic instrumentation for on-line monitoring of solid deposition in pipes," in *Proceedings of the SPE Production Operations Symposium*, 1997.
- [8] M. Y. Qureshi, *Development of techniques for detection and dissolution enhancement of mineral deposits in petroleum pipelines using ultrasound*. Phd, The Robert Gordon Univ, Aberdeen, U.K, 2002.

- 
- [9] K. Christidis, *Characterization and monitoring of mineral deposits in down-hole petroleum pipelines*. Phd, The Robert Gordon Univ, Aberdeen, U.K, 2000.
- [10] K. Christidis and G. P. P. Gunarathne, "Temperature compensation for ultrasound measurements and characterization of materials," *Instrumentation and Measurements, IEEE Transactions on*, vol. 52, no. 5, pp. 1520–1527, 2003.
- [11] G. Gunarathne and K. Christidis, "Material characterization in situ using ultrasound measurements," *Instrumentation and Measurement, IEEE Transactions on*, vol. 51, pp. 368–373, Apr. 2002.
- [12] Z. Chen, J. Hermanson, M. Shear, and P. Pedersen, "Ultrasonic monitoring of interfacial motion of condensing and non-condensing liquid films," *Flow Measurement and Instrumentation*, vol. 16, no. 6, pp. 353–364, 2005.
- [13] P. C. Pedersen, Z. Cakareski, and J. C. Hermanson, "Ultrasonic monitoring of film condensation for applications in reduced gravity," *Ultrasonics*, vol. 38, no. 1-8, pp. 486–490, 2000.
- [14] B. Angelsen, *Ultrasound imaging Waves, signals and signal processing Vol I*. Trondheim: Emantec, 2000.
- [15] V. K. Kinra and V. Dayal, "A new technique for ultrasonic-nondestructive evaluation of thin specimens," *Experimental Mechanics*, vol. 28, no. 3, pp. 288–297, 1988.
- [16] C. Zhu and V. K. Kinra, "A new technique for time-domain ultrasonic nde of thin plates," *Journal of Nondestructive Evaluation*, vol. 12, no. 2, pp. 121–131, 1993.
- [17] T. E. G. Alvarez-Arenas, "Simultaneous determination of the ultrasound velocity and the thickness of solid plates from the analysis of thickness resonances using air-coupled ultrasound," *Ultrasonics*, vol. 50, no. 2, pp. 104–109, 2010.
- [18] V. K. Kinra and C. Zhu, "Ultrasonic evaluation of thin (sub-wavelength) coatings," *The Journal of the Acoustical Society of America*, vol. 93, no. 5, pp. 2454–2467, 1993.
- [19] C. L. Yapura, V. K. Kinra, and K. Maslov, "Measurement of six acoustical properties of a three-layered medium using resonant frequencies," *The*

- Journal of the Acoustical Society of America*, vol. 115, no. 1, pp. 57–65, 2004.
- [20] R. Raisutis, R. Kazys, and L. Mazeika, “Ultrasonic thickness measurement of multilayered aluminum foam precursor material,” *Instrumentation and Measurement, IEEE Transactions on*, vol. 57, no. 12, pp. 2846–2855, 2008.
- [21] R. Raisutis, R. Kazys, and L. Mazeika, “Application of the ultrasonic pulse-echo technique for quality control of the multi-layered plastic materials,” *NDT&E International*, vol. 41, pp. 300–311, 2008.
- [22] W. P. Mason, *Electromechanical Transducers and Wave filters*. D. Van Nostrand Company, Inc, 1948.
- [23] M. Redwood, “Transient performance of a piezoelectric transducer,” *The Journal of the Acoustical Society of America*, vol. 33, no. 4, pp. 527–536, 1961.
- [24] R. Krimholtz, D. Leedom, and G. Matthaei, “New equivalent circuits for elementary piezoelectric ceramic transducers,” *Electronics Letters*, vol. 6, no. 13, pp. 398–399, 1970.
- [25] T. Johansen and B. Angelsen, “Versatile analysis of multilayer piezoelectric transducers using an admittance matrix approach,” in *Proceedings of the 28th Scandinavian Symposium on Physical Acoustics*, January 2005.
- [26] T. Johansen and T. Rommetveit, “Characterization of Ultrasound Transducers,” in *Proceedings of the 33rd Scandinavian Symposium on Physical Acoustics*, January 2010.
- [27] A. Lopez-Sanchez and L. Schmerr, “Determination of an ultrasonic transducer’s sensitivity and impedance in a pulse-echo setup,” *Ultrasonics, Ferroelectrics and Frequency Control, IEEE Transactions on*, vol. 53, pp. 2101–2112, november 2006.
- [28] C. Dang, *Electromechanical Characterization of Ultrasonic NDE Systems*. Phd, Iowa State University, Ames, USA, 2001.
- [29] M. Frijlink and H. Torp, “Simulation of acoustic fields from arbitrary transducer stacks using a fem transducer model and nonlinear wave propagation,” in *Proceedings of the IEEE International Ultrasonics Symposium*, pp. 2340–2343, sept. 2009.

- 
- [30] T. Azuma, M. Ogihara, J. Kubota, A. Sasaki, S.-i. Umemura, and H. Furuhashi, "Dual-frequency ultrasound imaging and therapeutic bilaminar array using frequency selective isolation layer," *Ultrasonics, Ferroelectrics and Frequency Control, IEEE Transactions on*, vol. 57, pp. 1211–1224, may 2010.
- [31] J. Kocbach, *Finite element modeling of ultrasonic piezoelectric transducers*. Phd, University of Bergen, Bergen, Norway, 2000.
- [32] N. Ichida, T. Sato, and M. Linzer, "Imaging the nonlinear ultrasonic parameter of a medium," *Ultrasonic Imaging*, vol. 5, pp. 295–299, 1983.
- [33] T. Sato, Y. Yamakoshi, and T. Nakamura, "Nonlinear tissue imaging," in *Proceedings of the IEEE International Ultrasonics Symposium*, pp. 889–900, 1986.
- [34] C. A. Cain, "Ultrasonic reflection mode imaging of the nonlinear parameter B/A: I. A theoretical basis," *The Journal of the Acoustical Society of America*, vol. 80, no. 1, pp. 28–32, 1986.
- [35] S.-I. U. H. Fukukita and T. Yano, "Ultrasound pulse reflection mode measurement of nonlinearity parameter B/A and attenuation coefficient," *The Journal of the Acoustical Society of America*, vol. 99, no. 5, pp. 2775–2782, 1996.
- [36] J.-Y. Kim, V. A. Yakovlev, and S. I. Rokhlin, "Surface acoustic wave modulation on a partially closed fatigue crack," *The Journal of the Acoustical Society of America*, vol. 115, no. 5, pp. 1961–1972, 2004.
- [37] M. Poznic and C. Pecorari, "Discriminating surface-breaking from subsurface cracks in pressurized water pipes by means of a parametric modulation technique," *NDT & E International*, vol. 41, no. 3, pp. 208 – 216, 2008.
- [38] R. M. Lerner, S. R. Huang, and K. J. Parker, "Sonoelasticity images derived from ultrasound signals in mechanically vibrated tissues.," *Ultrasound Med Biol*, vol. 16, no. 3, pp. 231–239, 1990.
- [39] S. P. Näsholm, *Ultrasound beams for enhanced image quality*. Phd, Department of Circulation and Medical Imaging, Norwegian University of Science and Technology, Trondheim, Norway, 2008. ISBN 978-82-471-9130-9.
- [40] R. Hansen, S. Måsøy, T. F. Johansen, and B. A. Angelsen, "Utilizing dual frequency band transmit pulse complexes in medical ultrasound imaging,"

*The Journal of the Acoustical Society of America*, vol. 127, no. 1, pp. 579–587, 2010.

- [41] S. P. Näsholm, R. Hansen, S. Måsøy, T. F. Johansen, and B. A. J. Angelsen, “Transmit beams adapted to reverberation noise suppression using dual-frequency SURF imaging,” *IEEE Transactions on Ultrasonics, Ferroelectrics, and Frequency Control*, vol. 56, pp. 2124–2133, Oct. 2009.
- [42] B. A. J. Angelsen and R. Hansen, “SURF Imaging - A new Method for Ultrasound Contrast Agent Imaging,” in *Proceedings of the IEEE International Ultrasonics Symposium*, pp. 531–541, 2007.
- [43] S.-E. Måsøy, Ø. Standal, P. Näsholm, T. F. Johansen, B. A. J. Angelsen, and R. Hansen, “SURF Imaging: In vivo demonstration of an ultrasound contrast agent detection technique,” *IEEE Transactions on Ultrasonics, Ferroelectrics, and Frequency Control*, vol. 55, pp. 1112–1121, May 2008.
- [44] J. M. Hugh, *Ultrasound Technique for the Dynamic Mechanical Analysis (DMA) of Polymers*. Phd, Technical University in Berlin, Berlin, Germany, 2008.
- [45] Ø. Baltzersen, T. Rommetveit, E. Strand, and Ø. Dahle, “Ultrasonic system for monitoring of corrosion in real time,” in *Proceedings of the 13th Middle East Corrosion Conference, Bahrain*, 2010. Paper 140-CM-29.
- [46] E. Bjorndal and K.-E. Froyso, “Acoustic methods for obtaining the pressure reflection coefficient from a buffer rod based measurement cell,” *Ultrasonics, Ferroelectrics and Frequency Control, IEEE Transactions on*, vol. 55, pp. 1781–1793, august 2008.



# A combined approach for high-resolution corrosion monitoring and temperature compensation using ultrasound

Tarjei Rommetveit<sup>1</sup>, Tonni F. Johansen<sup>2</sup> and Roy Johnsen<sup>1</sup>

<sup>1</sup>Department of Engineering Design and Materials, NTNU, Trondheim, Norway,

<sup>2</sup>Department of Circulation and Medical Imaging, NTNU, Trondheim, Norway

## Abstract

An approach for combined corrosion monitoring and temperature compensation (CMTTC) using permanently installed immersion ultrasound probes with a well defined standoff is presented. Combining sub-sample delay estimation with knowledge of how the sound speed in the immersion fluid and the steel varies with temperature enables us to estimate the temperature variations as well as the changes in wall thickness simultaneously using a linearized maximum likelihood estimator (MLE). The results show that sub-micrometer changes in the wall thickness are detected, and that the corrosion rates are predicted in good accordance with theory, also in the presence of temperature variations.

## A.1 Introduction

Corrosion is a major limiting factor in the service life of components ranging from microelectronics to offshore structures. The annual economic losses in USA due to corrosion damage are estimated to about 3.1% of the Gross Domestic Product [1]. In the petroleum industry, which is the main concern in this work, corrosion damage can lead to fatal environmental consequences due to oil leakage as well as huge maintenance/repair costs due to breakdown of process equipment. Hence it is of great importance to implement a corrosion management system including e.g. modeling, inspection and monitoring.

Corrosion of steel is a slow process. Typical acceptable general uniform corrosion rates for pipelines are in the range 0.1-0.2 mm/year [2]. This corresponds to a change in the wall thickness of 11.4-22.8 nm/hour. There are some applications where one aims for estimating the 'instantaneous' corrosion rate. One application is that of inhibitor optimization. Corrosion inhibitors are widely used in order to reduce the corrosion to a minimum. As such inhibitors both lead to great expenses (e.g. to the petroleum industry) and to chemical wastage, it is of common interest to optimize both type and amount which simultaneously minimize corrosion. Also, as the corrosive environment changes, a change in the composition of the inhibitor may be necessary over time. In order to optimize the use of inhibitors with respect to amount and efficiency it is therefore of vital interest to monitor the corrosion rate 'instantaneously,' i.e. as fast as possible. Using ultrasound is a well-established approach in the non destructive testing community for measuring wall thickness and detecting defects [3]. The well-known pulse-echo technique is frequently used for one-side access measurements [4] and should be well suited for general corrosion monitoring applications. However, when it comes to high resolution corrosion monitoring, probe technology is more commonly used. Some examples of probe technology are *Linear Polarization Resistance* (LPR), which is based on electrochemical principles, and *Electrical Resistance* (ER), which is based on measuring the increasing internal resistance as the probe corrodes. A drawback with LPR probes is that they require continuous water phase, and can thus not be used in oil and gas pipelines (except in water phase). General drawbacks with probe technology are that they are invasive and that they have a limited lifetime as they measure corrosion on the probe itself. An overview of corrosion monitoring techniques is given in [5].

Ultrasound has some advantages compared to probe technology: First of all it is non-invasive, secondly it measures directly on the metal of interest and finally the ultrasound probes have no theoretical upper lifetime-limit. A challenge with high resolution ultrasound applications is the temperature vari-

ations of acoustic properties which often have to be compensated for [6]. An approach to temperature compensation of diffuse ultrasonic waves for structural health monitoring where a model for the temperature dependent delays in an aluminum structure is developed, is presented in [7]. This has relations to our application where we need control of the sound speed and the thermal expansion; the smaller changes in steel thickness we want to estimate, the more critical is a robust temperature compensation scheme. Another challenge is the requirement for small changes in the wall thickness to be detected. Earlier work has shown that wall thickness changes in the sub-micrometer range are detectable [8–10].

The objective with this paper is twofold: a) To show the importance of temperature compensation with respect to high resolution corrosion monitoring and b) to develop a new method for corrosion monitoring of steel structures such as pipelines, where the wall thickness and the temperature is estimated simultaneously using only one ultrasound pulse-echo measurement. Throughout this paper, the proposed method is denoted CMTC as an acronym for *combined Corrosion Monitoring and Temperature Compensation*.

Applying ultrasound measurements for temperature estimation is a well-established technique in the literature [11]. There are some benefits with using the ultrasound sensor both as temperature- and wall-thickness estimator; a) traditional thermometers will be superfluous causing fewer sensors and less complexity in the complete measuring setup, and b) the temperature will be measured at the same spot as the wall-thickness measurement which means a more correct estimate in the case of temperature gradients. CMTC requires a combination of sub-sample delay algorithms [12, 13] and a mathematical model of how the delays are functions of the temperature and the wall thickness. In order to obtain an optimal estimate with respect to the variances a linearized maximum likelihood estimator (MLE) is employed. Note that a concept for immersion wall thickness monitoring of subsea pipelines already has been developed [10], and this can act as a starting point for a real CMTC-based system.

The paper is organized as follows: First, an outline of the background theory and CMTC is given. Then the experimental method for validating CMTC is presented. Finally the results are discussion before a brief conclusion is given at the end.

## A.2 Theory

### A.2.1 Effect of temperature

For the proposed estimation scheme, control of temperature variations both in the steel and in the immersion fluid is required. For the steel there are two relevant issues:

1. Thermal expansion.
2. Thermal variations of the sound speed.

The thermal expansion is in general temperature dependent but it changes slowly with temperature. For a certain temperature range, it is thus a reasonable assumption to use the linear thermal expansion coefficient,  $\alpha$ , which relates the change in temperature to the change in the material's dimensions by the following equation [14]:

$$\alpha = \frac{1}{y_{st}^0} \frac{\Delta y_{st}}{T - T^0} \quad (\text{A.1})$$

Here  $y_{st}^0$  is the thickness of the material at reference temperature  $T^0$ ,  $T$  is the current temperature, and  $\Delta y_{st}$  is the thermal expansion due to the temperature shift.  $T^0$  is in this work equal to  $25^\circ\text{C}$ . In CMTC,  $y_{st}^0$  is the main parameter we want to estimate. Using the fact that the Young's modulus,  $E$ , varies linearly with temperature [15] and that the total mass will be constant during the thermal expansion, the longitudinal sound speed (P-wave speed) in steel is given by [8]

$$c_{st}(T) = \sqrt{\Upsilon (E^0 + \beta(T - T^0)) (1 + \alpha(T - T^0))^3 / \rho^0}. \quad (\text{A.2})$$

Here  $\Upsilon = (1 - \nu)/(1 - \nu - 2\nu^2)$ ,  $\nu$  is the Poisson's ratio,  $\rho^0$  is the density referred to  $T^0$ ,  $E^0$  is Young's modulus at  $T^0$  while  $\beta$  is a material-specific parameter. It is not straight forward to determine the exact material parameters for the steel, and small variations may occur from sample to sample. For practical reasons (A.2) is approximated with a  $2^{nd}$  order polynomial:

$$c_{st}(T) \approx \sum_{n=0}^2 \varphi_n T^n. \quad (\text{A.3})$$

Here  $\varphi_n$  denotes the regression coefficients which determine the temperature dependent sound speed in steel. When we perform pulse-echo measurements of steel with constant temperature, the thickness can be calculated as

$$y_{st}(T) = c_{st}(T) \cdot \delta_{st}/2. \quad (\text{A.4})$$

Here  $\delta_{st}$  is the time-of-flight (tof) in the steel and  $y_{st}(T) = (1 + \alpha(T - T^0)) \cdot y_{st}^0$ . Note that for steel,  $\beta/E^0 \gg \alpha$ , and hence the variations in sound speed will dominate compared to the thermal expansion. For relevant contact fluids such as water and ethylene-glycol (EG), the sound speed,  $c_f$ , is in general approximated with an  $N^{\text{th}}$  order polynomial depending on the temperature range and curvature of the function:

$$c_f(T) = \sum_{n=0}^N \gamma_n T^n \quad (\text{A.5})$$

Here  $\gamma_n$  denotes the regression coefficients which determine the temperature dependent sound speed in the fluid.

### A.2.2 Sub-sample delay estimation

In this work, a relatively low sampling rate (50MHz) is employed. For many real-life applications a low sampling rate decreases the complexity of the system. A higher resolution of the wall thickness measurements is achieved by sub-sample delay estimation. Now consider the recorded discrete, noisy acoustic pulses  $s_{j-1}(n)$  and  $s_j(n)$  from measurement number  $j - 1$  and  $j$  respectively and assume they take the form

$$\begin{aligned} s_{j-1}(n) &= x(n) + w_{j-1}(n) \\ s_j(n) &= x(n - \tau) + w_j(n), \end{aligned} \quad (\text{A.6})$$

where  $x$  is the acoustic pulse and  $w$  is additive white Gaussian noise. The desired delay,  $\tau$ , is in general not an integer and must be estimated using a sub-sample delay algorithm. For CMTC, any suitable algorithm can be utilized, but in this paper the well-known direct correlator with parabolic fit is employed [12, 13]. This is given by

$$\hat{\tau} = T_s \left[ m - 0.5 \frac{\hat{R}_{s_{j-1}s_j}(m+1) - \hat{R}_{s_{j-1}s_j}(m-1)}{\hat{R}_{s_{j-1}s_j}(m+1) - 2\hat{R}_{s_{j-1}s_j}(m) + \hat{R}_{s_{j-1}s_j}(m-1)} \right], \quad (\text{A.7})$$

where  $T_s$  is the sampling period, and  $m = \arg \max \hat{R}(l)$  is the estimated correlation function.

### A.2.3 Derivation of the proposed method (CMTC)

We can represent the sequence of  $K$  echoes received from measurement  $j$  as

$$s_j(n) = \sum_{k=0}^{K-1} x_{k,j}[n] + w(n). \quad (\text{A.8})$$

Disregarding the subscript  $j$ , the echo  $x_k$  is received at time  $t_k$  (see figure A.1) which is given by

$$t_k = k \cdot \delta_{st}(T, y_{st}^0) + \delta_f(T). \quad (\text{A.9})$$

Here  $\delta_{st}$  is the tof in the coupling fluid. Since the sound speed varies with temperature,  $\delta_{st}$  will be a function of temperature,  $T$ , in addition to the decreasing steel thickness,  $y_{st} \cdot \delta_{st}$  will only be a function of temperature since no corrosion is expected on that side of the steel. For an illustration of the measurement setup and the waveform, see Figure A.1 and Figure A.2 respectively.

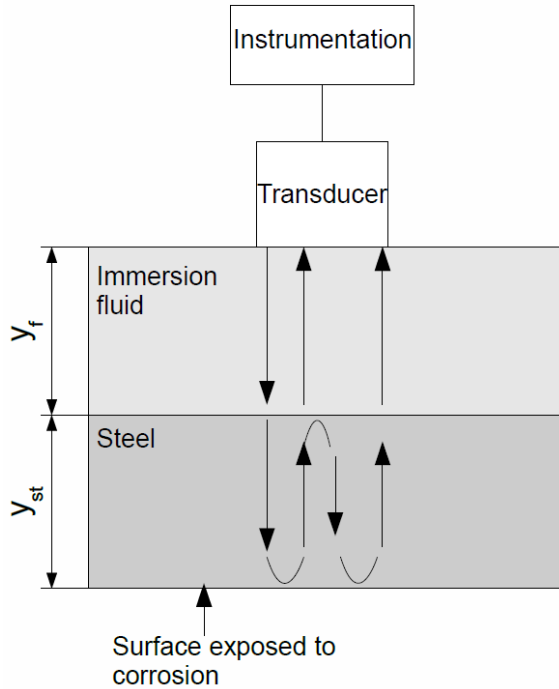


Figure A.1: Principle drawing of the problem.

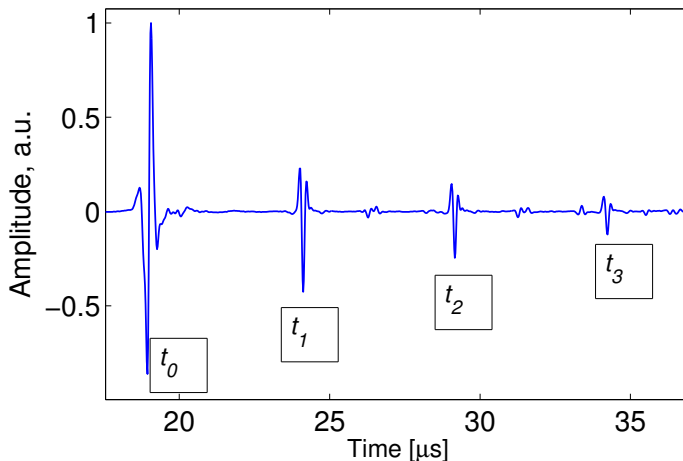


Figure A.2: A typical received waveform from the pulse-echo measurement. ( $t_k, k = 0..3$ : Time instants of the p-wave reflections. a. u. denotes amplitude in arbitrary units.)

Assume we have performed a similar measurement as in Eq.(A.8) at time instant  $j-1$ . If the temperature or wall thickness has changed from measurement  $j-1$  to  $j$ , all other parameters being equal, then  $\delta_{st}$  and possibly  $\delta_f$  should also have changed. Now we can identify each echo in the waveforms and do sub-sample time delay estimation between the echoes in  $s_{j-1}$  and  $s_j$  using Eq. (B.13). The time delays between time instant  $j-1$  and  $j$  can mathematically be modeled as:

$$\begin{aligned} \tau_{k,j}(T_j, y_{st,j}^0) &= (k \cdot \delta_{st}(T_j, y_{st,j}^0) + \delta_f(T_j)) \\ &- \left( k \cdot \delta_{st}(\hat{T}_{j-1}, \hat{y}_{st,j-1}^0) + \delta_f(\hat{T}_{j-1}) \right), k = 0 \dots K-1 \end{aligned} \quad (\text{A.10})$$

It is assumed that the temperature and wall thickness from the previous measurement already is estimated as  $\hat{T}_{j-1}$  and  $\hat{y}_{st,j-1}^0$  respectively. From Eq. (A.10) it is clear that the delays as a function of  $k$  represent much redundant information. This can be used for enhancing the resolution of our estimate. The physical meaning of the various delays is given in Table A.2.3.

As the contribution from the immersion fluid is constant for all delays, we can rewrite Eq. (A.10) as

$$\tau_{k,j} = \tau_{0,j} + k \cdot \tau_{st,j}, k \geq 0, \quad (\text{A.11})$$

Table A.1: Physical meaning of delays for increasing number of echoes

Delay	Physical meaning
$\tau_0$	time difference due to temperature variations in the immersion fluid
$\tau_1$	$\tau_0 + 1 \times$ (time difference due to temperature variations and thickness variations for the steel)
...	...
$\tau_{K-1}$	$\tau_0 + (K - 1) \times$ (time difference due to temperature variations and thickness variations for the steel)

where

$$\begin{aligned}\tau_{st,j} &= \delta_{st}(T_j, y_{st,j}^0) - \delta_{st}(\hat{T}_{j-1}, \hat{y}_{st,j-1}^0) \\ \tau_{0,j} &= \delta_f(T_j) - \delta_f(\hat{T}_{j-1}).\end{aligned}\tag{A.12}$$

In general, if there is a temperature gradient in the immersion fluid,  $\delta_f$  is given by

$$\delta_f = \int_0^{y_f} 2dz/c_f(T(z)).\tag{A.13}$$

Here  $z$  is the distance from the transducer surface to the observation point,  $y_f$  is the total standoff, and  $T$  will be a function of position. In this work we assume a zero temperature gradient, and hence  $\delta_f$  is given by

$$\delta_f(T) = 2y_f(T)/c_f(T).\tag{A.14}$$

We see that, depending on the measuring setup,  $y_f$  is a function of temperature and this should also be compensated for. In this work thread bars with the same  $\alpha$  as for the steel are employed in order to have a well defined standoff. Thus  $y_f(T) = y_f^0(1 + \alpha(T - T^0))$  where  $y_f^0$  is the standoff at temperature  $T^0$ . By combining Eq. (A.5) and Eq. (A.14),  $\tau_{0,j}$  can be rewritten as

$$\tau_{0,j} = 2y_f^0 \left( \frac{(1 + \alpha(T_j - T^0))}{\sum_{n=0}^N \gamma_n T_j^n} - \frac{(1 + \alpha(\hat{T}_{j-1} - T^0))}{\sum_{n=0}^N \gamma_n \hat{T}_{j-1}^n} \right).\tag{A.15}$$

Now we already have the estimates from measurement  $j - 1$ . If we assume that the change in temperature and wall thickness is sufficiently small, we can do a first order Taylor expansion of Eq. (A.11) around  $(\hat{T}_{j-1}, \hat{y}_{st,j-1}^0)$ :

$$\tau_{k,j} \approx (k \cdot B_j + A_j) \cdot (T_j - \hat{T}_{j-1}) + k \cdot C_j \cdot (y_{st,j}^0 - \hat{y}_{st,j-1}^0) \quad (\text{A.16})$$

where

$$\begin{aligned} A_j &= \frac{2y_f^0 \left( \alpha \cdot c_f(\hat{T}_{j-1}) - (1 + \alpha \Delta \hat{T}) \sum_{n=1}^N n \gamma_n \hat{T}_{j-1}^{n-1} \right)}{c_f(\hat{T}_{j-1})^2} \\ B_j &= \frac{2\hat{y}_{st,j-1}^0 \left( (\alpha \cdot c_{st}(\hat{T}_{j-1}) - (1 + \alpha \Delta \hat{T}) \sum_{n=1}^2 n \varphi_n \hat{T}_{j-1}^{n-1}) \right)}{c_{st}(\hat{T}_{j-1})^2} \\ C_j &= 2 \left( 1 + \alpha(\hat{T}_{j-1} - T_0) \right) / c_{st}(\hat{T}_{j-1}) \end{aligned} \quad (\text{A.17})$$

Here  $\Delta \hat{T} = \hat{T}_{j-1} - T^0$ . The error of this approximation is easily calculated by subtracting the right-hand side of Eq. (A.16) with Eq. (A.10). If we assume that the delay estimate  $\hat{\tau}_k$  (dropping the subscripts  $i$  and  $j$ ) has a Gaussian distribution, and assume independent measurement noise, we can calculate the joint probability density function as

$$f_{\hat{\tau}} = \frac{1}{(2\pi)^{(N-1)/2}} \prod_{k=0}^{N-1} \frac{1}{\sigma_k} e^{-\frac{(\hat{\tau}_k - \tau_k)^2}{2\sigma_k^2}} \quad (\text{A.18})$$

Now we can apply the maximum likelihood estimator which states that the minimum variance estimate is given by

$$(\hat{T}_j, \hat{y}_{st,j}^0) = \arg \max_{T_j, y_{st,j}^0} f_{\hat{\tau}_k} = \arg \min_{T_j, y_{st,j}^0} \sum_{k=0}^{N-1} \frac{(\hat{\tau}_{k,j} - \tau_{k,j})^2}{2\sigma_k^2} \quad (\text{A.19})$$

By doing the Taylor approximation, the estimate reduces to a weighted least squares estimate where the weights are given by the inverse of the variance. For this linearized problem, we can apply the normal equations for a computational efficient solution:

$$\begin{aligned} (\mathbf{X}_j^T \mathbf{W}_j \mathbf{X}_j) \hat{\chi}_j &= \mathbf{X}_j^T \mathbf{W}_j \hat{\tau}_j \\ \Rightarrow \hat{\chi}_j &= (\mathbf{X}_j^T \mathbf{W}_j \mathbf{X}_j)^{-1} \mathbf{X}_j^T \mathbf{W}_j \hat{\tau}_j \end{aligned} \quad (\text{A.20})$$

We see that in the general case, the measurement noise,  $\mathbf{W}_j$ , is updated at each time-step. One approach for adaptive noise covariance estimation is given

in [16]. Herein it is however assumed that the variances are known *a-priori*, and that they are constant, hence  $\mathbf{W}_j = \mathbf{W}$  in the rest of this paper. From Eqs. (A.16)-(A.20) we see that

$$\mathbf{X}_j = \begin{bmatrix} A_j & 0 \\ A_j + B_j & C_j \\ A_j + 2B_j & 2C_j \\ \vdots & \vdots \\ A_j + (N-1)B_j & (N-1)C_j \end{bmatrix}$$

$$\mathbf{W} = \begin{bmatrix} \frac{1}{\sigma_0^2} & 0 & 0 \\ 0 & \ddots & \vdots \\ 0 & \cdots & \frac{1}{\sigma_{N-1}^2} \end{bmatrix}, \hat{\tau}_j = \begin{bmatrix} \hat{\tau}_{0,j} \\ \vdots \\ \hat{\tau}_{N-1,j} \end{bmatrix} \quad (\text{A.21})$$

$$\hat{\chi}_j = \begin{bmatrix} \Delta \hat{T}_j \\ \Delta \hat{y}_{st,j}^0 \end{bmatrix} = \begin{bmatrix} \hat{T}_j - \hat{T}_{j-1} \\ \hat{y}_{st,j}^0 - \hat{y}_{st,j-1}^0 \end{bmatrix}$$

The complete algorithm is given here:

### 1. Initialization

- (a) Record the initial measurement,  $s_0$ .
- (b) Given the standoff,  $y_f$ , and a coupling fluid with the well defined function  $c_f(T)$ , estimate from  $s_0$  the initial temperature as well as the initial wall thickness using (A.4) and (A.14) respectively.
- (c) Identify the echoes,  $x_k$ , you want to use in the estimation scheme.

### 2. For each $j$ do:

- (a) Record a new measurement  $s_j$ .
- (b) Estimate the delay between each echo in  $s_{j-1}$  and  $s_j$  using Eq. (B.13).
- (c) Update the coefficients  $A_j$ ,  $B_j$  and  $C_j$  as well as the matrices  $\mathbf{X}_j$  and  $\hat{\tau}_j$ .
- (d) Estimate  $\Delta \hat{y}_{st,j}^0$  and  $\Delta \hat{T}_j$  using Eq. (A.20).
- (e) Update the current estimate of the wall-thickness and temperature using  $\hat{y}_{st,0,j} = \hat{y}_{st,0,j-1} + \Delta \hat{y}_{st,j}$  and  $\hat{T}_j = \hat{T}_{j-1} + \Delta \hat{T}_j$ .

In order to utilize this algorithm, the following a-priori information are needed: a) The standoff,  $y_f$ , b) the speed of sound in the fluid and steel as a function of temperature, c) thermal expansion coefficient for the steel, d) the variances for the delays and e) the thermal effects on  $y_f$ . A block diagram of the algorithm is presented in Figure A.3. Note that the algorithm requires at least two echoes in order to work; the front wall echo and the first back wall echo. If more observations are incorporated, the system of equations in Eq. (A.20) are over-determined which according to theory [17] should lead to a higher resolution due to increased noise suppression as long as the model is correct.

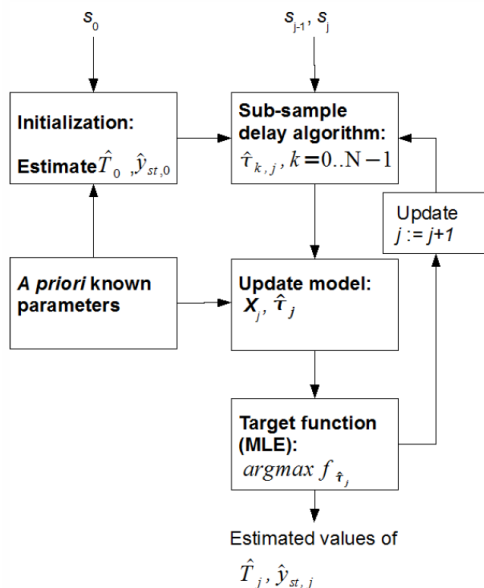


Figure A.3: A block diagram of the proposed algorithm.

#### A.2.4 Corrosion rate vs. rate of change in temperature

A method for estimating  $T$  and  $y_{st}^0$  has been proposed. The most interesting parameter to the corrosion engineer though, is the true corrosion rate,  $a_{corr} = -\partial y_{st}^0 / \partial t$ , where  $t$  is the time variable. If one already has obtained  $y_{st}^0$ , the real-time corrosion rate using e.g. a Kalman-filter as shown in [9] can be estimated. If the temperature varies relatively slowly with time (i.e. the effect of the temperature is much less than the effect of the corrosion), temperature

compensation is not that important. However, if the opposite is true, compensation is necessary in order to estimate the correct corrosion rate. To analyze this, consider the erroneous uncompensated wall thickness:

$$y_{st,\varepsilon}(T, t) = c_{st}(T^o) \cdot y_{st}(T, t) / c_{st}(T) \quad (\text{A.22})$$

As the temperature is a function of  $t$ , the total derivative of A.22, which also gives the erroneous corrosion rate,  $a_{corr,\varepsilon}$ , is expressed by

$$\frac{dy_{st,\varepsilon}}{dt} = -a_{corr,\varepsilon} = \frac{\partial y_{st,\varepsilon}}{\partial T} \frac{\partial T}{\partial t} + \frac{\partial y_{st,\varepsilon}}{\partial t} . \quad (\text{A.23})$$

Note that  $d/dt$  is the total derivative operator, while  $\partial/\partial t$  is the partial derivative operator. The erroneous corrosion rate is then given by

$$\begin{aligned} \varepsilon &= \frac{dy_{st,\varepsilon}}{dt} - \frac{\partial y_{st}^0}{\partial t} \\ &= \frac{\left[ \alpha y_{st}^0 \cdot c_{st}(T) - \sum_{n=1}^2 n \varphi_n T^{n-1} y_{st}(T) \right] c_{st}(T^0)}{c_{st}(T)^2} \frac{\partial T}{\partial t} \\ &\quad + (c_{st}(T^0) \cdot (1 + \alpha \Delta T) / c_{st}(T) - 1) \frac{\partial y_{st}^0}{\partial t} \end{aligned} \quad (\text{A.24})$$

From Eqs. (A.23)-(A.24) the requirements needed with respect to the temperature compensation scheme for realistic values of  $\partial y_{st}^0/\partial t$  and  $\partial T/\partial t$  can be investigated. In order to estimate  $y_{st,\varepsilon}$  and  $a_{corr,\varepsilon}$ , a direct correlation scheme (DC) is applied. DC calculates the delay based on correlating two subsequent echoes with sub-sample interpolation, and estimates the wall thickness based on a constant sound speed. Hence DC calculates the new thickness for each new measurement. For measurements where the temperature is kept constant, DC is considered as the ground truth. Note the conceptually different way of estimating the wall thickness for DC and CMTC; while the former calculates a new wall thickness for each measurement, the latter estimates the difference between the former and current measurement and updates the wall thickness estimate based on that.

### A.3 Experimental procedure

For many pulse-echo applications, multiple reflections from internal and external interfaces are exploited in order to determine layer thicknesses with a required accuracy [18]. When it comes to corrosion monitoring, it is the relative reduction of the wall thickness which is of main importance, i.e. the change

from one time instant to the next. In order to obtain repeatable measurements and high resolution, the transducer should be fixed with respect to the steel.

For testing CMTC a focused Imasonic immersion transducer with 5MHz center frequency, 10mm aperture and 50mm focal distance has been positioned in a cylindrical test cell with radius 35mm. The test cell has an end cap made of carbon steel fixed perpendicularly to the transducer axis. The test cell was flexible with respect to both steel thickness and standoff between the transducer and the steel. Further, the test cell was filled with a mixture of de-ionized water and EG. Different ratios of water and EG has been tested. This liquid has two main purposes; a) it will function as a contact fluid between the transducer and the steel and b) it will prevent corrosion on the sensor-side of the steel block. Another benefit with the mixture is that the attenuation is low and approximately constant with temperature, at least for the temperatures studied herein. The ultrasonic beam was aligned perpendicularly to the sample surface by maximizing the amplitude of the first echo. A caliper was used for determining the standoff between the transducer and the steel.

The test cell was immersed into a 100dm<sup>3</sup> tank filled with a corrosive electrolyte. As corrosion is a very slow process, for experimental purposes it is more convenient to employ accelerated corrosion. Herein, the corrosiveness was adjusted either by using an impressed current (anodic direction) or by changing the pH of the solution (a lower pH increases the corrosion rate of carbon steel). For the former method, note that corrosion of steel is an electrochemical reaction where iron ( $Fe$ ) is oxidized to ions ( $Fe^{2+}/Fe^{3+}$ ) by giving away electrons. The flow of electrons can be stimulated by using an impressed current and the resulting corrosion rate can be estimated in mm/year by applying Faraday's law [19].

$$a_{corr} = -\partial y_{st}^0 / \partial t = 3268 \cdot i_{corr} \cdot M / (z\rho). \quad (A.25)$$

Here  $i_{corr}$  denotes the impressed current density in A/cm<sup>2</sup>.  $M = 55.8$ g/mol is the mol weight of the actual alloy,  $z$  is the number of valence electrons and  $\rho = 7.85$ g/cm<sup>3</sup> is the density of steel. As the iron is oxidized both to  $Fe^{2+}$  and  $Fe^{3+}$ , a common practice is to set  $z = 2.67$ . Platinum is used as a counter electrode in order to minimize unwanted chemical reactions. The power supply must be connected with the positive voltage connected to the steel (anode) and the negative voltage connected to the platinum (cathode). The platinum thread is symmetrically positioned with respect to the exposed steel surface so that the corrosion shall occur as smooth as possible. With impressed current two achievements can be made: a) The measured corrosion rate can be compared with the theoretical corrosion rate quantitatively, and b) equally important is

the qualitative measure stating that the corrosion rate increases linearly with current.

An immersion heater was used for regulating the temperature in the electrolyte. A Dallas DS1621V thermometer covered with a thin epoxy-layer and a pump was submersed in the electrolyte for temperature readings near the test cell and to ensure circulation respectively. The circulation contributes to keep a constant temperature gradient in the tank as well as to remove rust-deposits on the exposed steel surface. The experimental setup is conceptually presented in Figure A.4. With this setup, it is clear that only the side of the steel sample in contact with the electrolyte is exposed to corrosion. This is similar to e.g. pipelines where it is the internal corrosion that is most relevant.

The transducer is excited with a 60V 1-cycle square pulse. On the receive part, an AD8332 ultra-low noise preamp is connected to a LTC2298 50Msp/s 14bit analog to digital converter. The digitized data are stacked 128 times before transferred over a RS485/RS232 bus to a PC for further examination. The processing is performed in Matlab (Mathworks, Massachusetts, USA).

Pulse-echo experiments have been performed in order to measure the sound speed in mixtures between water and EG for temperatures in the range 10-90°C. The results from two experiments with different volume fractions are shown in Table A.2. For mixtures with ratios comparable to that found in the literature [20, 21], a good correspondence has been found. The analysis has revealed two main problems: a) Very small changes in wall thickness should be detected; the smaller the better. b) Even small temperature variations will distort the wall thickness and corrosion rates estimates. This should be compensated for.

Table A.2: Temperature coefficients.

	$\varphi_0$	$\varphi_1$	$\varphi_2$
Steel	6008.1	-0.46	0.000
	$\gamma_0$	$\gamma_1$	$\gamma_2$
Pure EG (>95%)	1715.8	-2.38	0.000
EG - water, 50%-50%	1712.0	-0.768	-0.0081
EG - water, 67%-33% <sup>a</sup>	1648.6	1.046	-0.015

<sup>a</sup> Taken from [20].

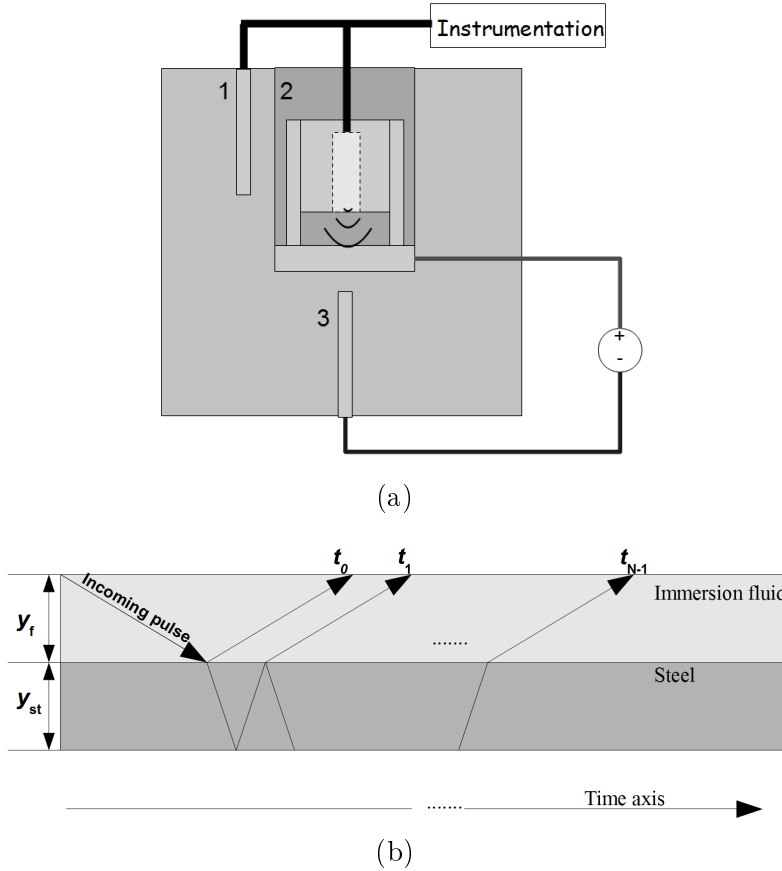


Figure A.4: a) Experimental setup. 1: Thermometer 2: Transducer fixture with coupling fluid submersed in electrolyte. 2: Platinum electrode (cathode). b) A schematic figure of the received reflections. ( $y_f$ ,  $y_{st}$ : Thicknesses of the layers;  $t_k$ ,  $k = 0..N - 1$ : Time instants of the reflections.)

## A.4 Results and discussion

### A.4.1 Error introduced if no temperature compensation is performed

Equation (A.24) gives the relationship between, amongst other,  $\partial T/\partial t$ ,  $a_{corr}$  and the error,  $\varepsilon$ . Inserting values reflecting the material properties used in the experiments gives the following relation:

$$\begin{aligned}\varepsilon &= 12.9 \cdot \partial T / \partial t - 4.7 \cdot 10^{-4} a_{corr}(T = 30^\circ\text{C}) \\ \varepsilon &= 12.9 \cdot \partial T / \partial t - 7.3 \cdot 10^{-3} a_{corr}(T = 100^\circ\text{C}) .\end{aligned}\tag{A.26}$$

Here  $\partial T / \partial t$  is given in  $^\circ\text{C}/\text{hour}$  while  $a_{corr}$  is given in  $\text{mm}/\text{year}$ . Two observations can be made from (A.26): a) The value of  $T$  is only significant for the coefficient in the  $2^{nd}$  term. (Note that the coefficient in the  $2^{nd}$  term is monotonic decreasing.) Hence the coefficient in the  $1^{st}$  term can be assumed constant for all  $T$ 's. b) For realistic values of  $\partial T / \partial t$  (e.g.  $1^\circ\text{C}/\text{hour}$ ) and  $a_{corr}$  (e.g.  $0.1 \text{ mm}/\text{year}$ ), the  $1^{st}$  term will totally dominate. Hence the  $2^{st}$  term can be neglected. This means that  $\varepsilon$  is nearly independent of  $\Delta T$  and that only  $\partial T / \partial t$  gives a significant contribution. A plot of  $\varepsilon$  as a function of  $\partial T / \partial t$  is presented in A.5. It is clear that even small temperature derivatives give rise to large errors compared to realistic corrosion rates. An example is that if  $\partial T / \partial t = 0.008^\circ\text{C}/\text{hour}$ , then  $\varepsilon = 0.1 \text{ mm}/\text{year}$  which is comparable to typical corrosion rates. The standard deviation of the temperature estimates for CMTC is estimated to  $0.003^\circ\text{C}$  indicating that very small temperature variations can be detected.

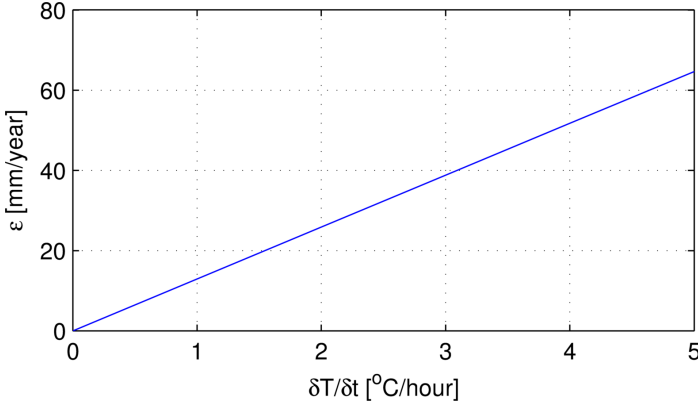


Figure A.5:  $\varepsilon$  as a function of  $\partial T / \partial t$ .

#### A.4.2 Test 1: Constant temperature experiment

In the  $1^{st}$  test, pure EG was used, and the temperature was held constant at  $21.5^\circ\text{C}$ . During the first part of the test  $i_{corr} = 5 \text{ mA}/\text{cm}^2$  while it was doubled to  $10 \text{ mA}/\text{cm}^2$  in the latter half. The wall thickness development of both  $y_{st}^0$  and  $y_{st,\varepsilon}$  is presented in Figure A.6 and it is seen that they are approximately equal. Hence CMTC operates as desired for constant temperatures.

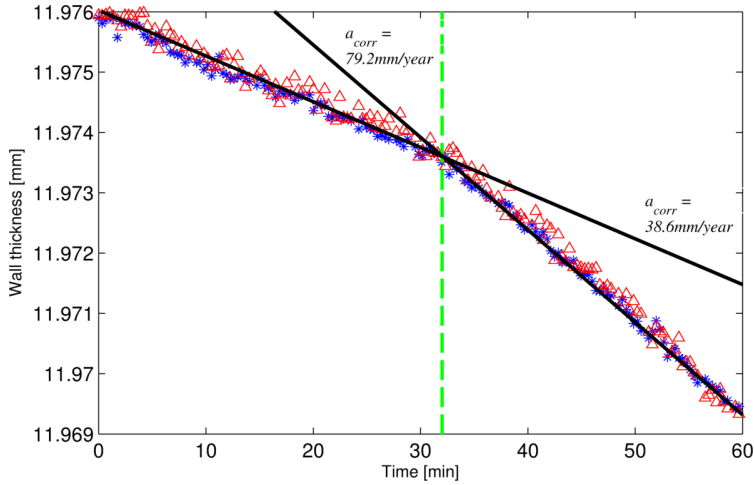


Figure A.6: Test 1: The plot illustrates the wall thickness development at constant temperature. The triangles ( $\Delta$ ) show the development using DC, while the stars (\*) show the same with CTCM. The dashed line indicates the time-instant for which the impressed current-density is doubled from  $5\text{mA}/\text{cm}^2$  to  $10\text{mA}/\text{cm}^2$ . The solid lines show the linear regression curves for the two current-densities together with the corresponding estimated corrosion rate.

As long as the current density is constant, the corrosion rate is also assumed constant. Thus we can estimate  $a_{corr}$  and the related confidence intervals based on linear regression. This is shown in Table A.3. The corrosion rate based on CMCT is  $38.4\text{mm}/\text{year}$  and  $79.2\text{mm}/\text{year}$  for  $i_{corr} = 5\text{mA}/\text{cm}^2$  and  $10\text{mA}/\text{cm}^2$  respectively. According to Eq. (A.25), the ratio of the corrosion rates should be the same as the ratio of the impressed currents (since we have assumed self corrosion to be negligible). In this case, the measured ratio is  $38.7/79.2 = 0.487$  which is less than 2.6% deviation from the theoretical ratio of 0.5. Qualitatively, a very good accordance between theory and measurements is hence achieved.

There is a good agreement between the theoretical and estimated corrosion rates with the latter systematically about 6-10% lower. Some possible error sources are: a) Equation (A.25) assumes a constant corrosion rate over the exposed steel surface. Local effects can occur, resulting in different rates on various spatial positions on the steel surface. Local effects can both increase and decrease  $a_{corr}$  compared to the calculated value. b) Surface roughness on the exposed area may increase the total surface area. c) Some of the electrons may react in other reactions, such as dissolution of other ions or oxygen evolution at the anode. d) Rust deposits such as iron oxide may form on the steel surface

causing a small change in the pulse-form. Deposits are indeed observed by visual inspection during the experiments. For b), c), and d)  $a_{corr}$  will be lower than what is predicted with (A.25). Thus we see that most of the error sources tend to decrease compared to what is calculated, a fact which is supported by the results.

Table A.3: Estimated and theoretical corrosion rates and the estimated temperature derivative.

Experimental information	$\hat{a}_{corr}^a$	$\hat{a}_{corr,\varepsilon}$	$\hat{\varepsilon}$	$\partial\hat{T}/\partial t^b$	$a_{corr}^c$	$\varepsilon$
Test 1: $i_{corr} = 5\text{mA}/\text{cm}^2$ (0-32min)	38.6±1.0	38.5±1.7	0.2	0.01±0.02	43.0	0.1
Test 1: $i_{corr} = 10\text{mA}/\text{cm}^2$ (32-60min)	79.2±1.3	79.2±3.0	0.0	0.01±0.02	86.0	0.1
Test 2: $i_{corr} = 10\text{mA}/\text{cm}^2$ (0-65min)	81.7±0.4	54.6±0.6	-27.1	2.25±0.02	86.0	-29
Test 2: $i_{corr} = 5\text{mA}/\text{cm}^2$ (65-175min)	39.3±0.2	47.0±0.4	7.9	-0.58±0.01	43.0	7.5
Test 2: $i_{corr} = 0\text{mA}/\text{cm}^2$ (175-min)	-0.19±0.6	5.8±1.1	6.0	-0.48±0.00	0.0	6.2

<sup>a</sup> The corrosion rates and  $\varepsilon$  are given in mm/year. All uncertainties are given in 95% confidence intervals. The regression is taken over an interval where  $\partial\hat{T}/\partial t$  is approximately constant, and not necessarily over the whole time interval indicated in the parenthesis. The estimated parameters are indicated with a  $\hat{\phantom{x}}$  (e.g.  $\hat{a}_{corr}$ ).

<sup>b</sup>  $\partial T/\partial t$  is given in  $^{\circ}\text{C}/\text{hour}$ .

<sup>c</sup> These values are calculated by using Eq. (A.25). Self corrosion due to the corrosive electrolyte will occur as well, but that is assumed negligible in this case.

Other acoustic errors sources which are assumed negligible are: a) Varying surface roughness during corrosion can cause pulse distortion and hence an error in the delay estimation. b) Attenuation is assumed constant with temperature. c) The diffraction of the acoustic pulse will be temperature dependent. For the relatively small temperature variations investigated in the current work, no pulse distortion has been visually observed.

### A.4.3 Test 2: Varying temperature experiment

In the 2<sup>nd</sup> test, pure EG was used and both  $i_{corr}$  and  $T$  varied as shown in Table A.3 and Figure A.7. The temperature estimate using CMTC clearly follows the temperature measured by the thermometer, but it is in particular one main source of error; the assumption of a constant temperature in the

electrolyte, coupling fluid and steel. When the temperature in the electrolyte changes, a temperature gradient will arise in the test cell causing a true relation between the tof and  $c_f$  as calculated by Eq. (A.13). A consequence of this is an error in the temperature estimation; when the temperature increases (decreases) in the electrolyte, an underestimation (overestimation) will occur because the temperature will be lower (higher) in the coupling fluid than in the steel. This phenomenon is seen in Figure A.7. If in addition  $\partial T/\partial t$  is different in the steel and in the contact fluid, an erroneous value of  $a_{corr}$  is estimated. A more detailed study of this requires investigating the heat equation and how the temperature gradient and  $\partial T/\partial t$  relates for the specific setup. Then it may be possible to invert the measured temperature development in the fluid back to the true temperature in the steel increasing the accuracy of the compensation scheme. Such a study is not considered in the scope of this work.

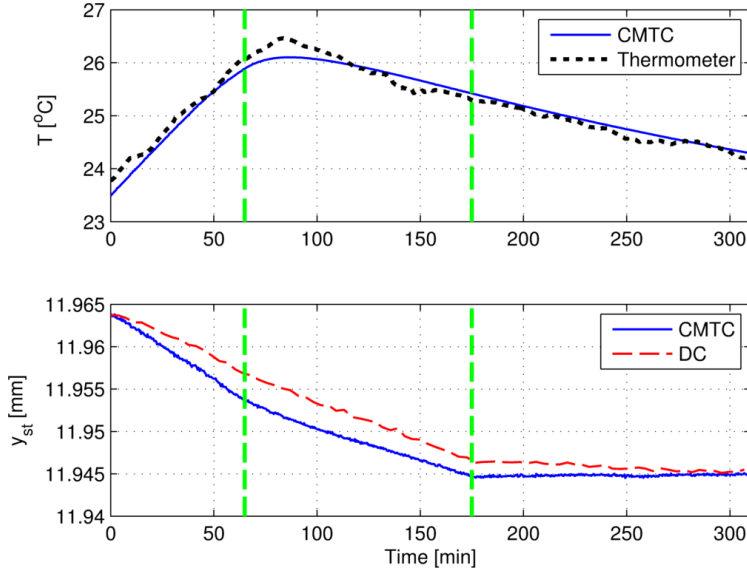


Figure A.7: In the upper plot the estimated- versus the measured temperature is presented. In the lower plot the estimated wall thickness using CMPT and DC is shown. The vertical dashed lines show the time instants for which  $i_{corr}$  change; first from 10 to 5mA/cm<sup>2</sup>, and then from 5 to 0mA/cm<sup>2</sup>.

When estimating the wall thickness, the lower plot of Figure A.7 illustrates different developments for DC and CMTC respectively. In the first period from 0-65min,  $\hat{a}_{corr,\varepsilon}$  is lower than  $\hat{a}_{corr}$  due to the increasing temperature. For the two latter periods, the opposite is true due to the decreasing temperature.

Note that for the second period, the regression is taken between 120min and 175min because it is important that  $\partial T/\partial t$  is approximately constant.  $\partial T/\partial t$  is estimated in order to compare  $\varepsilon$  with the estimated error,  $\hat{\varepsilon} = \hat{a}_{corr} - \hat{a}_{corr,\varepsilon}$ . (Note that  $\hat{a}_{corr}$  is roughly the same even if time intervals where  $\partial^2 T/\partial t^2 \neq 0$  is incorporated in the calculation.) Table A.3 shows that there is a good match between  $\hat{\varepsilon}$  and  $\varepsilon$ . Comparing the theoretical  $a_{corr}$  with the estimated  $\hat{a}_{corr}$  shows approximately the same systematic deviation as for the constant temperature test, but still it is a good agreement. Further, when comparing  $\hat{a}_{corr}$  for the 1<sup>st</sup> and 2<sup>nd</sup> test at equivalent current densities, the difference is 1.5% and 3% for 5mA/cm<sup>2</sup> and 10mA/cm<sup>2</sup> respectively. These results indicate the efficiency of the temperature compensation scheme.

It is worth noting that each step on the range-axis is 1 $\mu$ m and 5 $\mu$ m in Figure A.6 and Figure A.7 respectively, and the resolution is clearly in the sub micrometer scale. When it comes to resolution in general, Eq. (A.20) indicates that by incorporating more echoes in the calculation, a better estimate of the wall thickness may be obtained. Table A.4 shows standard deviations from a linear trend in nanometer (nm) as a function of number of echoes employed in the calculation for three cases: 1) Only  $a_{corr} > 0$ . These values are calculated based on the first 32min in the constant temperature test. 2) Only  $\partial T/\partial t \neq 0$ . These values are calculated based on the last part of Test 2 where only the temperature changes. 3) Both  $a_{corr} > 0$  and  $\partial T/\partial t \neq 0$ . These values are calculated based on data between 120- and 170min in Test 2. From the results it seems that by incorporating more echoes a better resolution is obtained, which is according to theory. But the picture is not all that clear. E.g. in the 2<sup>nd</sup> case, 3 echoes have the best standard deviation. It also seems that the standard deviation is less when the corrosion is zero. This may be caused by noise from the impressed DC current which is turned off in the case of no corrosion, or from the fact that the corrosion rate is not a true constant; it may vary slightly over time causing a deviation from the linear trend. In general, 5 echoes are used in the current work.

Table A.4: Standard deviation as a function of incorporated echoes.

Number of echoes	Standard deviation, $\sigma$ [nm]		
	$a_{corr} > 0$	$\partial T/\partial t \neq 0$	$a_{corr} > 0$ and $\partial T/\partial t \neq 0$
2	195	82	181
3	118	74	145
4	91	78	145
5	86	78	142

#### A.4.4 Test 3: Low corrosion rate experiment

When using impressed current, high current densities are important in order to make  $a_{corr}$  the dominant factor compared to other error sources. In Figure A.8 results from an experiment with more realistic corrosion rates and a 67%-33% EG-water mixture as coupling fluid are presented. Here,  $a_{corr}$  is varied by altering the pH in the solution; for  $\text{pH} < 7$ , decreasing (increasing) the pH causes an increase (decrease) in the corrosion rate. The drawback with the method is that the theoretical corrosion rate is difficult to estimate. The upper plot shows that the estimated temperature corresponds very well to the measured temperature. In the first 1350min of the experiment, the pH equals 4 with  $\hat{a}_{corr}$  around 0.4mm/year. At the indicated time instant at 1350min, the pH is decreased to 3, causing  $\hat{a}_{corr}$  to increase to 3mm/year. It is clear that the thermal error (here  $|\partial T/\partial t| < 0.3^\circ\text{C}/\text{hour}$ ) in some time intervals dominates over the wall thickness loss, leading to periods where the thickness seems to increase when using DC. Even for such low corrosion rates, CMTC removes most of the thermal error and a more realistic corrosion rate is obtained.

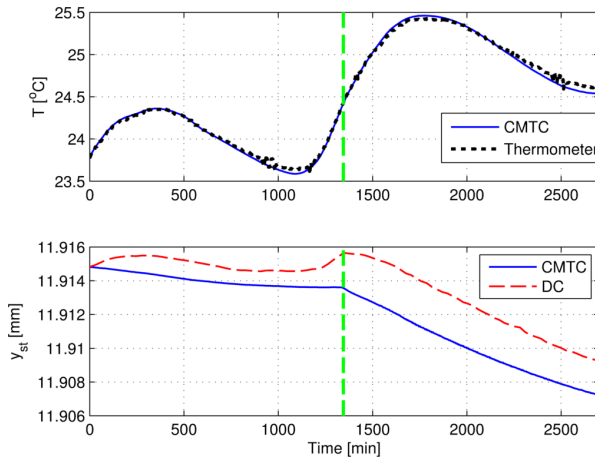


Figure A.8: In the upper plot the estimated- versus the measured temperature is presented. In the lower plot the estimated wall thickness using CMTC and DC is shown. The vertical dashed line show the time instant where the pH is reduced from 4 to 3.

#### A.4.5 Verification with contact micrometer

The accumulated wall loss from the steel sample has been measured using a contact micrometer. In order to decrease the uncertainty ( $\pm 5\mu\text{m}$ ) of the

contact micrometer readings relative to the change in wall thickness, a separate experiment with a relatively large accumulated loss is performed. The measured accumulated losses at 3 spots near the ultrasound footprint are  $50\mu\text{m}$ ,  $50\mu\text{m}$  and  $52\mu\text{m}$  using the contact micrometer (average of  $51.3\mu\text{m}$ ), while it is  $53\mu\text{m}$  if we use CMTC. This result indicates an excellent agreement between CMTC and contact micrometer readings.

The reason why the accumulated losses are less when using the contact micrometer may be because of the surface roughness. The contact micrometer will always measure the thickest point under its footprint while the ultrasound measurement gives an average. Thus if the roughness increases during the experiment, the measured accumulated wall thickness may be larger for the ultrasound measurement.

#### A.4.6 Error due to linearization

The linearization in Eq.(A.16) introduces an error which can be calculated by subtracting the true- and approximated delay. Figure A.9 shows that the error introduced from the fluid is 100 times larger than from the steel. As an example, consider the large temperature step of  $15^\circ\text{C}$  from one measurement to the next which causes approximately 1ns and 0.01ns error in  $\tau_0$  and  $\tau_{st}$  respectively. This corresponds to an error of  $0.03^\circ\text{C}$  in the estimated temperature. For the estimated wall thickness we get two error contributions: a) From the linearization error of  $\tau_{st}$  directly and b) indirectly from  $\tau_0$  through the erroneous temperature compensation. The former error is 30nm while the latter is 60nm. This adds up to 90 nm which is comparable to the standard deviation of the thickness measurements. If, however, the measuring interval is small compared to  $\partial T/\partial t$  and  $\Delta T$  e.g. is less than  $1^\circ\text{C}$ , the linearization errors will be negligible. Accumulating errors may be an important aspect for long term applications, but that is considered as future work. In relation to e.g. corrosion monitoring of petroleum pipelines, the really large temperature deviations usually occur in connection with shut-down operations.

#### A.4.7 Uncertainty analysis

Here we investigate how the initial parameter errors translate into the final accuracy of  $T$  and  $y_{st}^0$ . We assume type B uncertainty [22], that a first order polynomial describes the temperature dependence of the sound speed in the fluid/steel and that we can disregard thermal expansion, i.e.  $y_{st}(T) \approx y_{st}^0$ ,  $y_f(T) \approx y_f^0$ , in order to simplify the analysis. For steel, the ratio of influence due to sound speed compared to expansion is about 8:1. For EG this ratio is above 100:1.

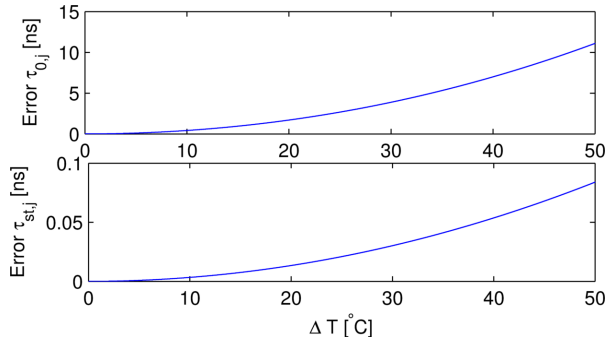


Figure A.9: Linearization errors in nanoseconds (ns). In the upper plot the error for the delay in the fluid is shown as a function of temperature step. In the lower plot the same is presented for the delay in the steel. It is assumed that  $y_{st}^0 = 12\text{mm}$ ,  $y_f = 20\text{mm}$  and that pure EG is used.

Hence the thermal change in sound speed is the dominant factor, and the approximation is sound. The fundamental factor in the uncertainty analysis of a function  $f(p_1, p_2 \dots p_n)$ , where  $p_i$  is parameter  $i$ , is the sensitivity given as  $S_{f,p_i} = \partial f / \partial p_i$ . The combined standard uncertainty of  $f$  for independent contributions is now given as

$$u_c(f) = \sqrt{\sum_i S_{f,p_i}^2 \cdot u^2(p_i)} = \sqrt{\sum_i u_f^2(p_i)} \quad (\text{A.27})$$

where  $u(p_i)$  is the type B uncertainty of  $p_i$  and  $u_f(p_i) = S_{f,p_i} \cdot u(p_i)$  reflects the uncertainty translated into  $f$  from  $p_i$ . In order to be able to compare the sensitivities of different parameters, it is adequate to normalize  $S_{f,p_i}$ , giving the normalized sensitivity  $\bar{S}_{f,p_i} = |p_i/f \cdot \partial f / \partial p_i|$ . Starting from Eq. (A.14) and solving with respect to  $T$ , we obtain an equation which depends on 4 parameters:  $T(y_f^0, t_0, \gamma_0, \gamma_1) = (2y_f^0 - \gamma_0 t_0) / \gamma_1 t_0$ . Similarly, by inserting the equation for  $T$  into Eq. (A.4) we obtain an equation of 7 parameters for  $y_{st}^0$  giving:

$$y_{st}^0(y_f^0, t_0, \gamma_0, \gamma_1, \delta_{st}, \varphi_0, \varphi_1) = (t_0(\varphi_0 \gamma_1 - \varphi_1 \gamma_0) + \varphi_1 2y_f^0) \cdot \delta_{st} / (2\gamma_1 t_0) \quad (\text{A.28})$$

From Eq. (D.15) and Eq. (A.28), the partial derivatives of  $T$  and  $y_{st}^0$  with respect to its parameters can be found and the according normalized sensitivities calculated. This is shown together with the uncertainty of each parameter in Table A.5. We can deduce that  $T$  is most sensitive to  $t_0$ ,  $\gamma_0$  and  $y_{st}^0$  and

that for the given uncertainties,  $t_0$  contributes most to  $u_c(T)$ . We can also see that  $y_{st}^0$  is most sensitive to  $\varphi_0$  and  $\delta_{st}$  and that these parameters contributes to nearly 100% of  $u_c(y_{st}^0)$ . From Eq. (D.15) we obtain  $u_c(T) = 0.7^\circ\text{C}$  and  $u_c(y_{st}^0) = 65\mu\text{m}$ . By perturbing the parameters in CMTC accordingly and calculate the resulting  $a_{corr}$ , we can find  $u_{a_{corr}}(p_i)$ . Since it is assumed, based on Eq. (A.24), that  $u_{a_{corr}}(p_i)$  also is a function of  $\partial T/\partial t$  and  $a_{corr}$ ,  $u_{a_{corr}}(p_i)$  is found in 4 different cases. From the constant temperature case, it is seen that  $\varphi_0$  contributes to almost all the uncertainty and that the uncertainty increases with  $a_{corr}$  which is expected. The latter means that for realistic values of  $a_{corr}$ , the uncertainty will be very small. It can also be noted that even though  $\delta_{st}$  contributes to 60% of  $u_c(y_{st}^0)$ , it does not contribute significantly to  $u_c(a_{corr})$ . Hence, a slight bias in the absolute thickness estimate does not influence the estimate of the relative change in thickness notably. When the temperature varies, we see that in addition to the contribution from  $\varphi_0$ , we also have two significant contributions from  $\varphi_1$  and  $\gamma_1$  for which the contribution increases with  $\partial T/\partial t$ . This is logical, since it is  $\varphi_1$  and  $\gamma_1$  which determine how the sound speed changes with temperature. A more elaborate uncertainty analysis is considered as future work.

Table A.5: Results from uncertainty analysis.

$p_i$	$\bar{S}_{T,p_i}$	$\bar{S}_{y_{st},p_i}^0$	$u(p_i)$	$u_T(p_i)$	$u_{y_{st}^0}(p_i)$	$u_{a_{corr}}(p_i)^b$	$u_{a_{corr}}(p_i)^c$	$u_{a_{corr}}(p_i)^d$	$u_{a_{corr}}(p_i)^e$
$t_0$	27.8	0.06	20ns	0.57 (65%) <sup>a</sup>	0.6 (0%)	0.00 (0%)	0.00 (0%)	0.02 (0%)	0.05 (8%)
$\gamma_0$	28.8	0.06	0.7m/s	0.29 (17%)	0.3 (0%)	0.00 (0%)	0.00 (0%)	0.00 (0%)	0.00 (0%)
$\gamma_1$	1.0	0.00	$\approx 1\%$	0.25 (12%)	0.3 (0%)	0.01 (2%)	0.01 (0.5%)	0.21 (24%)	0.06 (11%)
$y_f^0$	27.8	0.06	5 $\mu\text{m}$	0.17 (6%)	0.2 (0%)	0.00 (0%)	0.00 (0%)	0.00 (0%)	0.00 (0%)
$\varphi_0$	-	1	13m/s	-	26 (16%)	0.08 (96%)	0.17 (99%)	0.31 (52%)	0.15 (70%)
$\varphi_1$	-	0.00	$\approx 1\%$	-	0.3 (0%)	0.01 (2%)	0.01 (0.5%)	0.18 (18%)	0.05 (8%)
$\delta_{st}$	-	1	20ns	-	60 (84%)	0.00 (0%)	0.00 (0%)	0.10 (6%)	0.03 (3%)

<sup>a</sup> The values in the parenthesis indicate the relative contribution to the total uncertainty, i.e.  $u_j^2(p_i)/u_c^2(f) \cdot 100\%$ .

<sup>b</sup> Based on the 1<sup>st</sup> part of Test 1, i.e.  $\partial T/\partial t \approx 0$  and  $\hat{a}_{corr} = 38.6\text{mm/year}$ .

<sup>c</sup> Based on the 2<sup>nd</sup> part of Test 1, i.e.  $\partial T/\partial t \approx 0$  and  $\hat{a}_{corr} = 79.2\text{mm/year}$ .

<sup>d</sup> Based on the 1<sup>st</sup> part of Test 2, i.e.  $\partial T/\partial t = 2.25^\circ\text{C}$  and  $\hat{a}_{corr} = 81.7\text{mm/year}$ .

<sup>e</sup> Based on the 2<sup>nd</sup> part of Test 2, i.e.  $\partial T/\partial t = -0.58^\circ\text{C}$  and  $\hat{a}_{corr} = 39.3\text{mm/year}$ .

## A.5 Conclusions

A technique for estimating the wall thickness and temperature simultaneously from one ultrasound measurement has been investigated. The analysis has revealed the importance of temperature compensation and how even small thermal variations can give an erroneous corrosion rate if not corrected for. The main challenge has been to separate the two phenomena temperature variations and corrosion, as well as to exploit the ultrasound signal so that very

small changes in the wall thickness can be detected. The proposed method combines a sub-sample delay algorithm and a linearized MLE with a mathematical model of how the various delays relates to temperature and wall thickness. To estimate the temperature, a well defined stand-off between the steel and transducer where the coupling medium has a defined speed of sound as a function of temperature, is necessary.

The results show that the estimated corrosion rate agrees very well qualitatively and quite well quantitatively with Faraday's law. When comparing CMTC with DC, a very good match is obtained for the constant temperature case, a fact which shows that CMTC operates similar to more conventional wall thickness algorithms under that particular condition. The estimated errors between the compensated and non-compensated corrosion rates also match very well with theoretical values. An uncertainty analysis revealed that  $u_c(y_{st}^0)$  and  $u_c(T)$  was  $65\mu\text{m}$  and  $0.7^\circ\text{C}$  respectively for the current setup.  $\delta_{st}$ , which gives the major contribution to  $u_c(y_{st}^0)$ , is, however, not contributing significantly to  $u_c(a_{corr})$ .  $u_c(a_{corr})$  is empirically found to increase both with  $\partial T/\partial t$  and  $a_{corr}$ .

The developed technique can be used for non-invasive corrosion monitoring applications where high resolution and fast response is required, e.g. for monitoring of pipelines and process equipment, for lab applications etc.



# References

- [1] G. H. Koch, M. P. H. Brongers, N. G. Thompson, Y. P. Virmani, and J. H. Payer, "Corrosion costs and preventive strategies in the united states," *NACE International*, 2002.
- [2] NORSOK, *M-001 Materials Selection*. 2004.
- [3] J. Krautkramer and H. Krautkramer, *Ultrasonic Testing of Materials*. Springer-Verlag, 1983.
- [4] V. K. Kinra and C. Zhu, "Ultrasonic evaluation of thin (sub-wavelength) coatings," *The Journal of the Acoustical Society of America*, vol. 93, no. 5, pp. 2454–2467, 1993.
- [5] V. S. Agarwala and S. Ahmad, "Corrosion detection and monitoring a review," in *Proceedings of NACE Corrosion 2000, Orlando*, pp. 00271.1–00271.19, 2000.
- [6] K. Christidis and G. P. P. Gunarathne, "Temperature compensation for ultrasound measurements and characterization of materials," *Instrumentation and Measurements, IEEE Transactions on*, vol. 52, no. 5, pp. 1520–1527, 2003.
- [7] Y. Lu and J. E. Michaels, "A methodology for structural health monitoring with diffuse ultrasonic waves in the presence of temperature variations," *Ultrasonics*, vol. 43, no. 9, pp. 717–731, 2005.
- [8] T. Rommetveit, R. Johnsen, and Ø. Baltzersen, "Using ultrasound measurement for real-time process control of pipelines and process equipment subjected to corrosion and/or erosion," in *Proceedings of NACE Corrosion 2008, New Orleans*, 2008. Paper 08285.
- [9] T. Rommetveit, T. F. Johansen, R. Johnsen, and Ø. Baltzersen, "High resolution ultrasound wall thickness measurements through polyester coating

- 
- and real-time process control,” in *Proceedings of NACE Corrosion 2009, Atlanta*, 2009. Paper 09452.
- [10] Ø. Baltzersen, T. I. Waag, R. Johnsen, C. H. Ahlen, and E. Tveit, “Wall thickness monitoring of new and existing pipelines using ultrasound,” in *Proceedings of NACE Corrosion 2007, Nashville*, 2007. Paper 07333.
- [11] W.-Y. Tsai, H.-C. Chen, and T.-L. Liao, “An ultrasonic air temperature measurement system with self-correction function for humidity,” *Measurement Science and Technology*, vol. 16, no. 2, pp. 548–555, 2005.
- [12] S. R. Dooley and A. K. Nandi, “Comparison of discrete subsample time delay estimation methods applied to narrowband signals,” *Measurement Science and Technology*, vol. 9, no. 9, pp. 1400–1408, 1998.
- [13] G. Jacovitti and G. Scarano, “Discrete time techniques for time delay estimation,” *Signal Processing, IEEE Transactions on*, vol. 41, pp. 525–533, Feb. 1993.
- [14] “Asm handbook online, properties and selections: Irons, steels and high performance alloys.” [Online]. Available: <http://products.asminternational.org/hbk/index.jsp>.
- [15] C. E. Woon and L. D. Mitchell, “Temperature-induced variations in structural dynamic characteristics. part ii: Analytical,” in *SPIE, 2nd International Conference on Vibration Measurements by Laser Techniques: Advances and Applications*, pp. 58–70, 1996.
- [16] R. G. Brown and P. Y. C. Hwang, *Introduction to random signals and applied Kalman filtering*. John Wiley & Sons, 3 ed., 1997.
- [17] P. S. Maybeck, *Stochastic Models, Estimation, and Control*, vol. 1. Academic Press, Inc, 1979.
- [18] R. Raisutis, R. Kazys, and L. Mazeika, “Ultrasonic thickness measurement of multilayered aluminum foam precursor material,” *Instrumentation and Measurement, IEEE Transactions on*, vol. 57, no. 12, pp. 2846–2855, 2008.
- [19] E. Bardal, *Corrosion and protection*. Springer-Verlag, 2004.
- [20] J. Harris J Hebert, “Sound speed in water-ethylene glycol mixtures as a function of temperature and pressure,” *The Journal of the Acoustical Society of America*, vol. 49, no. 3B, pp. 930–931, 1971.

- [21] N. G. Tsierkezos and M. M. Palaiologou, “Ultrasonic studies of liquid mixtures of either water or dimethylsulfoxide with ethylene glycol, diethylene glycol, triethylene glycol, tetraethylene glycol, 1,2-propylene glycol and 1,4-butylene glycol at 298.15k,” *Physics and Chemistry of Liquids*, vol. 47, pp. 447–459, 2009.
- [22] B. N. Taylor and C. E. Kuyatt, “Guidelines for evaluating and expressing the uncertainty of nist measurement results,” 1994. Nat. Inst. Stand. Technol. , Tech. Note, pp. 1-20.



# Using a multi-layered transducer model to estimate the properties of paraffin wax deposited on steel

Tarjei Rommetveit<sup>1</sup>, Tonni F. Johansen<sup>2</sup> and Roy Johnsen<sup>1</sup>

<sup>1</sup>Department of Engineering Design and Materials, NTNU, Trondheim, Norway,

<sup>2</sup>Department of Circulation and Medical Imaging, NTNU, Trondheim, Norway

## Abstract

When using ultrasound for detecting low impedance materials on the surface of high impedance materials, a major challenge is the contrast difference between the strong reverberations from the high impedance material and the weak echoes received from the low impedance material. The purpose of this work is to present the theoretical and experimental validation of an ultrasonic methodology for estimating the acoustical properties of paraffin wax on the surface of steel. The method is based on modeling and inversion of the complete electro-acoustic channel from the transmitted voltage over the active piezoelectric element, to the received voltage resulting from the acoustic reverberations in the multi-layered structure. In the current work, two conceptually different models of the same multilayer transducer structure attached to steel is developed and compared with measurements. A method is then suggested for suppressing the strong reverberations in steel, hence isolating the wax signals. This contrast enhancement method is fitted to the model of the structure, facilitating parameter inversion from the wax layer. The results show that the models agree well with measurements and that up to three parameters (travel time, impedance and attenuation) can be inverted from the wax simultaneously. Hence, given one of the three parameters, density, sound speed or thickness, the other two can be estimated in addition to the attenuation.

## B.1 Introduction

Detection and characterization of low to medium impedance materials through a high impedance material such as steel using ultrasound may be a challenging task. The main reason is that the difference in characteristic impedance causes most of the energy to reverberate back and forth inside the high impedance material. Consequently only a small fraction of the energy will be transmitted into and reflected back from the material of interest. An eventual overlap between the weak desired echo and the strong echo from the steel further complicates the problem. Much work has been performed with respect to material characterization through metals. In [1], a windowing method is used for separating strong and weak echoes when characterizing a three-layered aluminum structure. Kinra *et al.* demonstrated in [2] how to determine phase velocity and thickness of sub-wavelength coatings through an aluminum substrate based on plane wave analysis and an inversion scheme. In [3] a technique for characterizing mineral deposits through steel is presented. By using the fact that the reflected energy at an interface is dependent on the characteristic impedances of the two materials, it is possible to characterize the type (not thickness) of the deposit by analyzing the sequence of decaying echoes in the ultrasonic waveform. Another related problem is ultrasonic monitoring of wax-deposits which can cause production losses due to restricted fluid/gas flow and eventual plugging of pipelines. Wax can precipitate in both oil- and gas pipes due to a drop of either pressure or temperature. A method for estimating the thickness of wax-deposits through gas-pipelines, based on a standard pulse-echo technique where the received signal is correlated with a reference signal and the peaks are separated in time-domain, is presented in [4]. This is a straightforward approach with some drawbacks. In the first place, the large contrast difference between the wax- and steel signal can make it difficult to identify the wax echoes, in particular if there is an overlap with the steel echo. Secondly, if the pulse length is larger than the wax thickness, it is difficult to separate two subsequent wax echoes and thus to estimate the thickness. In the current work an approach to paraffin-wax detection which addresses these challenges is presented.

When dealing with excitation of plane waves at normal incidence into a multi-layered structure, one dimensional (1D) models can be employed. To model the 1D electromechanical coupling of a piezoelectric element, the approaches of Mason [5], Redwood [6] and Krimholtz *et al.* [7] are popular. 1D models are beneficial to use as a first study of a piezoelectric transducer. For single element transducers and transducer arrays which have elements that are large compared to the wavelength such a model is a good description of the

transducer and it can e.g. be used for transducer characterization [8]. For more elaborate modeling, a finite element method (FEM) can be employed.

The objective of this work is threefold: Firstly, to model a multilayer structure (a maximum of 6 layers is used herein) with one active piezoelectric element through the electrical impedance. Herein a 1D model and a finite element (FE) model are developed. By combining these with a model of the electrical transceiver circuit it is possible to, given an electrical transmit pulse, simulate the received voltage which will be a function of the reverberating signals in all layers. Hence both the acoustical channel and the electrical channel are modeled simultaneously. This may be important for continuous, long term structural health monitoring applications, such as for the SmartPipe project [9] where it is aimed at installing sensor-belts along subsea pipelines. Given a good correspondence between the model and the measurements, a change in the transducer response can then be related to the piezoelectric parameters as well as changes in the temperature or layer thicknesses. Secondly, in many non-destructive evaluation (NDE) applications it is challenging to separate weak signals from strong overlapping echoes. Herein, a simple contrast enhancement scheme for removing the strong reverberations in steel is presented. This increases the robustness of the proposed wax detection scheme by making the wax echo more readily identifiable. Finally, the model is fitted to measurements using a genetic algorithms inversion scheme. This increases the confidence in both the model and the transducer behavior, and it facilitates the inversion of material parameters and layer thicknesses. When it comes to inversion of material parameters from plane layers, much related work is reported in the literature (see e.g. [2, 10–12]). The conceptual difference with this work is that herein the inversion includes the model of the electro-acoustic coupling and that the inversion is performed on the isolated wax signal. In general the suggested approach can be useful for applications where it is necessary to separate out weak signals from strong reverberations in an intermediate layer. More specifically, if this method should be used for detection and monitoring of wax deposits in gas pipelines, surface roughness, curvature of the pipeline as well as effect of temperature should also be taken into account. These topics are thoroughly treated in [13, 14] and it should be feasible to implement eventual compensation schemes into the method presented herein. It should be noted that the electro-mechanical (E/M) impedance method is another technique which employs the electrical impedance in order to estimate the state of multilayer structures. This can in turn be related to e.g. near-field damages or self-diagnostics [15, 16].

## B.2 Overview of the multi-layered structure

An example of the multi-layered structure is illustrated in Figure B.1 and it is composed of maximum 6 layers. The structure consists of plane layers, starting with a PZ26 [17] circular piezoceramic layer (which is considered passive in this work), a frequency selective, low impedance, isolation layer and a circular active PZ27 [17] piezoelectric layer which is bonded directly onto a rectangular steel with a thin epoxy layer. As the piezoelectric element has a characteristic impedance close to steel, this will cause a good acoustic match between those two layers. An additional layer consisting of paraffin wax is optionally deposited on the steel surface. The thickness of the isolation layer should be  $\lambda_{iso}/4$  where  $\lambda_{iso}$  is the wavelength in the centre of the passband of the transducer. The isolation layer is originally developed for 2-frequency transducers with the objective of minimizing the energy transmission in the backward direction as well as separating the two frequency bands [18, 19]. In [20] it is shown that by using such an isolation layer, the mechanical impedance seen backwards from the active piezoelectric element is lower than the impedance of the material constituting the isolation layer in the expected passband of the transducer. This, together with the good acoustic match towards steel, indicates a high efficiency of the transducer in its pass-band. Hence the isolation layer is an alternative to more traditional high-impedance backing procedures for which the sensitivity of the transducer can be increased. The effect of the isolation layer is investigated in Section B.5.1. Relevant material properties of the multi-layered structure are given in Table B.1.

Table B.1: Material properties and layer thicknesses

	$Z = \rho c$ [MRayl]	$c$ [m/s]	$\eta$	$L$ [mm]	$\nu$	$E$ [GPa]
Passive ceramics	34.6	4523	0.0003	10.1	-	-
Isolation layer	2.9	2600	0.033	0.337 <sup>a</sup>	0.37	4.25
Piezoceramic layer	33.3	4330	0.014	1.0	-	-
Coupling layer	2.9	2600	0.033	0.0055 <sup>a</sup>	0.37	4.25
Steel	46	5900	0.002	14.5	0.29	209
Wax	1.85 <sup>b</sup>	2030 <sup>b</sup>	0.08b	-	-	-

<sup>a</sup> This value is estimated using the genetic algorithm inversion scheme.

<sup>b</sup> This value is estimated from independent measurements

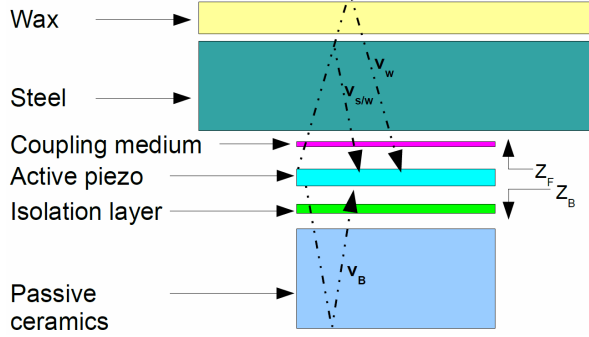


Figure B.1: Outline of the multi-layered transducer structure.  $Z_F$  and  $Z_B$  are the acoustic impedances seen forward and backwards from the active piezoelectric layer respectively.  $v_B$  is the received voltage due to the backward propagating energy. The forward propagating waves are split into the echo from the steel/wax interface,  $v_{s/w}$ , and the reverberations in the wax layer,  $v_w$ . The dashed arrows indicate the acoustic path of the three signals.

## B.3 Theory

### B.3.1 1D modeling of a multi-layered transducer structure and transceiver circuit

When the piezoelectric material equation is assumed to be in one dimensional thickness mode, the relations between the voltage,  $V_1$ , across- and the current,  $I_1$ , into the electrodes of the piezoelectric element, and the pressures and particle velocities at the two surfaces of the piezoelectric element can be represented by the Mason equivalent 3-port circuit in Figure B.2 [21]. The pressures over the acoustic impedances seen forward and backwards ( $Z_F$  and  $Z_B$ ) from the piezoceramic layer are denoted by  $P_1$  and  $P_2$  respectively while the particle velocities at the boundaries of the piezoelectric element is given by  $U_1$  and  $U_2$ . Harmonic variables are assumed, i.e.  $p_1(t) = \text{Re}\{P_1 e^{-j\omega t}\}$ , etc where  $\omega$  is the angular frequency and  $j = \sqrt{-1}$ . Further  $Z_1^M = jZ_0 \tan(k_0 L_0)/2$  and  $Z_2^M = -jZ_0 / \sin(k_0 L_0)$  where  $Z_0 = \rho_0 c_0$  is the characteristic impedance,  $\rho_0$  is the density,  $c_0$  is the speed of sound in the piezoelectric element and  $L_0$  is the thickness of the piezoelectric element. The complex wave number  $k_0 = \omega/c_0 \cdot (1 - j\eta_0/2)$ , incorporates a linear attenuation model using the loss factor,  $\eta_0$ . Consider that there are  $N$  ( $M$ ) additional layers in the backward (forward) direction. Then  $Z_B$  ( $Z_F$ ) can be calculated iteratively using the

formula:

$$Z_{AI,i}(\omega) = Z_i \frac{Z_{AI,i-1} + jZ_i \tan(k_i L_i)}{Z_i + jZ_{AI,i-1} \tan(k_i L_i)}. \quad (\text{B.1})$$

Here  $Z_{AI,i}$ ,  $Z_i$ ,  $k_i$  and  $L_i$  are the spatial dependent acoustic impedance seen into layer  $i$ , the characteristic impedance, wave number and thickness of layer  $i$ . In order to initialize the iteration,  $Z_{AI,0} = Z_{Air} \approx 0$  ( $Z_{AI,0} = Z_L$ ) when calculating  $Z_B$  ( $Z_F$ ). Here  $Z_{Air}$  and  $Z_L$  are the characteristic impedances of air and the load respectively. Hence it is clear that  $Z_B = Z_{AI,N}$  ( $Z_F = Z_{AI,M}$ ).  $M$  and  $N$  can be any positive integer in the general case. The total number of layers thus becomes  $M + N + 1$ . For the specific setup shown in Figure B.1,  $M = 3$  and  $N = 2$  but some simulations also assumes that  $M < 3$  or  $N < 2$  depending on the analysis. The total electrical impedance of the transducer,  $Z_{XD}$ , seen from the electrical ports is calculated using Figure B.2:

$$Z_{XD}(\omega) = (Z_{C_0} || Z_M) / A \quad (\text{B.2})$$

Here  $Z_{C_0} = 1/(j\omega C_0)$  where  $C_0 = \varepsilon/L_0$ .  $\varepsilon$  is the dielectric constant. Further  $A$  is the area of the piezoceramic while  $Z_M$  is the impedance of the components above the transformer referred to the primary side defined as:

$$Z_M(\omega) = (-h^2 C_0 / (j\omega) + Z_2^M + Z_R || Z_L) / (hC_0)^2 \quad (\text{B.3})$$

where  $Z_R = Z_F + Z_1^M$  and  $Z_L = Z_B + Z_1^M$  and  $h$  is the piezoelectric constant. Note that the operator  $||$  returns the resulting impedance from two impedances coupled in parallel, i.e.  $Z_a || Z_b = Z_a Z_b / (Z_a + Z_b)$ .

The transceiver circuit applied in this work is illustrated in Figure B.3 where  $Z_{Scope}$ ,  $Z_g$  and  $Z_{Cables}$  are the electrical impedances of the oscilloscope, the signal generator and the cables respectively, and  $V_g$  refers to the voltage source. The impedance transfer function,  $H_{M,N}$ , which relates the transmitted electrical pulse to the received voltage over the oscilloscope for a  $M + N + 1$  layer model is defined by

$$H_{M,N}(\mathbf{p}; \omega) = \left[ \frac{Z_{par}(\mathbf{p}; \omega)}{Z_{par}(\mathbf{p}; \omega) + Z_g(\omega)} \right]_{M,N} \quad (\text{B.4})$$

where

$$Z_{par}(\mathbf{p}; \omega) = Z_{Cables} || Z_{Scope} || Z_{XD}. \quad (\text{B.5})$$

Here  $\mathbf{p}$  is the model-parameters to be estimated, e.g. layer thickness, loss factor etc. In general  $\mathbf{p}$  is a vector as multiple parameters can be estimated simultaneously. Note that  $H_{M,N}$  completely determines the received voltage due to

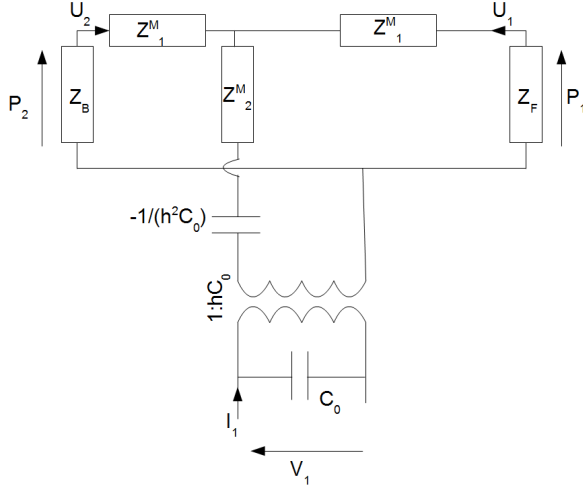


Figure B.2: Mason equivalent of piezoelectric element.

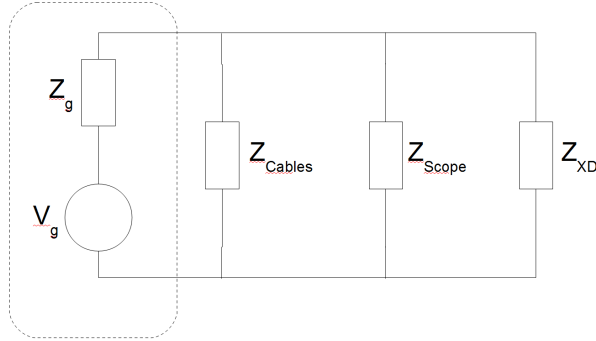


Figure B.3: Electrical network of transceiver circuit.

internal ringing in all the layers in the structure. Given a transmitted generator voltage  $V_g(\omega)$  the windowed received waveform is defined in the frequency domain as

$$V_{M,N}(\mathbf{p}; \omega) = [H_{M,N}(\mathbf{p}; \omega) \cdot V_g(\omega)] * W(\omega) . \quad (\text{B.6})$$

Here  $W(\omega)$  is the Fourier transform of a Tukey window [22] used in order to separate out the echoes to be analyzed and  $*$  is the convolution operator. This is preferred over a rectangular window because of lower side-lobes. The received signal in time domain can now be found through the inverse Fourier transform:

$$\bar{v}_{M,N}(\mathbf{p}; t) = \int e^{j\omega t} V_{M,N}(\mathbf{p}; \omega) d\omega / 2\pi . \quad (\text{B.7})$$

Note that the measured signal and the simulated time-domain signal are denoted without and with a bar, respectively.

### B.3.2 FE modeling of a multi-layered transducer structure

An axisymmetric FE model has been developed in Comsol 3.5a (Comsol AB, Stockholm, Sweden) for validating the 1D model as well as comparing with measurements. The geometry of the FE model is shown in Figure B.4. The left boundaries represent the axial symmetric axis. This is a multiphysics problem where Comsol's *Piezo Axial Symmetry* application mode and *Axial Symmetry Stress-Strain* application mode can be combined. The *Piezo Axial Symmetry* application mode has three material models for which all are employed in this model. The active element uses the piezoelectric material model governed by the stress-charge equations which express the relation between the stress, strain, electric field, and electric displacement field:

$$\begin{aligned}\mathbf{T} &= [c_E] \mathbf{S} - [e^T] \mathbf{E} \\ \mathbf{D} &= [e] \mathbf{S} + [\varepsilon_S] \mathbf{E}\end{aligned}\tag{B.8}$$

In the general 3D case,  $\mathbf{T}$  is the 6x1 stress vector,  $\mathbf{S}$  is the 6x1 strain vector,  $\mathbf{E}$  is the 3x1 electric field vector and  $\mathbf{D}$  is the 3x1 electric displacement field vector.  $c_E$ ,  $e$  and  $\varepsilon_s$  are the 6x6 piezoelectric elasticity matrix, the 3x6 coupling matrix and the 3x3 permittivity matrix of the material respectively. The subscript  $E$  indicates a zero, or constant, electric field; the subscript  $S$  indicates a zero, or constant, strain field; and the superscript  $T$  stands for transposition of the matrix. The isolation layer and coupling layer use the decoupled isotropic material model. The passive ceramic employs the anisotropic material model. Both the isotropic and anisotropic model is governed by Hooke's law,  $\mathbf{T} = [c] \mathbf{S}$ , with the difference that for isotropic materials, the 6x6 elasticity matrix  $[c]$  is determined by two constants only, namely the Young's modulus and the Poisson ratio. The mechanical damping is given as a loss factor,  $\eta$ . The steel uses an isotropic material model together with the axial symmetry stress-strain application mode which also is governed by Hooke's law. The reason for introducing this application mode is to incorporate a cylindrical perfectly matched layer (PML) absorbing in all directions for the steel. PMLs are not available in the *Piezo Axial Symmetry* application mode. The width of the PML is larger than the longest simulated wavelength in steel, indicating that sufficient absorption is attained [23]. For the interior boundaries in the transducer and steel, continuity of displacements and stresses are necessary. The exterior boundaries are free as the measurement is performed in air.

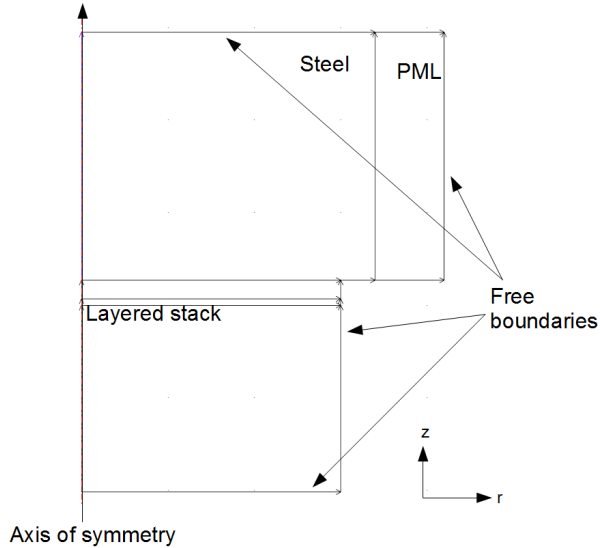


Figure B.4: Geometry of the FE model.

The maximum mesh size,  $h_{max}$ , is determined by  $h_{max} \leq \lambda_{min}/6$ .  $\lambda_{min}$  is in general determined by the maximum frequency as well as the lowest wave speed in the material. For solids, this is given by the shear wave velocity. As a 2<sup>nd</sup> order Lagrange polynomial is used as basis functions, this implies a minimum of 12 nodes/ $\lambda_{min}$ . A convergence study where the element size is decreased from larger to smaller mesh sizes has been performed to ensure the reliability of the results. Unstructured and structured meshes have also been compared, but only negligible differences in the results are observed. An unstructured mesh is employed in the simulation.

In order to compare the FE model with the 1D model, the electrical impedance,  $Z_{xd}$ , seen from the electrodes of the active piezoelectric element must be calculated. (Note that the subscript of the electrical impedance of the FE model is in lowercase letters.) Since the FE model can't be represented with a lumped circuit model,  $Z_{xd}$  is found differently: The FE model is solved by applying a harmonic voltage,  $V_1$ , over the electrodes. This is performed for a whole range of frequencies, and for each frequency a resulting current density,  $\mathbf{J}$ , is developed. The total current is then calculated by performing boundary integration over the electrode as

$$I_1 = \int_0^{r_{max}} \mathbf{J} \cdot \mathbf{n} \cdot 2\pi r dr . \quad (\text{B.9})$$

Here  $\mathbf{n}$  is the normal unit vector on the boundary. Finally  $Z_{xd}$  can be calculated as

$$Z_{xd} = V_1/I_1 \quad (\text{B.10})$$

Now  $Z_{xd}$  can replace  $Z_{XD}$  in Eq. (B.5), making it possible to compare the two models.

### B.3.3 Isolation of wax signal

When the piezoelectric layer is excited with an electric pulse, it will transmit energy both in the forward and backward direction. Referring to Figure B.1 it is clear that the forward propagating wave eventually will hit the steel/wax interface where it is partially reflected and partially transmitted. The pulse transmitted into the wax causes a reverberating wave bouncing back and forth between the steel/wax- and wax/air-interface. It is assumed that a Tukey-window has selected only the first echo from the steel/wax interface together with the resulting wax reverberations, and the total received voltage can hence be split in the time domain as

$$\begin{aligned} v_{3,2}(t) &= v_F(t) + v_B(t) \\ &\approx v_F(t) = v_{s/w}(t) + v_w(t). \end{aligned} \quad (\text{B.11})$$

Here  $v_F$  and  $v_B$  are the received voltages due to the forward and backward propagating signals respectively while  $v_{s/w}$  and  $v_w$  are the received voltages due to the 1<sup>st</sup> reflected wave at the steel/wax interface and due to the reverberating wave in the wax respectively. The approximation in Eq. (B.11) is introduced because the amount of signal power transmitted backwards is small compared to what is transmitted in the forward direction and hence assumed negligible. This is discussed in more detail in Section B.5.1.

Now assume a reference signal,  $v_{2,2}$ , is measured with only air beneath steel. The received signal will then mainly consist of the echo from the steel/air interface; again neglecting  $v_B$  (this will simplify the following analysis.) Denote this by  $v_{s/a}$ . Hence the reference signal is approximated as  $v_{2,2}(t) \approx v_{s/a}(t)$ . Compared to  $v_{s/w}$ ,  $v_{s/a}$  will have a larger amplitude due to a higher absolute value of the reflection coefficient. A time-shift may also occur due to temperature variations and experiments have shown that it is crucial to do a time-shift correction; even small temperature variations ( $< 1^\circ\text{C}$ ) will distort the result if not compensated for. The first step is to correct for the amplitude-difference:

$$\hat{v}_{s/w}(t - \tau) = \frac{v_{2,2}(t) \cdot \|v_{2,3}\|_\infty}{\|v_{2,2}\|_\infty} \approx v_{2,2}(t) \cdot |R_{s/w}| \quad (\text{B.12})$$

where  $\|\cdot\|_\infty$  denotes the peak,  $\hat{v}_{s/w}(t - \tau)$  is the estimated signal from the steel/deposit interface with the true time-shift  $\tau$  and  $R_{s/w}$  is the normal incident reflection coefficient between the steel/deposit-interface. To estimate  $\tau$ , a time-delay estimation scheme, e.g. correlation, between the estimated- and measured signal is performed:

$$\begin{aligned}\hat{\tau} &= \arg \max_k E\{\hat{v}_{s/w}(t - \tau)v_{2,3}(t - k)\} \\ &\approx \arg \max_k E\{\hat{v}_{s/w}(t - \tau)v_{s/w}(t - k)\}\end{aligned}\tag{B.13}$$

The main assumption in the approximation of Eq. (B.13) is that  $\|v_w\|_\infty \ll \|v_{s/w}\|_\infty$ . This is apparent when considering that the voltage ratios are bounded upwards by the ratios of the transmission/reflection coefficients governing the amplitude of the echoes in steel when disregarding attenuation:  $\|v_{s/w}\|_\infty$  is governed by  $|rR_{s/w}|$  where  $r$  is a constant and  $R_{s/w}$  is the normal incident reflection coefficient between the steel/deposit interface.  $\|v_w\|_\infty$  is on the other hand bounded upwards by  $|rT_{s/w}R_{w/a}T_{w/s}|$  where  $T_{s/w}$  is the transmission coefficient between the steel/wax interface and  $R_{w/a} = -1$  is the reflection coefficient between the wax/air. Hence it is seen that:

$$\frac{\|v_w\|_\infty}{\|v_{s/w}\|_\infty} \leq \left| \frac{T_{s/w}R_{w/a}T_{w/s}}{R_{s/w}} \right| = \frac{4Z_sZ_w}{Z_s^2 - Z_w^2}\tag{B.14}$$

with equality for zero absorption. Inserting a plausible value of  $Z_w = 1.8\text{MRayl}$  gives  $\|v_w\|_\infty/\|v_{s/w}\|_\infty \leq -16\text{dB}$ . The estimate of the signal from the steel/deposit interface now becomes:

$$\hat{v}_{s/w}(t) \approx \hat{v}_{s/w}(t - \tau + \hat{\tau})\tag{B.15}$$

and  $v_w$  can further be estimated from the measured received signal,  $v_r$ , as

$$\hat{v}_w(t) = v_{3,2}(t) - \hat{v}_{s/w}(t) \approx v_w(t).\tag{B.16}$$

It should be noted that  $v_B$  will be equal for  $v_{2,2}$  and  $v_{3,2}$ . Hence the subtraction in (B.16) will also remove  $v_B$  (which is already assumed negligible) except for a scaling error corresponding to the ratio of the reflection coefficients given in (B.12). Since  $R_{s/w}/R_{s/a} = R_{s/w} \approx 0.95$ , roughly 95% of  $v_B$  is removed through this scheme.

### B.3.4 Inversion procedure

In any inversion scheme, the objective is to estimate some true parameters,  $\mathbf{p}$ , through a comparison of a measured and a predicted data set. The best estimate of  $\mathbf{p}$  is the one that minimizes an objective function,  $\varphi$ , which typically

represents a variant of the squared error sum between the observed and modeled data. Another common name for  $\varphi$  is the error function. In the current work, a hybrid approach using genetic algorithms combined with a quasi-Newton search is employed for the data fitting. Genetic algorithms is a global nonlinear optimization scheme related to genetic evolution and driven by stochastic means. It has successfully been employed in e.g. seismic applications [24, 25], and it reduces computation compared to traditional Monte Carlo techniques. The genetic algorithm is implemented employing the Genetic Algorithms Toolbox in Matlab (Mathworks, Massachusetts, USA). To improve the value of the search, a local quasi-Newton minimization scheme which uses the final point from the genetic algorithm as its initial point is employed.

### B.3.4.1 Fitting of Reference Signal

The reference signal is modeled using Eq. (B.7) and assuming that the thickness of the wax layer is zero.  $\varphi$  is assumed to be the normalized root mean square error between the simulated and measured signal:

$$\varphi(\mathbf{p}) = \|\bar{v}_{2,2}(\mathbf{p}; t) - v_{2,2}(t)\| / \|v_{2,2}(t)\| \quad (\text{B.17})$$

where  $\|\cdot\|$  denotes the L2 norm. As most of the model parameters are known with the desired certainty, the number of unknowns in the optimization is limited to two; the thickness of the isolation- and coupling layer denoted  $L_{iso}$  and  $L_c$ . Hence  $\mathbf{p} = [L_{iso}; L_c]$ . The reason for estimating only these values is that  $L_{iso}$  and  $L_c$  are associated with the largest uncertainties in the reference structure (i.e. the multi-layered structure without any layer beneath steel) due to the manufacturing procedure. In order to limit the search space, realistic bounds are given. The formulation of the inversion problem becomes:

$$\hat{\mathbf{p}} = \arg \min_{\mathbf{p}} \varphi(\mathbf{p}) \quad (\text{B.18})$$

Here  $\hat{\mathbf{p}}$  is the estimated value of  $\mathbf{p}$ .

### B.3.4.2 Estimation of acoustical parameters from wax

The reflections from the wax/load interface are very weak compared to the strong reverberations in the steel. To increase the sensitivity of the inversion, the wax signal is isolated prior to the optimization. Hence the two models  $\bar{v}_{2,2}(t)$  and  $\bar{v}_{3,2}(\mathbf{p}_w; \mathbf{t})$  are simulated. Note that  $\bar{v}_{2,2}(t)$  have no dependence on the vector  $\mathbf{p}$  which in this case consists of a combination of any of the wax-parameters to be estimated, for example  $c_w$ ,  $\rho_w$ ,  $L_w$  or  $\eta_w$  denoting the sound

speed, density, thickness and loss factor of the wax respectively. By subtracting the two modeled waveforms, the signal from the wax/air interface is obtained:

$$\bar{v}_w(\mathbf{p}; t) = \bar{v}_{3,2}(\mathbf{p}; t) - \bar{v}_{2,2}(t) \cdot R_{s/w}/R_{s/a} \quad (\text{B.19})$$

By combining Eq. (B.16) and Eq. (B.19) with the selected optimization criterion, the objective function to be minimized becomes

$$\varphi_w(\mathbf{p}) = \|\bar{v}_w(\mathbf{p}; t) - \hat{v}_w(t)\|/\|\hat{v}_w(t)\| . \quad (\text{B.20})$$

When performing inversion it is important to do a sensitivity analysis of the different parameters. The sensitivity of a parameter  $p_i \in \mathbf{p}$  is herein defined as

$$S_{\bar{v}_w, p_i} = \frac{1}{\|\bar{v}_w\|} \left\| \frac{p_i \delta \bar{v}_w}{\delta p_i} \right\| \quad (\text{B.21})$$

i.e. it is a normalized measure of how much the model varies when performing a perturbation of the parameter. It is not in the scope of this work to do a detailed sensitivity analysis, but it is worth mentioning the main principle: If the sensitivity is small, a small error in measuring  $v_w$  causes a large error in estimating  $p_i$  and vice versa [2]. Hence, when solving the inverse problem, the sensitivity is a very important parameter; the higher the sensitivity, the better. If two parameters have the same influence on the model, linear dependency between the parameters makes the inverse problem impossible. An example of two nearly linearly dependent parameters is  $c_w$  and  $L_w$ ; when perturbing these, the main change in the model is a change in phase through the one-way travel time  $\tau_w = L_w/c_w$ . It is clear that separate changes in  $c_w$  or  $L_w$  can lead to the same change in phase. Hence it is not possible to determine which of  $c_w$  or  $L_w$  that has caused the phase change. It is still theoretically possible to estimate both  $c_w$  and  $L_w$  simultaneously because  $c_w$  also determines the wax impedance  $Z_w$  but then  $\rho_w$  must be assumed known. This is discussed in more detail in Section B.5.4.

## B.4 Experimental procedure

The experimental setup is represented as a lumped circuit as shown in Figure B.3. The electrical transmit pulse is generated using a WW2571 Tabor signal generator (Tabor Electronics Ltd., Tel Hanan, Israel) which is directly connected to the active piezoelectric element. The received signal is stacked and recorded by a Lecroy WaveSurfer 42Xs oscilloscope (LeCroy, Geneva, Switzerland) and transferred to a PC for further investigation. The wax [26] layer is

obtained by heating the leveled low carbon steel (the transducer structure is now below the steel plate) with a certain amount of wax already placed inside a mold on the steel surface. When the temperature of the steel exceeds the melting point of 57-59°C, the paraffin wax melts directly on the steel. When the heating procedure stops, the wax will solidify as a plane layer. To avoid vaporization of the wax, the steel is then cooled down in a water bath. The mold had a well defined circular geometry. An estimation of  $L_w$  was enabled by depositing a known mass of wax over a known area. The material parameters  $\eta_w$ ,  $c_w$  and  $\rho_w$ , were determined from independent measurements. The estimated values of the material parameters are found in Table B.1.

## B.5 Results and discussion

### B.5.1 Effect of isolation layer

As the passive ceramics has negligible loss, the acoustic energy transmitted backwards will reverberate back and forth in the layer for a long time and affect the received pulse response. Considering an excited signal transmitted simultaneously in both directions, the expected transit time for the pulse propagating backwards to the ceramic/air interface and back to the piezoelectric element, where it is received as  $v_B$ , is  $4.7\mu s$ . The expected transit time for the pulse propagating forwards to the steel/air interface and back to the piezoelectric element, where it is received as  $v_F$ , is  $4.9\mu s$ . As one period of the pulse lasts for about  $0.5\mu s$ , these signals will overlap. In order to simulate the influence of  $v_B$  on the complete signal  $v_{3,2}$ , two scenarios are simulated with the 1D model: a)  $v_F$  is modeled in the same manner as  $v_{2,2}$  (disregarding the wax layer which is uninteresting in this analysis), but with one main difference: The passive ceramic is assumed to be the load in the backward direction. Hence no signal from the ceramic/air interface is received and  $v_{2,1} = v_F$ . b)  $v_B$  is also modeled in the same manner as  $v_{2,2}$  except one important difference: It is assumed that the steel is the load, i.e. the steel is semi-infinite. Then the strong signal from the steel/air interface is avoided, and  $v_{1,2} = v_B$ . (It is important to note that the subscripts denote the number of layers forwards and backwards seen from the active element).

The signal envelopes of the received voltages from these scenarios are compared in Figure B.5. A one cycle sine pulse with  $f_c = 2\text{MHz}$  is given as input voltage. According to this result, the amplitude of the first arrival of  $v_B$  is 28dB below that of  $v_F$ . Hence,  $v_B$  has little influence on the total received signal indicating that the isolation layer works as intended and that the approximation in Eq. (B.11) is sound.

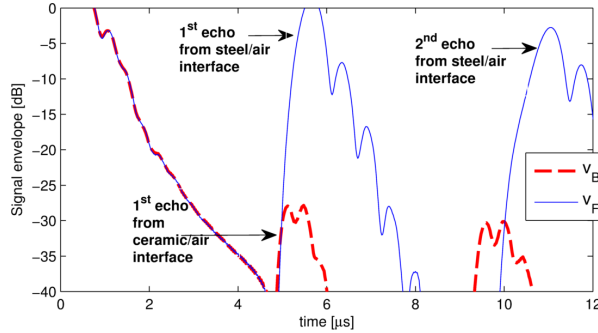


Figure B.5: Simulations of signal envelopes of  $v_B$  versus of  $v_F$ .

### B.5.2 Fitting of reference signal

A reference signal is recorded using a 10 volt peak-to-peak 1 cycle sine pulse as input from the signal generator. Then the inversion scheme expressed with Eq. (B.18) is executed to obtain the optimal fit between the 1D model and the measurement. Most of the fixed parameters for the 1D model are found in Table B.1, except the piezoelectric parameters which are  $h = 1.98 \cdot 10^9 \text{V/m}$  and the relative permittivity  $\epsilon_r = 914$  [17]. The result from the inversion is presented in Figure B.6. It can be seen that an excellent agreement is achieved between the simulated and measured data suggesting that the 1D model is valid for the given multi-layered structure.

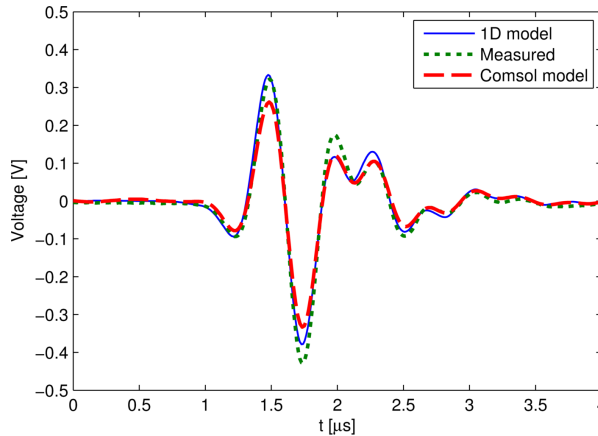


Figure B.6: 1D-modeled and COMSOL-modeled vs. measured reference signal,  $v_{2,2}$ .

Based on the estimated layer thicknesses of the coupling- and isolation layer, the complete axisymmetric Comsol model has been developed. The isolation layer and the coupling layer are made from a two-component epoxy (SvaPox 110/Harter TL, Svas Kjemi AS, Fettsund, Norway). For isotropic materials such as steel and epoxy, the input structural material parameters are density, Poisson's ratio,  $\nu$ , and Young's modulus,  $E$ . As the true values of  $\nu$  and  $E$  are unknown, they are estimated in the following way: The p-wave velocity and density of the materials are measured.  $\nu$  and  $E$  are then chosen so that they correspond to tabulated data found in [27] of similar materials with comparable densities and p-wave velocities.  $Z_{xd}$  is found using Eq (B.10) and then replacing  $Z_{XD}$  in Eq. (B.5). The resulting received voltage, given the same transmit-pulse as for the 1D model, is also shown in Figure B.6. The agreement with both the measurement and the 1D model is excellent when it comes to pulse shape, a fact that further increases the confidence in that a plane wave solution is sufficient for the given structure. When looking at the signal amplitude though, the signal modeled with the FE model is down about 10% compared to the 1D-modeled signal and the measured signal. There are some probable explanations for this: Firstly, it is only the 1D model which is optimized with respect to the measurement. If the FE model had been optimized, slightly different parameters favoring the FE model could have been obtained instead. Secondly, the 1D model incorporates fewer parameters leading to less uncertainty. For example, there is less uncertainty related to the longitudinal speed of sound which is input to the 1D model, than to the combination of  $E$ ,  $\nu$  and  $\rho$  which determines the sound speed in the FE model. The tolerances for the piezoelectric materials are  $\pm 5\%$  for the electromechanical properties and  $\pm 2.5\%$  for the mechanical properties [28]. As the FE model employs more of these parameters, more uncertainty are also introduced into the model.

In Figure B.7 the error function  $\varphi(L_c, L_{iso})$  which is characterized by a valley along the  $L_{iso}$ -axis is presented, but it still has a well defined minimum. Since the gradient of  $\varphi$  increases more rapidly along the  $L_c$ -axis, it is clear that the model is more sensitive to  $L_c$ . For  $L_{iso}$  the target thickness was  $\lambda_{iso}/4$  at 2MHz, corresponding to  $325\mu\text{m}$  when  $c = 2600\text{m/s}$ . The inversion gives  $337\mu\text{m}$  which is a deviation of  $12\mu\text{m}$ . When bonding a plane piezoelectric element onto a plane steel sample with epoxy, a thickness of a few  $\mu\text{m}$  is expected. Herein,  $L_c$  is found to be  $5.5\mu\text{m}$ . So even if the true values of  $L_c$  or  $L_{iso}$  are unknown, the estimates seem reasonable.

A typical result from the COMSOL simulation, showing the real part of the z-component of the stress in steel, is illustrated for  $f = 2\text{MHz}$  in Figure B.8. By studying the wave fronts, it can be observed that they are not completely

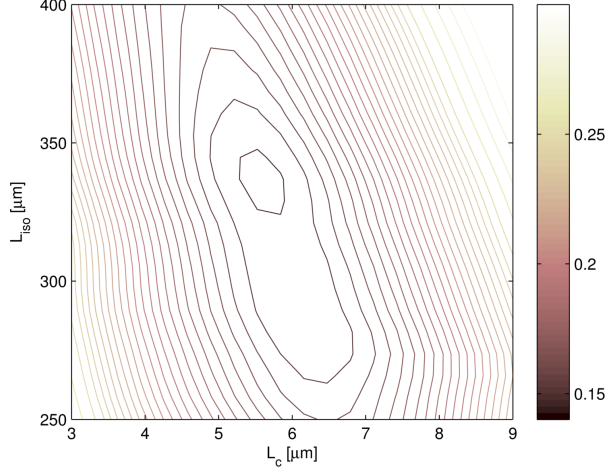


Figure B.7:  $\varphi$  as a function of  $L_c$  and  $L_{iso}$  with a minimum at  $(5.5\mu\text{m}, 337\mu\text{m})$ .

plane. The reason for this is that for a harmonic solution at one frequency, a mode pattern will occur on the excited piezoelectric element. When several of these frequencies are combined into a broadband pulse, the mode pattern will vary for each frequency causing destructive interference and the summation over the whole frequency range will produce an approximately plane wave with no such mode pattern. Different mode patterns of piezoelectric elements are analyzed in for example [29].

Due to a significantly reduced computational complexity when using the 1D model compared to the FE model and the good correspondence between the 1D model and measurement, the 1D model is employed in the rest of this paper.

### **B.5.3 Isolation of wax signal**

If the wax layer is thin compared to the wavelength of the transmitted pulse, it is not possible to resolve the individual reflections from the wax. When the echoes interfere, the individual flanks of the reflections will be masked. In order to test the contrast enhancement scheme proposed for resolving the problem, a reference measurement,  $v_{2,2}$ , and a measurement with wax,  $v_{3,2}$ , are recorded using a 32 volt peak-to-peak 1 cycle sine pulse as input. Then the procedure described in Eqs. (B.12)-(B.16) is executed. An example result with a 1.1mm wax layer is seen in Figure B.9. Here  $v_{2,2}$  and  $v_{3,2}$  is plotted and it can be observed that the weak reflections from the wax is difficult to distinguish relative to the strong signal from the steel/wax interface. The ellipse illustrates

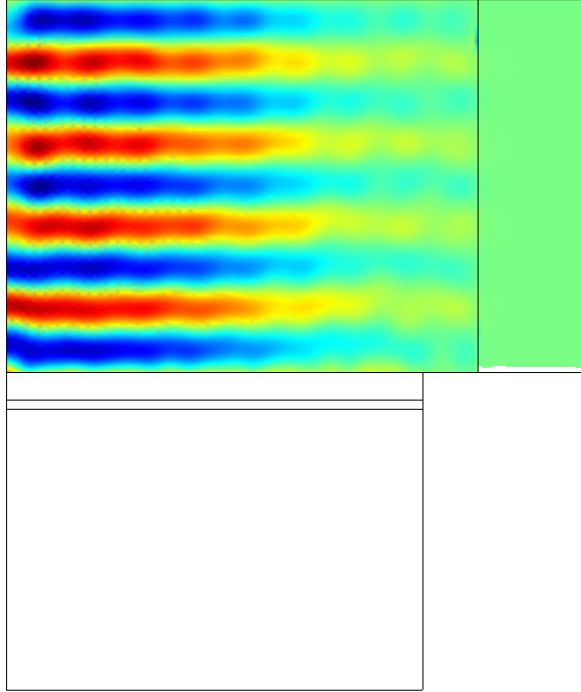


Figure B.8: Continuous wave simulation. Real part of z-component of stress in steel at  $f = 2\text{MHz}$ .

the time interval for where deviation is expected. Indeed, some differences are observable, but due to the overlap between the internal ringing and the wax-signal causing interference between the signals, it is challenging to draw any conclusions regarding the wax parameters directly.

Figure B.10 illustrate that by performing the isolation procedure, the strong reverberations in steel are suppressed with 40dB. It can be observed that  $\hat{v}_w$  is 21dB below the peak of  $v_{3,2}$  and that  $\hat{v}_w$  is clearly below the internal ringing of the transducer. If for example Figure B.9 and Figure B.10 a) are investigated more carefully, the main positive peaks occur at  $1.05\mu\text{s}$  and  $2.15\mu\text{s}$  respectively resulting in an estimated layer thickness of  $\approx 1.1\text{mm}$  given  $c_w = 2030\text{m/s}$ . This is a straightforward estimate yielding fine results given a good estimate of the sound speed.

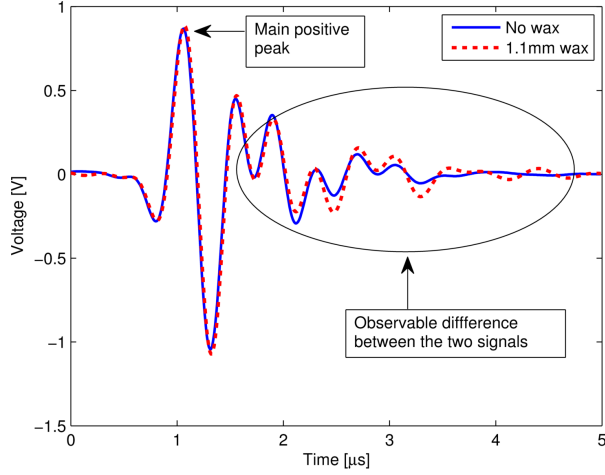


Figure B.9:  $v_{2,2}$  and  $v_{3,2}$  where the difference in amplitude has been corrected.

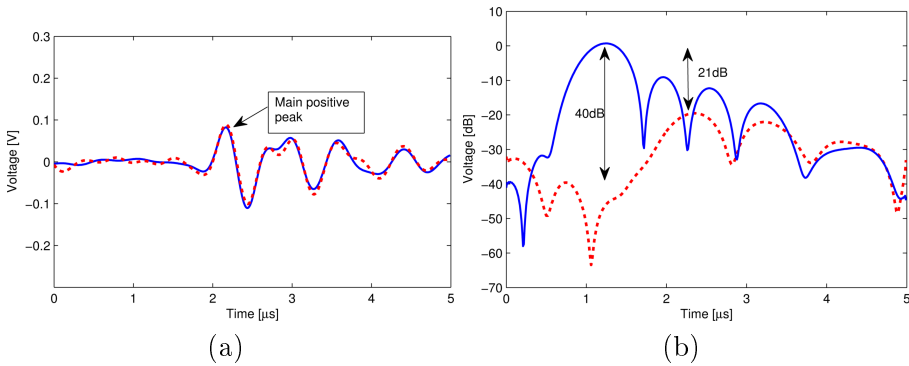


Figure B.10: a) Modeled ( $\bar{v}_w$ , solid) versus processed measured data ( $\hat{v}_w$ , dotted) of the isolated wax signal. b) Signal envelope of  $v_r$  (solid) and  $\hat{v}_w$  (dotted).

### B.5.4 Estimation of parameters from wax layer

By fitting the model to the measurements through the inversion scheme two main achievements can be made: Firstly, increased confidence in both the model and the contrast enhancement scheme can be attained. Finally, material parameters as well as layer thickness can be estimated.

When selecting parameters to optimize, it is of importance to avoid ill-conditioned problems. Let's denote the wax parameters  $c_w$ ,  $\rho_w$  and  $L_w$  as the

primary parameters. If no a priori information of the deposit layer is available, it is assumed that a wave experiences a combination of three factors when reverberating in the layer: Firstly, the travel-time  $\tau_w = L_w/c_w$ . Secondly, the acoustic impedance,  $Z_w = \rho_w c_w$ . Finally, the frequency dependent attenuation, here modeled through  $\eta_w$ . It can readily be observed that it is not possible to invert both  $c_w$ ,  $L_w$  and  $\rho_w$  correctly simultaneously as it has an infinite number of solutions (combining  $\tau_w$  and  $Z_w$  end up in two equations with the three unknowns  $c_w$ ,  $L_w$  and  $\rho_w$ ). However, if one of the primary parameters is known in advance, the other two may be estimated based on the relations  $Z_w = \rho_w c_w$  and  $\tau_w = L_w/c_w$ .

In the general case  $\mathbf{p} = [\tau_w; Z_w; \eta_w]$ . To investigate the feasibility of inverting these, consider the sensitivity defined in Eq. (B.21). When perturbing  $\tau_w$ , the most prominent effect is a phase-shift. Two similar signals with different phases will have a large deviation in the mean square sense; hence the sensitivity with respect to  $\tau_w$  is large. Knowing one of the parameters  $c_w$  or  $L_w$ , it is thus feasible to invert the other.  $Z_w$  will only alter the amplitude according to Eq (B.14), while  $\eta_w$  in addition changes the frequency spectrum causing a pulse distortion in the time domain. The model is in general much less sensitive to  $Z_w$  and  $\eta_w$ . As an example, assume  $\tau_w = 0.7\mu\text{s}$ ,  $Z_w = 1.8\text{MRayl}$  and  $\eta_w = 0.05$ . Perturbing the parameters with 1%, gives (using Eq. (B.21))  $S_{\bar{v}_w, \tau_w} = 20.1$ ,  $S_{\bar{v}_w, Z_w} = 0.8$  and  $S_{\bar{v}_w, \eta_w} = 0.5$  and it is observed that the sensitivity with respect to  $\tau_w$  clearly is the largest.

In Figure B.10 b) a typical result from the inversion is presented illustrating that the modeled signal match very well to the contrast enhanced measured signal. Now the percentual deviation  $\sigma_p = (\hat{p}/p - 1) \cdot 100\%$  where  $\hat{p}$  is the inverted and  $p$  the 'true' parameter is introduced and plotted as a function of the true layer thickness. This is presented for the 3-parameter inversion in Figure B.11 for 5 different values of  $L_w$  ranging from 0.8 to 1.5mm. It can be seen that the deviation of  $\tau_w$ ,  $Z_w$  and  $\eta_w$  is roughly within  $\pm 2\%$ ,  $\pm 9\%$  and  $\pm 4\%$  respectively.  $\sigma_\tau$  is in the same order of magnitude as the uncertainty of  $L_w$ . Hence, the accuracy of predicting  $\tau_w$  is probably higher then what is indicated here. It is a contradiction that the deviation is larger for  $Z_w$  than for  $\eta_w$  even though the sensitivity is larger for  $Z_w$ . One possible explanation is as follows: The contrast enhancement scheme tries to isolate the wax signal. The error introduced by the contrast enhancement scheme is larger in the beginning of the wax signal where it strongly overlaps with the echo from the steel/wax interface. It also seems that when estimating  $Z_w$ , the inversion scheme emphasize the beginning of the wax signal where the amplitude (and measurement error) is largest, while for  $\eta_w$  it seems that the latter parts of the signal is equally important

because then the attenuation has had more effect on the waveform. An eventual measurement error introduced by the contrast enhancement scheme thus has a greater impact on the inversion of  $Z_w$  than  $\eta_w$  and this is not taken into account in the sensitivity analysis.

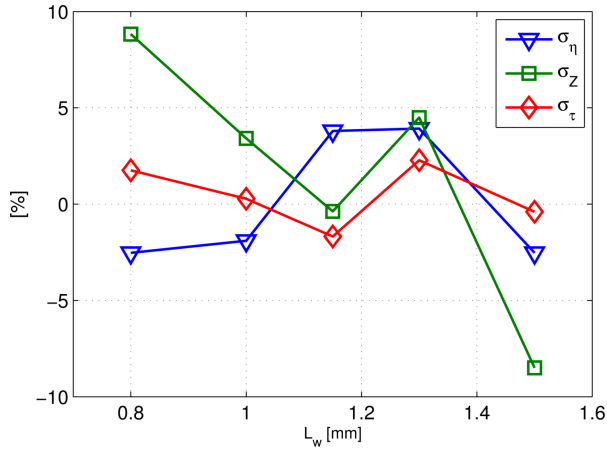


Figure B.11: Percentual deviation from the true value of the three parameters  $\eta_w$ ,  $c_w$  and  $L_w$ .

## B.6 Conclusions

In the current work a multilayer transducer structure has been investigated with the aim of modeling the transducer behavior and detecting weak signals from paraffin wax through steel and estimating material parameters. A 1D-model and a FE model of the structure have been developed and compared with measurements. A contrast enhancement scheme which isolates the weak signal is presented, and it is combined with the 1D model in order to invert material parameters from the wax. The results have shown that an excellent agreement is found between the measured and modeled waveforms. For the inversion, up to 3 parameters (attenuation, impedance and travel time) can be found simultaneously from the wax layer, and it is found that the inverted parameters correspond well to the 'true' parameters. Given one of the three parameters, density, sound speed or thickness, the other two can then be estimated in addition to the attenuation.



# References

- [1] R. Raisutis, R. Kazys, and L. Mazeika, "Ultrasonic thickness measurement of multilayered aluminum foam precursor material," *Instrumentation and Measurement, IEEE Transactions on*, vol. 57, no. 12, pp. 2846–2855, 2008.
- [2] V. K. Kinra and C. Zhu, "Ultrasonic evaluation of thin (sub-wavelength) coatings," *The Journal of the Acoustical Society of America*, vol. 93, no. 5, pp. 2454–2467, 1993.
- [3] G. Gunarathne and K. Christidis, "Material characterization in situ using ultrasound measurements," *Instrumentation and Measurement, IEEE Transactions on*, vol. 51, pp. 368–373, Apr. 2002.
- [4] C. E. Woon and L. D. Mitchell, "Ultrasonic instrumentation for on-line monitoring of solid deposition in pipes," in *Proceedings of the SPE Production Operations Symposium*, 1997.
- [5] W. P. Mason, *Electromechanical Transducers and Wave filters*. D. Van Nostrand Company, Inc, 1948.
- [6] M. Redwood, "Transient performance of a piezoelectric transducer," *The Journal of the Acoustical Society of America*, vol. 33, no. 4, pp. 527–536, 1961.
- [7] R. Krimholtz, D. Leedom, and G. Matthaei, "New equivalent circuits for elementary piezoelectric ceramic transducers," *Electronics Letters*, vol. 6, no. 13, pp. 398–399, 1970.
- [8] A. Lopez-Sanchez and L. Schmerr, "Determination of an ultrasonic transducer's sensitivity and impedance in a pulse-echo setup," *Ultrasonics, Ferroelectrics and Frequency Control, IEEE Transactions on*, vol. 53, pp. 2101–2112, november 2006.

- 
- [9] SmartPipe project. [Online]. Available: <http://www.sintef.no/Projectweb/SmartPipe/>.
- [10] T. E. G. Alvarez-Arenas, "Simultaneous determination of the ultrasound velocity and the thickness of solid plates from the analysis of thickness resonances using air-coupled ultrasound," *Ultrasonics*, vol. 50, no. 2, pp. 104 – 109, 2010.
- [11] V. K. Kinra and V. R. Iyer, "Ultrasonic measurement of the thickness, phase velocity, density or attenuation of a thin-viscoelastic plate. part ii: the inverse problem," *Ultrasonics*, vol. 33, no. 2, pp. 111 – 122, 1995.
- [12] C. L. Yapura, V. K. Kinra, and K. Maslov, "Measurement of six acoustical properties of a three-layered medium using resonant frequencies," *The Journal of the Acoustical Society of America*, vol. 115, no. 1, pp. 57–65, 2004.
- [13] K. Christidis, *Characterization and monitoring of mineral deposits in down-hole petroleum pipelines*. Phd, The Robert Gordon Univ, Aberdeen, U.K, 2000.
- [14] M. Y. Qureshi, *Development of techniques for detection and dissolution enhancement of mineral deposits in petroleum pipelines using ultrasound*. Phd, The Robert Gordon Univ, Aberdeen, U.K, 2002.
- [15] V. Giurgiutiu, A. Zagrai, and J. Bao, "Embedded active sensors for in-situ structural health monitoring of thin-wall structures," *Journal of Pressure Vessel Technology*, vol. 124, no. 3, pp. 293–302, 2002.
- [16] V. Giurgiutiu and A. N. Zagrai, "Embedded self-sensing piezoelectric active sensors for on-line structural identification," *Journal of Vibration and Acoustics*, vol. 124, no. 1, pp. 116–125, 2002.
- [17] "Ferroperm material datasheet." [Online]. Available: [www.ferroperm-piezo.com/](http://www.ferroperm-piezo.com/).
- [18] T. Azuma, S.-I. Umemura, and H. Furuhashi, "Dual frequency array transducer for ultrasonic-enhanced transcranial thrombolysis," in *Proceedings of the IEEE International Ultrasonics Symposium*, pp. 680–683, 2003.
- [19] T. Azuma, S.-I. Umemura, and H. Furuhashi, "Prototype dual frequency bilaminar array transducer capable of therapeutic exposure at 500 kHz and Doppler monitoring at 2 MHz," in *Proceedings of the IEEE International Ultrasonics Symposium*, pp. 141–144, 2004.

- [20] T. Johansen, J. Deibele, S.-E. Måsøy, R. Hansen, and B. Angelsen, “Design and Test of a Dual-Layer, Dual Frequency SURF Array,” in *Proceedings of the 31st Scandinavian Symposium on Physical Acoustics, ISBN 978-82-8123-007-1*, January 2008.
- [21] B. Angelsen, *Ultrasound imaging Waves, signals and signal processing Vol I*. Trondheim: Emantec, 2000.
- [22] “Matlab documentation.” [Online]. Available: <http://www.mathworks.com/access/helpdesk/help/toolbox/signal/tukeywin.html>.
- [23] “Comsol multiphysics, acoustics module, user’s guide, version 3.5a.”
- [24] M. Sambridge and G. Drijkoningen, “Genetic algorithms in seismic waveform inversion,” *Geophys. J. Int.*, vol. 109, pp. 323–342, 1992.
- [25] S. Dosso, “Overview of inverse theory in underwater acoustics,” in *Proceedings of the European Conference on Underwater Acoustics*, (Delft), 2004.
- [26] Article number ATE835, Joel Svenssons Vaxfabrik AB, Skalderhus SE-266 94 Munka Ljungby, Sweden.
- [27] Laust Pedersen, tabulated data of material properties, [Online]. Available: [http://www.ondacorp.com/tecref\\_acoustictable.html](http://www.ondacorp.com/tecref_acoustictable.html).
- [28] Ferroperm material tolerances, [Online]. Available: [www.ferroperm-piezo.com/](http://www.ferroperm-piezo.com/).
- [29] J. Kocbach, *Finite element modeling of ultrasonic piezoelectric transducers*. Phd, University of Bergen, Bergen, Norway, 2000.



# A dual frequency transducer applied for fluid film detection through steel using radiation force

Tarjei Rommetveit<sup>1</sup>, Tonni F. Johansen<sup>2</sup> and Roy Johnsen<sup>1</sup>

<sup>1</sup>Department of Engineering Design and Materials, NTNU, Trondheim, Norway,

<sup>2</sup>Department of Circulation and Medical Imaging, NTNU, Trondheim, Norway

## Abstract

In this work, a dual frequency transducer applied for water film detection through steel using radiation force is investigated. The transducer consists of two active piezoelectric elements with an operating frequency separation of about 1:10 and separated with a frequency selective isolation layer. The method is based on manipulating the water film surface with the low frequency (LF) radiation pressure, while the high frequency (HF) pulse detects the film. Acoustic crosstalk from the LF to the HF element introduces unwanted noise. A theoretical framework for evaluating such crosstalk is therefore presented. For the measurements, an empirical approach to crosstalk reduction is performed, and it is shown that the crosstalk suppression is about 15-20dB. The measurements further show that, by applying the radiation force, it is possible to isolate the water film echo from the strong steel reverberations *in situ*, hence making it possible to estimate thin film thickness without the use of any reference signals.

Is not included due to copyright



# Two-way nonlinear manipulation in plane materials using dual frequency band pulse complexes

Tarjei Rommetveit<sup>1</sup>, Tonni F. Johansen<sup>2</sup>, Jochen Deibele<sup>2</sup>, Halvard Kaupang<sup>2</sup> and Bjørn Angelsen<sup>2</sup>

<sup>1</sup>Department of Engineering Design and Materials, NTNU, Trondheim, Norway,

<sup>2</sup>Department of Circulation and Medical Imaging, NTNU, Trondheim, Norway

## Abstract

In this work a one dimensional model based on plane wave, linear acoustics is formulated. It is used to estimate the two-way nonlinear delay,  $\tau$ , obtained in a planar layer between two semi-infinite materials using a dual frequency band method where two pulses with a large frequency separation are transmitted simultaneously and coaxially. The model handles broadband low frequency (LF) pulses as well as the continuous wave situation which in turn generates standing low frequency waves (SW) in the layer. For SW the model finds the phase relationship between the high frequency pulse and the LF wave which maximizes  $\tau$  given the boundary conditions (BCs) and the linear acoustic parameters of the layer in addition to the incoming pressure. The model is compared with a one dimensional nonlinear simulation tool based on the spectral element method for which the results correspond well. An experiment is performed to study  $\tau$  as a function of the BCs in a water layer. The measurements are compared with simulations and it is shown how  $\tau$  is related to the nonlinearity parameter  $B/A$ .

## D.1 Introduction

Understanding of nonlinear wave propagation becomes increasingly important with more sophisticated ultrasound techniques and applications. Nonlinear effects are e.g. utilized for second harmonic imaging [1, 2] and for nonlinear characterization of materials for which several techniques have been developed. As the current work is related to estimating the nonlinearity parameter  $B/A$ , a short review of such methods are given: The thermodynamic approach relies on estimating  $B/A$  by investigating the change in phase velocity as a function of hydrostatic pressure and temperature [3, 4]. Finite amplitude techniques estimate  $B/A$  by examining the fundamental and  $2^{nd}$  harmonic component of the received waveform [5, 6]. Using dual-frequency band pulses is another approach which has been used for estimating the spatial varying  $B/A$  parameter in heterogeneous media such as tissue. The idea is then that a low frequency (LF) pulse, which is transmitted only, manipulates the acoustic properties of the medium. A high frequency (HF) pulse, which is both transmitted and received, then propagates under the influence of the LF pulse. Based on this interaction,  $B/A$  can be estimated. One approach is to transmit the LF wave perpendicular to the HF pulse and estimate  $B/A$  from the accumulated HF phase shift [7, 8]. A reflection mode imaging approach of  $B/A$  is given by Cain [9] where the phase shift of a sinusoidal HF waveform can be derived due to nonlinear interaction with the LF pulse propagating in the opposite direction. A pulse-echo approach where the LF pulse and HF pulse is transmitted simultaneously and coaxially is given in [10]. The HF pulse is then positioned on the flank of the LF pulse causing a nonlinear frequency shift which is used for estimating  $B/A$ .

In medical pulse-echo applications nonlinear propagation can usually be ignored for the backscattered wave. However, if a strong reflector is present, as often is the case in non-destructive evaluation applications, nonlinear effects occur both forwards and backwards. There are three main objectives of this work. The first is to formulate a model for the two-way nonlinear delay,  $\tau$ , obtained using a dual frequency method where two pulses with a large frequency separation are transmitted simultaneously and coaxially. The model makes it possible to calculate  $\tau$  in a plane layer as a function of  $B/A$ , the boundary conditions and the linear acoustic parameters. Further, it handles arbitrary incoming LF pulse shapes as well as the continuous wave (CW) situation leading to standing LF waves (SW) in the layer. Note that in the current work, SW also refer to partial standing LF waves. The current model is based on two underlying hypotheses which greatly simplifies the analysis: Firstly,  $\tau$  may be approximated using linear acoustics. Secondly, it is sufficient to analyze properties of the LF pressure when calculating  $\tau$ . This means that issues such

as HF amplitude, HF pulse length and HF pulse distortion is disregarded in the analysis. It should be noted that the described method is a variant of a technique known as SURF which is an acronym for *Second order Ultrasound Field*. SURF has previously been studied in relation to medical ultrasound for e.g. reverberation suppression [11, 12] and contrast agent detection [13–15].

The second objective is to verify the proposed model, and herein it is verified with measurements and nonlinear simulations. The measurements are performed using a dual frequency band linear array where  $\tau$  is estimated in a water layer as a function of various parameters. Two different reflectors are used in order to quantify the two-way nonlinear manipulation. Since  $\tau$  is directly related to the nonlinearity parameter, it is also described how the experimental setup in combination with the proposed model can be used for estimating  $B/A$ . The nonlinear simulations are performed using a one dimensional (1D) simulation program based on the spectral element model (SEM) with the aim of looking more carefully into errors introduced by the proposed model due to the hypotheses it relies on.

The last objective in this paper is to investigate SW simulation results obtained using the proposed model. It is important to note that SW in this work refers to standing LF waves, and that the HF pulse still is broadband. SW may be important in applications where thin layers relative to the LF pulse length is analyzed or in cases where it is challenging to achieve a sufficient high manipulation pressure in the layer of interest using short LF pulses. One such example is if a low impedance material is to be investigated through a high impedance material such as steel. Then SW may be generated in order to produce a higher manipulation pressure leading to observable nonlinear effects.

## D.2 Theory

### D.2.1 Background; Forward Propagation

Herein, dual band pulses with a large frequency separation ( $\sim 1:10$ ) are employed. Examples are shown in Figure E.1 where the HF pulse,  $y_{HF}$ , is placed on the maximum, the flank and on the minimum of the LF pulse,  $y_{LF}$ . The idea is that  $y_{LF}$ , which is transmitted only, manipulates the acoustic properties of the material such as the sound speed. It is therefore also called the manipulation pulse. The pulse complexes,  $y$ , are modeled in time domain as  $y(t) = y_{HF}(t) \pm y_{LF}(t)$ . It is clear that  $y_{HF}$  can be extracted from  $y$  by a suitable band-pass filter. When taking nonlinear propagation into account, the sound speed,  $c$ , in a material is a function of the manipulation pressure,  $p_m$ ,

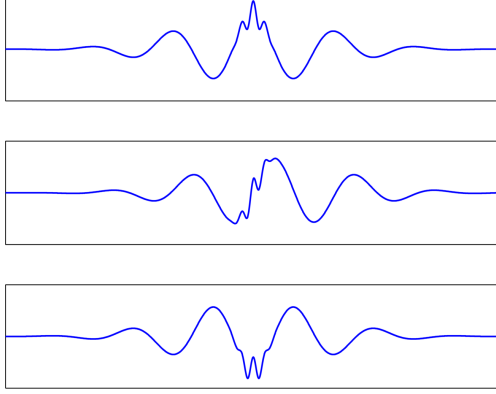


Figure D.1: Examples of transmitted dual frequency pulses with different phase relationships between  $y_{HF}$  and  $y_{LF}$ .  $y_{HF,+}(0, p_m)$ ,  $y_{HF,+}(\pi/2, p_m)$ ,  $y_{HF,-}(0, p_m)$  is presented in the upper, middle and lower plot respectively.

and can be approximated as [16]:

$$c(p_m) \approx c_0 / \sqrt{1 - 2\beta_n \kappa p_m} \approx c_0(1 + \beta_n \kappa p_m) \quad (\text{D.1})$$

Here  $c_0$  is the constant linear sound speed,  $\beta_n$  is related to the  $B/A$  parameter as  $\beta_n = 1 + B/(2A)$  and  $\kappa$  is the compressibility of the material. Note that in the rest of this manuscript,  $\beta_n$  is used for convenience. If the length of  $y_{HF}$  is sufficiently short compared to the LF period one can assume that the manipulation pressure can be separated into a time varying and an average component. The former then causes an expansion or compression of  $y_{HF}$  depending on the local slope of  $y_{LF}$  while the latter leads to a slight change in the travel time. To incorporate the nonlinear effects,  $y_{HF}$  is modeled as (neglecting the time-variable,  $t$ ):

$$y_{HF} = y_{HF,\pm}(\varphi, p_m) \quad (\text{D.2})$$

where  $\varphi$  reflects the phase between  $y_{HF}$  and  $y_{LF}$  and the subscript ' $\pm$ ' indicates the polarity of  $y_{LF}$ . Here,  $\varphi = 0$  refers to the phase with maximal positive peak value of  $p_m$  given a positive polarity of  $y_{LF}$ . If one wants to promote expansion/compression of  $y_{HF}$ , it should be placed on the flank of  $y_{LF}$  where the time varying component of the sound speed is largest, while placing it on the maximum or minimum of  $y_{LF}$  promotes  $\tau$ . For a given  $p_m$  transmitted (assuming plane waves) into a homogeneous, non-dispersive half-space, the largest delay,  $\tau_{max}$ , with respect to the pulse with no manipulation,  $y_{HF}(\varphi, 0)$ , is obtained by transmitting  $y_{HF,+}(0, p_m)$  or  $y_{HF,-}(0, p_m)$ . This is illustrated in Figure D.2. Assuming that  $y_{HF}$  has infinitesimal amplitude and neglecting

the effect of compression/expansion,  $\tau_{max}$  can be expressed when propagating from  $z = 0$  to  $z = L$  as [17]:

$$\tau_{max} = \int_0^L (1/c_0 - 1/[c_0(1 + \beta_n \kappa p_m(z))]) dz \quad (\text{D.3})$$

where the spatial dependence of  $p_m$  is taken into account. If  $p_m$  is constant with  $z$ , the approximation  $\tau_{max} \approx L\beta_n \kappa p_m / c_0$  is obtained. Based on measurements,  $\tau_{max}$  can be estimated by a (sub-sample) time delay estimation scheme such as correlation [18].

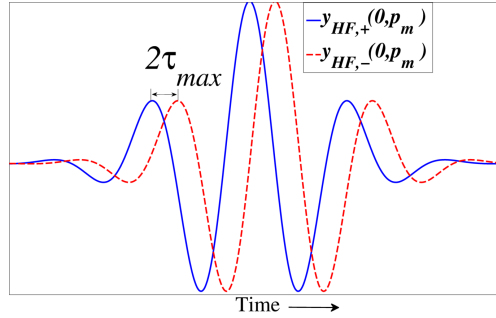


Figure D.2: Two time-shifted HF pulses due to accumulated delay after propagating a distance  $L$  and after bandpass-filtering.

### D.2.2 Derivation of the proposed pulse echo model

For strong reflectors, the reflected manipulation pressure cannot be neglected. As it is desired to describe the two-way nonlinear delay with a linear model, assumptions must be made. The most important are:

1. Nonlinear propagation of  $y_{LF}$  can be neglected.
2. Compression/expansion effects and nonlinear distortion of  $y_{HF}$  can be neglected.
3. The spatial extent of the HF pulse is much shorter than one LF wavelength,  $\lambda_{LF}$ . Hence it can be assumed that all of  $y_{HF}$  experiences approximately the same manipulation pressure.
4. The delay,  $\tau$ , can be estimated by the manipulation pressure experienced by  $y_{HF}$ .

Throughout this section, the pressure field will be given in time domain as  $p_{i\pm}(t; z)$  or in frequency domain as  $p_{i\pm}(\omega; z) = P_{i\pm}(\omega)e^{\mp jk_i z}$  where the subscript  $i$  indicates the material,  $P_{i\pm}$  is the complex amplitude of the pressure wave,  $j = \sqrt{-1}$  and  $\omega = 2\pi f_{LF}$  is the angular frequency. Finally,  $k_i = \omega/c_i(1 - j/(2Q_i))$ ,  $c_i$  and  $Q_i$  are the complex wave number, the sound speed and the mechanical Q-value of material  $i$  respectively. The subscript  $\pm$  gives the direction of the wave.

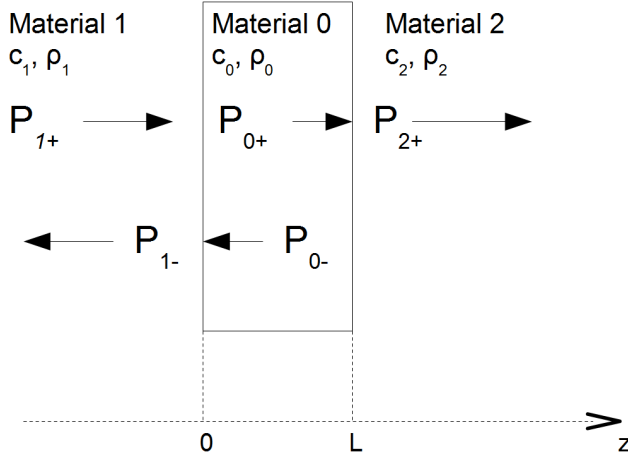


Figure D.3: FIG. 2 Viscoelastic layer (Material 0) between two semi-infinite materials with  $p_{1+}$  coming in from left infinity.  $c_i$  and  $\rho_i$  are the sound speed and density of material  $i$  respectively for  $i = 0,1,2$ .

Consider the normal incident plane wave  $p_{1+}$  propagating in from the left along the  $z$ -axis as shown in Figure D.3. The structure illustrates a viscoelastic layer, Material 0, with thickness  $L$  submersed between two semi-infinite media. As  $p_{1+}$  hits the interface between Material 1 and Material 0, it will be partially transmitted and reflected producing  $p_{0+}$  and  $p_{1-}$  respectively. The same phenomenon will occur for  $p_{0+}$  at the  $2^{nd}$  interface between Material 0 and 2 producing  $p_{2+}$  and  $p_{0-}$  respectively. The following relations can be obtained between the complex amplitudes [19]:

$$\begin{aligned} P_{0+}(\omega) &= P_{1+}(\omega)T_{10}/(1 - R_{01}R_{02}e^{-j2k_0L}) \\ P_{0-}(\omega) &= P_{1+}(\omega)T_{10}R_{02}e^{-j2k_0L}/(1 - R_{01}R_{02}e^{-j2k_0L}) \end{aligned} \quad (\text{D.4})$$

Here  $R_{ik}$  and  $T_{ik}$  are the normal incident reflection and transmission coefficients from material  $i$  to material  $k$  respectively. The total pressure in medium 0 is

now given as a superposition of the forward and backward propagating wave:

$$p_0(\omega; z) = P_{0+}(\omega)e^{-jk_0z} + P_{0-}(\omega)e^{jk_0z} \quad (\text{D.5})$$

The transfer function from  $P_{1+}(\omega)$  to  $p_0(\omega, z)$  is given by combining Eq. (D.4) and Eq. (D.5):

$$H(\omega, z) = \frac{p_0(\omega, z)}{P_{1+}(\omega)} = \frac{T_{10}[e^{-jk_0z} + R_{02}e^{-j2k_0L}e^{jk_0z}]}{1 - R_{01}R_{02}e^{-j2k_0L}} \quad (\text{D.6})$$

In order to estimate the accumulated delay, the experienced manipulation pressure,  $p_0(t)$ , is tracked for a wavelet with infinitesimal extent in time traveling back and forth in medium 0. When travelling forwards, the position of this point can be expressed as a function of  $t$ :

$$z = c_0t, t \in [0, L/c_0] \quad (\text{D.7})$$

In a similar manner, the position when travelling backwards can be expressed as:

$$z = 2L - c_0t, t \in [L/c_0, 2L/c_0] \quad (\text{D.8})$$

Given  $P_{1+}$ ,  $p_0(t)$  is found in the forward and backward direction using the inverse Fourier transform:

$$p_0(t) = \left\{ \begin{array}{l} p_0(t; z)|_{z=c_0t} = \\ \int H(\omega, c_0t) \cdot \frac{P_{1+}(\omega)}{2\pi} \cdot e^{j\omega t} d\omega, \quad t \in \left[0, \frac{L}{c_0}\right] \\ p_0(t; z)|_{z=2L-c_0t} = \\ \int H(\omega, 2L - c_0t) \frac{P_{1+}(\omega)}{2\pi} \cdot e^{j\omega t} d\omega, t \in \left[\frac{L}{c_0}, \frac{2L}{c_0}\right] \end{array} \right\} \quad (\text{D.9})$$

The delay between  $y_{HF}(\varphi, 0)$  and  $y_{HF}(0, p_0)$  becomes:

$$\tau = \int dz/c_0 - \int dz/c(p_0(t)) \approx \kappa \cdot \beta_n \int p_0(t) dt \quad (\text{D.10})$$

Two approximations are performed in Eq. (D.10): (a) A 1<sup>st</sup> order Taylor expansion of  $(c - c_0)/c_0$  around zero is carried out, and (b)  $dz$  is approximated as  $dz = c(p_0)dt \approx c_0dt$ . It is clear that  $\beta_n$  and hence  $B/A$  can be estimated from Eq. (D.10).

Note that the current model can be extended to analyzing nonlinear propagation effects of a single layer in multilayer structures or transducer stacks by replacing the real-valued reflection coefficients  $R_{01}$  and  $R_{02}$  in Eq. (D.4) with the complex-valued lumped circuit equivalents of the structure which is part of the analysis. A more detailed analysis of this is considered as further work.

### D.2.2.1 Special case: Standing LF waves

For CW some simplifications can be performed as  $\omega$  is constant and  $p_0(t; z) = \text{Re}\{p_0(z)e^{j\omega t}\}$ . The position of  $y_{HF}$  is related to  $y_{LF}$  through the phase,  $\varphi$ , of  $P_{1+} = |P_{1+}|e^{j\varphi}$ . Hence Eq. (D.9) can be rewritten as

$$p_0(t) = \left\{ \begin{array}{l} \text{Re}\{H(c_0t) \cdot |P_{1+}|e^{j\varphi} \cdot e^{j\omega t}\}, \quad t \in [0, L/c_0] \\ \text{Re}\{H(2L - c_0t) \cdot |P_{1+}|e^{j\varphi} \cdot e^{j\omega t}\}, \quad t \in \left[\frac{L}{c_0}, \frac{2L}{c_0}\right] \end{array} \right\} \quad (\text{D.11})$$

The integral in Eq. (D.10) can then be calculated as:

$$\tau = \kappa \cdot \beta_n \text{Re}\{P_{1+}A\} = \kappa \cdot \beta_n |P_{1+}| |A| \cos(\varphi + \theta) \quad (\text{D.12})$$

where  $A = |A|e^{j\theta}$  and  $A$  is expressed as:

$$A = \frac{T_{10}}{1 - R_{01}R_{02}e^{-j2k_0L}} \left( \frac{2Q}{\omega} (1 - \alpha^L + R_{02}(\alpha^L - \alpha^{2L})) + R_{02}(\alpha^L - e^{-j2k_0L}) + e^{j2k_rL} - \alpha^L/\omega (1/(2Q) + 2j) \right) \quad (\text{D.13})$$

In Eq. (D.14) the attenuation factor  $\alpha = e^{-k_r/(2Q)}$  is defined and  $k_r = \omega/c_0 = \text{Re}\{k_0\}$ . If a non-attenuating medium is investigated, care must be taken as the first term is a 0/0 expression when  $Q \rightarrow \infty$ . Applying L'Hopita's rule then yields:

$$\lim_{Q \rightarrow \infty} A = \frac{T_{10}}{1 - R_{01}R_{02}e^{-j2k_rL}} \left( \frac{L}{c_0} (1 + R_{02}) + \frac{R_{02}(1 - e^{-j2k_rL}) + e^{j2k_rL} - 1}{2j\omega} \right). \quad (\text{D.14})$$

The optimal delay  $\tau_{max}$  can be found through the optimization  $\tau_{max} = \arg \max_{\varphi, L/\lambda_{LF}} \tau$ .

The phase corresponding to  $\tau_{max}$  is denoted  $\varphi_{max}$ .

## D.3 Methods

### D.3.1 Measurements

A pulse-echo experiment was performed in order to quantify the two-way non-linear manipulation in a de-ionized water layer. A bi-layer, dual frequency

probe designed inhouse and manufactured by Vermon (Tours, France) was connected to a modified Ultrasonix SonixRP (Richmond, Canada) scanner for data recording. In order to achieve common aperture for the two frequency bands, the HF elements and the LF elements are organized in a stack only separated with a low impedance isolation layer with thickness  $\lambda_{HF}/4$ . Here  $\lambda_{HF}$  refers to the wavelength in the center of the HF passband for the isolation layer material. The isolation layer is introduced in order to avoid ripple in the HF passband. The center frequencies of the probe are 0.9MHz and 7.5MHz for the LF array and HF array respectively and they were excited with 5 and 3 half cycle square pulses with center frequencies of 0.9MHz and 8MHz respectively. The reason for elevating the excitation frequency relative to the centre frequency of the HF array, is to avoid an unwanted resonance in the lower part of the HF passband. The HF aperture was  $7 \times 7 \text{mm}^2$  and the LF aperture  $14 \times 21 \text{mm}^2$  with the HF aperture located in the centre of the LF aperture. For a more thorough review of the principles of design for a similar probe, see [20].

Plane waves were transmitted from both apertures and it was operated in the diffraction limited near-field of the transducer in order to avoid phase-sliding between the LF and HF pulses. The large LF aperture compared to the HF aperture was chosen in order to maintain a relatively constant manipulation pressure over the HF beam. On receive, 40 lines were recorded, and for each line the data was averaged 20-30 times. The probe was attached to a Physik Instrumente (Karlsruhe, Germany) multistage robot for controlling the distance,  $L$ , between the probe and reflector. The ultrasound beam was aligned perpendicular to the reflector. The thickness of the reflector was much larger than the spatial extent of  $y$ . Hence the model assumption of a semi-infinite boundary medium (Material 2) was satisfied. By changing the material of the reflector (plexiglass and steel), it was possible to study the two-way nonlinear manipulation because  $\tau$  will increase as a function of  $R_{02}$  for  $R_{02} > 0$ . The characteristic impedance,  $Z_2 = \rho_2 c_2$ , was determined for both plexiglass and steel by weighing a rectangular sample with known volume, and by measuring the sound speed in a pulse echo arrangement. The setup, except for the scanner, is shown in Figure D.4 while the acoustic parameters of the reflectors are shown in Table D.1. The sound speed in water was determined from measuring the temperature with a thermocouple and a multimeter, and using the equations given in [21].

In order to obtain the output manipulation pressure from the transducer, the probe was pre-calibrated in a water tank for 25V transmit voltage and it was assumed that the voltage-pressure relationship was linear. For the water tank calibration measurements, an  $85 \mu\text{m}$  ONDA HGL-0085 hydrophone with

a 20-dB pre-amplifier was used (Onda Corporation, Sunnyvale, U.S.A.). The hydrophone was fixed to the aforementioned robot and the pulses were recorded using a LeCroy WaveSurfer 42Xs (LeCroy, Geneva, Switzerland) oscilloscope.

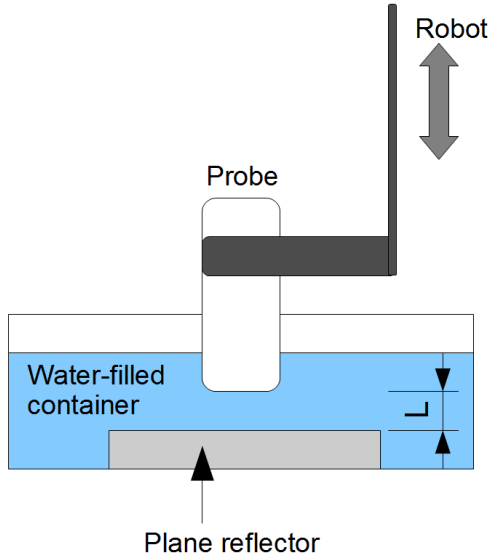


Figure D.4: Experimental setup.

Table D.1: Material parameters

	Water	Plexiglass	Steel
$\beta_n$	3.5	-	-
$c$ [m/s]	1486	2783	5970
$\rho$ [kg/m <sup>3</sup> ]	1000	1182	7790

### D.3.2 Simulations

In all simulations the following common parameters are used:  $\rho_0 = 1000\text{kg/m}^3$  and  $\beta_n=3.5$  (assuming density and nonlinearity parameter of water).

#### D.3.2.1 The SEM tool

A time-domain SEM [22] is used to compute the nonlinear solutions. It is not in the scope of this work to fully investigate this tool, but a brief description

of the model and the verification procedures are given in the following: The SEM tool is based on a variational formulation of the acoustic models given by Tabei *et al.* [23] and Yuan *et al.* [24] and it uses high-order ( $N=16$ ) Lagrange polynomials to approximate the solution. The underlying model of the SEM tool is modified to include a pressure dependent speed of sound similar to the middle term of Eq. (E.1). The absorption model is the same as in [23, 24] and is based on a theoretical formulation for frequency dependent absorption and phase velocity presented by Nachman *et al.* [25].

To verify the absorption model for a wide range of frequencies a chirp signal constructed from a linear frequency sweep from 500kHz to 4MHz is simulated. The frequency dependent absorption and phase velocity is estimated from a SEM simulation and compared with the theoretical results from [25]. The errors are measured in the L2 norm for the frequency range 0-6 MHz, and are  $1.45 \cdot 10^{-3}$  for the absorption and  $0.24 \cdot 10^{-3}$  for the phase velocity. The nonlinear model is compared with an analytic expression for a CW plane wave propagation in a nonabsorbing medium presented by Pierce [26]. From the SEM solution 32 periods are excerpted for frequency analysis, and the L2 errors are  $0.74 \cdot 10^{-3}$ ,  $7.85 \cdot 10^{-3}$  and  $33.12 \cdot 10^{-3}$  for the first-, second- and third-harmonic component. In this work, the maximum frequency used in the SEM simulations is  $3.5f_{HF}$  where  $f_{HF}$  is the centre frequency of  $y_{HF}$  while the CLF number is 0.5.

### D.3.2.2 Verifying the linear model for broadband LF pulses

First, simulations were performed in order to compare with measurements. Then, several series of simulations were performed in order to validate the proposed model by evaluating it against the SEM tool. In the two first simulation series, the varying parameters were the amplitude of  $p_{0+}$  and the attenuation in Material 0. Then simulations were performed in order to see the effect of increasing the HF amplitude as well as the HF pulse length.  $y_{LF}$  was a 5 half cycles sine burst with a center frequency of 1MHz. In the SEM simulations,  $y_{HF}$  was, if not otherwise stated, a 3 half cycles sine burst with a center frequency of 10MHz. Further  $c_0 = 1500\text{m/s}$ ,  $L = 3\lambda_{LF}$  and  $R_{01} \approx 1$ . For the linear model,  $2\tau$  is obtained directly from the experienced pressure as given in Eq. (D.10), while for the SEM,  $2\tau$  is estimated by correlation between  $y_{HF,+}(\varphi_{max}, p_{0+})$  and  $y_{HF,-}(\varphi_{max}, p_{0+})$ .  $\varphi_{max}$  is referred to the centre of gravity of  $y_{HF}$ . When  $R_{01} > 0$  and  $R_{02} > 0$ , as is the case in these simulations,  $\varphi_{max} = 0$  for broadband LF pulses.

### D.3.2.3 The SW situation

The SW situation is an important special case which can arise if  $L/c_0$  is much less than the LF pulse length. The linear method is then particularly beneficial because SW is computationally expensive to simulate in the nonlinear time domain. When SW occurs, it is not necessarily optimal to transmit  $y_{HF}$  on the maximum and minimum of  $y_{LF}$  as it will interact with the superposition of all the reflected LF waves propagating forwards and backwards in the layer. Hence,  $\tau_{max}$  is simulated together with  $\varphi_{max}$  as a function of  $L/\lambda_{LF}$ . The simulations are performed with the parameters  $f_{LF} = 500\text{kHz}$ ,  $c_0 = 1500\text{m/s}$ ,  $R_{01} \approx 1$  and  $p_{0+} = 1\text{MPa}$ .

In order to verify the SW situation with the SEM tool, a pulse complex with a long LF pulse was transmitted approximating CW.  $y_{HF}$  was not transmitted before the system reached equilibrium. In order to estimate  $\tau_{max}$  and  $\varphi_{max}$  from the nonlinear simulations, an algorithm taking locally variable delays [27] into account was employed in stead of correlation. The linear model was verified around the 2<sup>nd</sup> resonance peak at  $L/\lambda_{LF} = 0.75$  for  $R_{02} = -0.5$ .

## D.4 Results and discussion

### D.4.1 Measurements vs. linear 1D model

The experimental setup does not eliminate the nonlinear effects developed internally in the probe. Hence the measurements include the accumulated nonlinear effects both from the propagation in the probe and the water layer. The internal probe effects are estimated and subtracted from the measured delays by extrapolating a linear regression curve to  $L = 0$ . The numerical value of the material parameters used in the simulations is given in Table D.1.

In Figure D.5 the simulated vs. the measured delays for 5V and 10V transmit voltages are presented. The measurements validate that  $\tau$  is indeed dependent on  $R_{02}$ . The slope of  $\tau(L)$  is higher for the steel reflector than for the plexiglass reflector and larger delays are obtained from the former due to the higher backwards manipulation pressure. Also note that a doubling of the transmit voltage roughly causes a doubling of the delay for a given reflector as expected.

However, there are some simplifications and error sources which are important to be aware of in addition to those mentioned in Section E.2. Firstly, diffraction effects and phase sliding between  $y_{HF}$  and  $y_{LF}$  will occur in the experimental setup to some degree. The measured LF axis scan used for calibrating the model is given in Figure D.6 together with the average pressure.

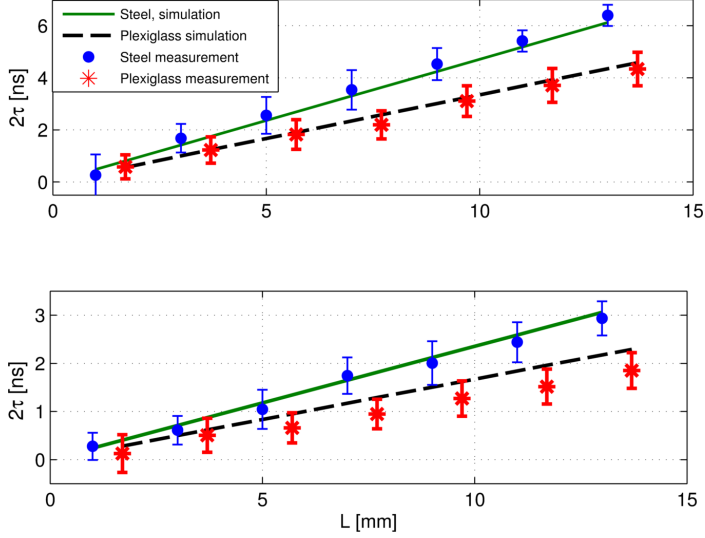


Figure D.5: Measured and simulated delay after subtracting the internal delay in the probe. The delays are obtained given 10V ( $\sim 115\text{kPa}$ ) and 5V ( $\sim 57.5\text{kPa}$ ) transmit voltages in the upper and lower plot respectively. The error bars represent one standard deviation in each direction.

It is clear that the plane wave assumption is violated due to diffraction effects. In the simulations, the average pressure is used as input to the model. For a more thorough discussion of diffraction effects and beamforming strategies for SURF applications, see [28]. Secondly,  $R_{01}$  is complex for any transducer, while in the simulation it is assumed to be real and constant for all frequencies. In order to choose a realistic value of  $R_{01}$  herein, the reflection coefficient magnitude in the centre of the LF passband is employed. This was obtained from simulations of the transducer stack using an in house simulation tool based on the Mason model [29]. Thirdly, the slightest movement of the probe relative to the reflector between measuring  $y_{HF,+}$  and  $y_{HF,-}$  causes large errors. This can occur due to vibrations or positioning errors of the robot. As an example, a  $1\mu\text{m}$  variation of  $L$  will give an error of 1.3ns delay in water. Still, the simulated delays correspond well with the experimental results indicating that the relatively simple linear model catches the main features of a complex nonlinear problem in terms of  $\tau$ .

Even though the main task of this paper is to present and verify the 1D model, it can also be a useful tool for estimation of the nonlinearity parameter. In Figure D.7,  $\beta_n$  in water is estimated as a function of  $L$  using the 10V

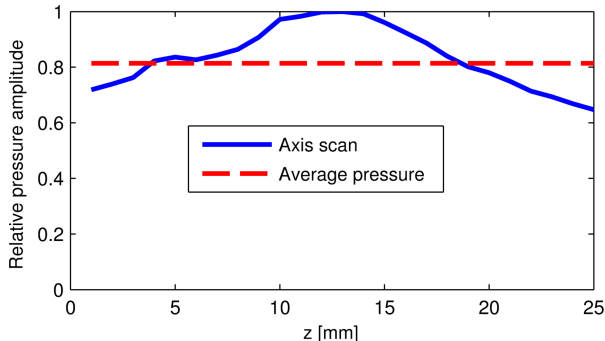


Figure D.6: Measured axis scan of LF pulses and the average pressure used in simulations. The axis scan is based on the maximal pressure amplitude.

measurements results from Figure D.5. The estimation is based on a slight rearrangement of Eq. (D.10):  $\hat{\beta}_n = \hat{\tau} / (\kappa \cdot \int p_0(t) dt)$ . Here  $\hat{\tau}$  is the estimated delay from the measurements. Figure D.7 shows that the uncertainty of  $\hat{\beta}_n$  decreases with  $L$  and  $R_{02}$ . This is equivalent to say that the uncertainty of  $\hat{\beta}_n$  decreases with  $\tau$ . To see this, consider the uncertainty translated into  $\hat{\beta}_n$  from  $\hat{\tau}$ ,  $u_{\hat{\beta}_n}(\hat{\tau})$  [30]:

$$u_{\hat{\beta}_n}(\hat{\tau}) = \sigma_{\hat{\tau}} \cdot \partial \hat{\beta}_n / \partial \hat{\tau} = \sigma_{\hat{\tau}} \cdot \beta_n / \tau \quad (\text{D.15})$$

Here  $\sigma_{\hat{\tau}}$  is the standard deviation of  $\hat{\tau}$ . In the HF nearfield it is sound to assume that  $\sigma_{\hat{\tau}}$  is nearly constant with  $L$ , and this is also supported by the measurements. Hence, Eq. (D.15) indicates that  $u_{\hat{\beta}_n}(\hat{\tau})$  is inversely proportional to  $\hat{\tau}$ . For a better estimate of  $\beta_n$  it should therefore be strived for maximizing  $\hat{\tau}$  by increasing  $R_{02}$ ,  $L$  and the transmit voltage. The reason for only using 10V in the current measurements, is that the receive electronics went into saturation for higher transmit voltages due to the strong reflected LF wave (recall that the electronics is designed for medical use where the backscattered LF wave is negligible.) The estimation procedure will be improved by either including diffraction effects in the model, or by designing an experimental setup enforcing plane waves in a better manner. This is considered as future work.

#### D.4.2 1D Model vs. SEM - Broadband LF pulses

In Figure D.8 results from the SEM model and the linear model for 5 half cycle LF bursts are compared. In the upper plot the amplitude of  $p_{0+}$  is varied, and it can be seen that an excellent agreement between the two models is achieved, with a slightly higher calculated delay for the linear model. The

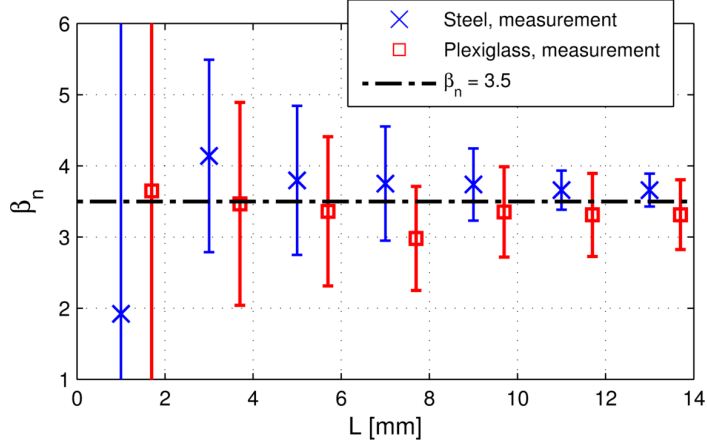


Figure D.7: Estimated nonlinearity parameter based on fitting measurements and simulations. The error bars represent one standard deviation in each direction.

reason for this is twofold: Firstly, the SEM transfers energy to higher harmonics and the sub-harmonic during nonlinear propagation causing the LF amplitude to drop slightly over time compared to for the linear model. Secondly, the SEM simulations employ a HF-pulse that is spread over  $y_{LF}$ , while the linear model assumes an infinitesimal HF pulse-length. Hence the average pressure experienced,  $p_{avg}$ , by  $y_{HF}$  is slightly lower than the maximum manipulation pressure. It is performed a similar series of simulations where  $R_{02} = 0.5$  which yields comparable results. Those results are not reproduced here.

The lower plot in Figure D.8 shows how attenuation affects the two models. They correspond quite well but with a slightly increased deviation as a function of attenuation. The reason for this is that the assumption of non-dispersive media is violated as the attenuation introduces a frequency dependent sound speed for the SEM tool. This causes  $y_{HF}$  to slide away from the maximum of  $y_{LF}$  leading to a decreased  $p_{avg}$ .

### D.4.3 Nonlinear distortion of $y_{HF}$

A series of SEM simulations was performed in a non-attenuating medium in order to analyze the effect nonlinear distortion of the HF pulse has on  $\tau$ . The distortion of  $y_{HF}$  can be given relative to the shock length,  $z_{sh}$  [19]:

$$z_{sh} = c_0^3 \rho / (\omega p_{HF} \beta_n) \quad (\text{D.16})$$

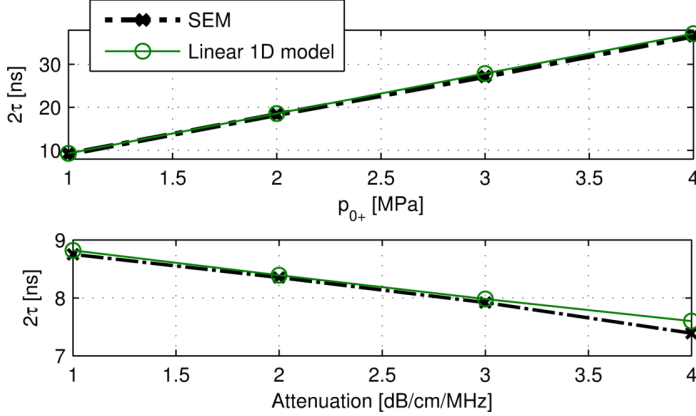


Figure D.8: In the upper plot the models are compared with respect to the amplitude of  $p_{0+}$  in a non-attenuating medium where  $R_{02} = 1$ . In the lower plot, the models are compared with respect to attenuation with the amplitude of  $p_{0+}$  equal to 1MPa and  $R_{02} = 1$ .

Here the HF pressure-amplitude  $p_{HF}$  is assumed and the shock length is given relative to the centre frequency of  $y_{HF}$ . The HF amplitude was varied so that  $y_{HF}$  propagated between  $0.1z_{sh}$  and  $z_{sh}$ . The estimated value of  $\tau$  varied less than 0.4% showing that the HF distortion does not affect the estimate of  $\tau$  significantly. A probable reason for this is given in the following:  $y_{HF,+}(0, p_{0+})$  and  $y_{HF,-}(0, p_{0+})$  can be thought of as two pulses propagating in two different media with slightly different sound speeds. Raising the HF amplitude will not change the experienced sound speed and the mutual translation. It will only change the self distortion of  $y_{HF}$ . But by elevating the HF amplitude, the non-linear self distortion of both  $y_{HF,+}(0, p_{0+})$  and  $y_{HF,-}(0, p_{0+})$  increases jointly in the same manner. Hence the mutual difference between the pulse forms does not increase considerably and correlating between them yields approximately the same answer regardless of the HF amplitude.

#### D.4.4 Influence of HF pulse length

In the proposed model, it is assumed that the extension of  $y_{HF}$  can be neglected in the analysis as it is much less than  $\lambda_{LF}$ . In order to investigate the effect the HF pulse length has on  $\tau$  when  $\tau$  is estimated with correlation, a series of SEM simulations were performed. The extension of  $y_{HF,+}(0, p_{0+})$  and  $y_{HF,-}(0, p_{0+})$  then ranged from 10-70% of  $\lambda_{LF}$ . This corresponds to 1-7 cycle sine bursts with a frequency ratio of 1:10 between  $f_{HF}$  and  $f_{LF}$ . The main results were that by

increasing the extension of  $y_{HF}$  relative to  $\lambda_{LF}$  from 10% to 15% and 25% the estimated  $\tau$  decreases with less than 0.7% and 2.5%. It has, however, decreased with nearly 5% and 35% at 25% and 70% extension. Hence it is of importance to control the HF pulse length in order to obtain a good estimate. In some cases it is obviously necessary to correct for this effect. One approach for HF pulse length correction using the proposed method is to estimate several delays based on different values of  $\varphi$  where each value corresponds to a point on  $y_{HF}$ . Then a weighted approach can be used for correcting for the extension of  $y_{HF}$ . Another approach is to use the algorithm tracking locally variable delays [27] in stead of correlation.

#### **D.4.5 SW simulations**

In cases where it is challenging to transmit enough pressure into the layer of interest, e.g. when examining a material through steel, it may be necessary to transmit a long LF pulse in order to build up SW. If constructive interference is achieved, a higher manipulation pressure is generated which in turn produces a larger delay from the layer. The results in Figure D.9a) and Figure D.9b) show that  $\tau_{max}$  has peaks when  $L$  equals  $n\lambda_{LF}/2$  and  $(2n+1)\lambda_{LF}/4$  for  $R_{02} > 0$  and  $R_{02} < 0$  respectively, where  $n = 1, 2, \dots$ . Further,  $\tau_{max}$  is very phase sensitive as a function of  $L/\lambda_{LF}$ . E.g. with no attenuation, a periodic pattern occurs with the optimal phase of 0 and 90 degrees at the resonance peaks for  $R_{02} = 1$  and  $R_{02} = -1$  respectively. For the cases with attenuation the optimal phase converges in the limit to 0 degrees as  $L/\lambda_{LF} \rightarrow \infty$ . Further,  $\tau_{max}$  increases on average as a function of  $L/\lambda_{LF}$  for all cases except when  $R_{02} = -1$  with 0dB/cm/MHz. Also note that it is more feasible to obtain larger  $\tau_{max}$  when  $R_{02} > 0$ . The reason for this is that when  $R_{02} < 0$ , the nonlinear manipulation for the backward propagation has opposite polarity compared to the forward propagation causing the accumulated delay to decrease on the way back from the reflector.

In Figure D.10 the SW situation is compared between the SEM tool and the linear model with respect to  $\tau_{max}$  and  $\varphi_{max}$  in an attenuating medium. A good correspondence between the two models is obtained and the deviation is less than 6.4% for the estimated delays. The deviation in  $\varphi_{max}$  is less than 6.4 degrees corresponding to 1.8% of one LF period. A similar comparison is also performed in the non-attenuating case for which the correspondence between the two models is even better. This is probably due to the differences in the sound speed models when loss is introduced as discussed earlier in the paper. Hence, the deviation between the two models will most likely increase as a function of attenuation. For the case without attenuation, which is not

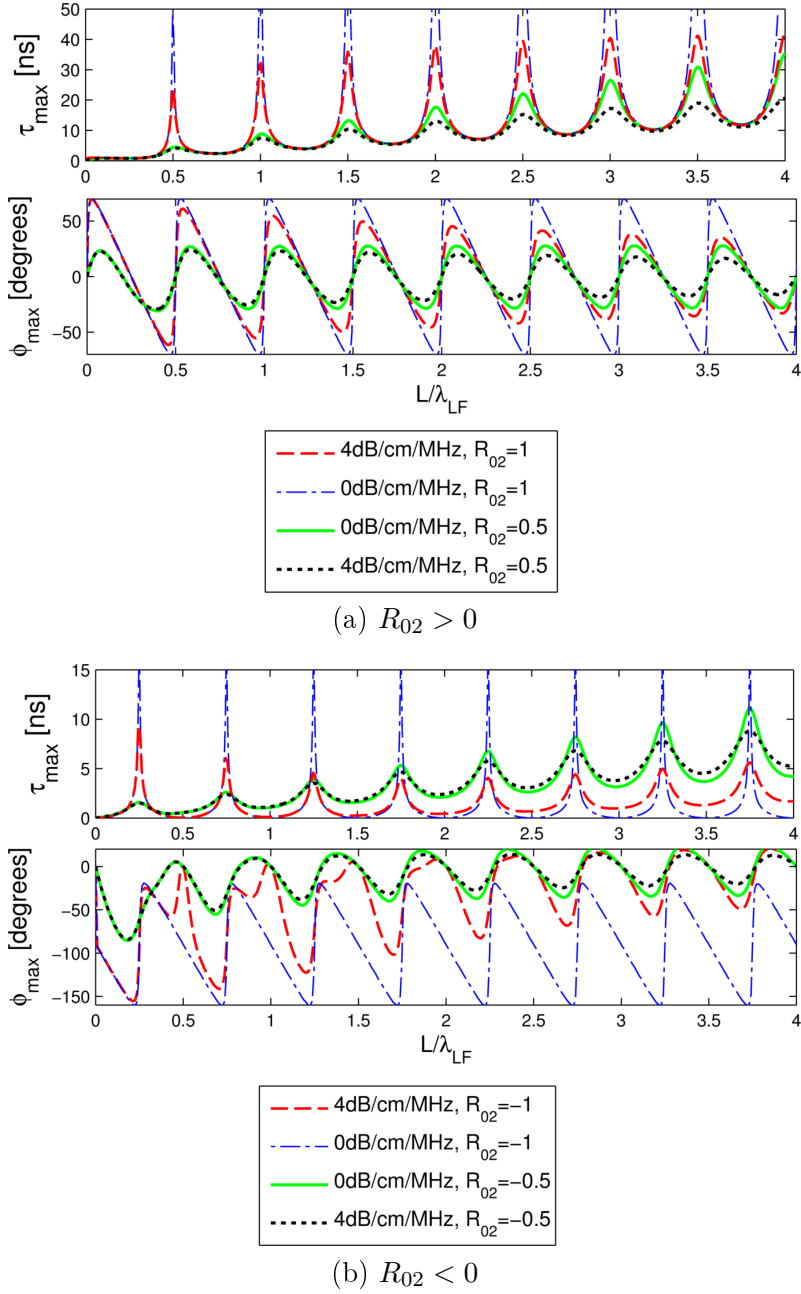


Figure D.9:  $\tau_{max}$  and the corresponding phase for different situations.

graphically reproduced herein, the deviation in  $\tau_{max}$  is less than 3.7% while the deviation in  $\varphi_{max}$  is less than 5.1 degrees corresponding to 1.4% of one LF period. In general it seems that the linear model slightly overestimates  $\tau_{max}$  relative to the SEM tool.

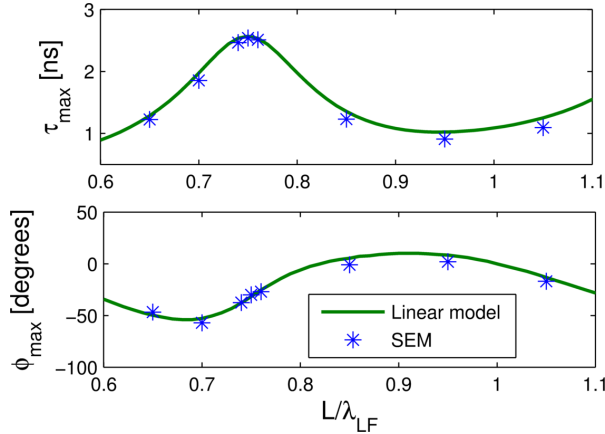


Figure D.10: Comparison of the SEM tool and the linear model with respect to  $\tau_{max}$  and  $\varphi_{max}$  for the SW situation. The attenuation is 2dB/cm/MHz.

Figure D.11 shows as an example  $p_0(t)$  for an infinitesimal wavelet propagating with the phase  $\varphi_{max}$  relative to  $y_{LF}$ . As  $y_{HF}$  propagates on a SW pattern, the experienced pressure is oscillating with  $f_{LF}$  in a somewhat complex manner. In this case the forward propagation is characterized by a positive experienced manipulation pressure, while the backward propagation is distinguished by an on average negative experienced manipulation pressure due to that  $R_{02} < 0$ . However, the total average pressure for the two-way propagation is positive. The current model can hence be used to study  $p_0(t)$  for various scenarios, increasing the understanding of such problems. An excellent correspondence with the SEM tool is obtained in this particular case.

## D.5 Conclusions

A model calculating the two-way nonlinear delay for plane wave, dual frequency band ultrasound is formulated and verified. The results demonstrate that the model corresponds well with both experimental data and the SEM tool. It is shown that the deviation between the linear simulations and the nonlinear simulations increases slightly with attenuation due to the dispersion effects that are introduced by the SEM tool. It is also shown through simulations that the

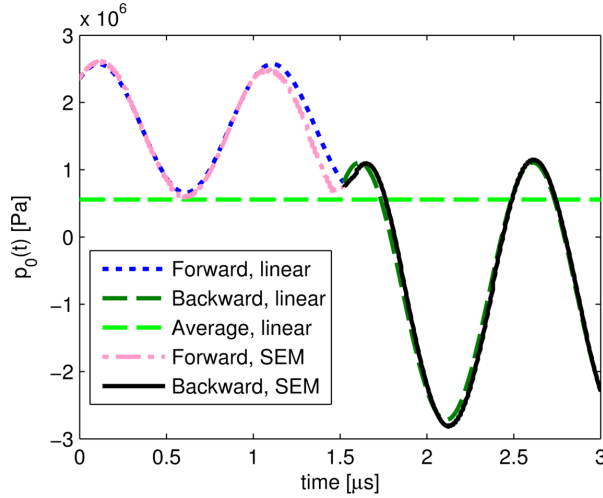


Figure D.11: An example of the experienced pressure  $p_0(t)$  which yields  $\tau_{max}$  when the attenuation is zero,  $L/\lambda_{LF} = 0.76$  and  $R_{02} = -0.5$ .

HF amplitude is negligible when estimating  $\tau$ , and that the extension of  $y_{HF}$  relative to  $\lambda_{LF}$  should be corrected for in order to obtain an optimal estimate. The model increases the understanding of how the nonlinear delays accumulate in various pulse-echo setups and it can be a valuable tool for nonlinear material characterization. Another advantage is that the current model significantly reduces the computational requirements relative to nonlinear simulation tools.

# References

- [1] M. Averkiou, D. Roundhill, and J. Powers, “A new imaging technique based on the nonlinear properties of tissues,” in *Proceedings of the IEEE International Ultrasonics Symposium*, vol. 2, pp. 1561–1566, 1997.
- [2] M. Averkiou, “Tissue harmonic imaging,” in *Proceedings of the IEEE International Ultrasonics Symposium*, pp. 1563–1572, 2000.
- [3] Z. Zhu, M. S. Roos, W. N. Cobb, and K. Jensen, “Determination of the acoustic nonlinearity parameter  $b/a$  from phase measurements,” *The Journal of the Acoustical Society of America*, vol. 74, no. 5, pp. 1518–1521, 1983.
- [4] C. M. Sehgal, R. C. Bahn, and J. F. Greenleaf, “Measurement of the acoustic nonlinearity parameter  $b/a$  in human tissues by a thermodynamic method,” *The Journal of the Acoustical Society of America*, vol. 76, no. 4, pp. 1023–1029, 1984.
- [5] W. N. Cobb, “Finite amplitude method for the determination of the acoustic nonlinearity parameter  $b/a$ ,” *The Journal of the Acoustical Society of America*, vol. 73, no. 5, pp. 1525–1531, 1983.
- [6] S. Saito, “Finite amplitude method for measuring the nonlinearity parameter  $b/a$  in small-volume samples using focused ultrasound,” *The Journal of the Acoustical Society of America*, vol. 127, no. 1, pp. 51–61, 2010.
- [7] N. Ichida, T. Sato, and M. Linzer, “Imaging the nonlinear ultrasonic parameter of a medium,” *Ultrasonic Imaging*, vol. 5, pp. 295–299, 1983.
- [8] T. Sato, Y. Yamakoshi, and T. Nakamura, “Nonlinear tissue imaging,” in *Proceedings of the IEEE International Ultrasonics Symposium*, pp. 889–900, 1986.

- 
- [9] C. A. Cain, "Ultrasonic reflection mode imaging of the nonlinear parameter B/A: I. A theoretical basis," *The Journal of the Acoustical Society of America*, vol. 80, no. 1, pp. 28–32, 1986.
- [10] S.-I. U. H. Fukukita and T. Yano, "Ultrasound pulse reflection mode measurement of nonlinearity parameter B/A and attenuation coefficient," *The Journal of the Acoustical Society of America*, vol. 99, no. 5, pp. 2775–2782, 1996.
- [11] S. P. Näsholm, R. Hansen, S. Måsøy, T. F. Johansen, and B. A. J. Angelsen, "Transmit beams adapted to reverberation noise suppression using dual-frequency SURF imaging," *IEEE Transactions on Ultrasonics, Ferroelectrics, and Frequency Control*, vol. 56, pp. 2124–2133, Oct. 2009.
- [12] R. Hansen, S. Måsøy, T. F. Johansen, and B. A. Angelsen, "Utilizing dual frequency band transmit pulse complexes in medical ultrasound imaging," *The Journal of the Acoustical Society of America*, vol. 127, no. 1, pp. 579–587, 2010.
- [13] B. A. J. Angelsen and R. Hansen, "SURF Imaging - A new Method for Ultrasound Contrast Agent Imaging," in *Proceedings of the IEEE International Ultrasonics Symposium*, pp. 531–541, 2007.
- [14] R. Hansen and B. Angelsen, "SURF imaging for contrast agent detection," *Ultrasonics, Ferroelectrics and Frequency Control, IEEE Transactions on*, vol. 56, no. 2, pp. 280–290, 2009.
- [15] S.-E. Måsøy, Ø. Standal, P. Näsholm, T. F. Johansen, B. A. J. Angelsen, and R. Hansen, "SURF Imaging: In vivo demonstration of an ultrasound contrast agent detection technique," *IEEE Transactions on Ultrasonics, Ferroelectrics, and Frequency Control*, vol. 55, pp. 1112–1121, May 2008.
- [16] B. Angelsen, *Ultrasound imaging Waves, signals and signal processing Vol II*. Trondheim: Emantec, 2000.
- [17] S. P. Näsholm, *Ultrasound beams for enhanced image quality*. Phd, Department of Circulation and Medical Imaging, Norwegian University of Science and Technology, Trondheim, Norway, 2008. ISBN 978-82-471-9130-9.
- [18] G. Jacovitti and G. Scarano, "Discrete time techniques for time delay estimation," *Signal Processing, IEEE Transactions on*, vol. 41, pp. 525–533, Feb. 1993.

- [19] B. Angelsen, *Ultrasound imaging Waves, signals and signal processing Vol I*. Trondheim: Emantec, 2000.
- [20] T. Johansen, J. Deibele, S.-E. Måsøy, R. Hansen, and B. Angelsen, “Design and Test of a Dual-Layer, Dual Frequency SURF Array,” in *Proceedings of the 31st Scandinavian Symposium on Physical Acoustics, ISBN 978-82-8123-007-1*, January 2008.
- [21] J. Lubbers and R. Graaff, “A simple and accurate formula for the sound velocity in water,” *Ultrasound in Medicine & Biology*, vol. 24, no. 7, pp. 1065–1068, 1998.
- [22] H. Kaupang and B. A. J. Angelsen, “A Time Domain Spectral Element Method for Propagation of Pulses in Nonlinear Soft Tissue,” in *Poster session at the IEEE International Ultrasonics Symposium*, 2009.
- [23] M. Tabei, T. D. Mast, and R. C. Waag, “A k-space method for coupled first-order acoustic propagation equations,” *The Journal of the Acoustical Society of America*, vol. 111, no. 1, pp. 53–63, 2002.
- [24] X. Yuan, D. Borup, J. Wiskin, M. Berggren, and S. Johnson, “Simulation of acoustic wave propagation in dispersive media with relaxation losses by using fdtd method with pml absorbing boundary condition,” *Ultrasonics, Ferroelectrics and Frequency Control, IEEE Transactions on*, vol. 46, pp. 14–23, jan 1999.
- [25] A. I. Nachman, J. F. Smith, and R. C. Waag, “An equation for acoustic propagation in inhomogeneous media with relaxation losses,” *The Journal of the Acoustical Society of America*, vol. 88, no. 3, pp. 1584–1595, 1990.
- [26] A. D. Pierce, *Acoustics - An Introduction to Its Physical Principles and Applications*. Acoustical Society of America, Melville, NY, 1994.
- [27] Ø. Standal, T. Tangen, and B. Angelsen, “A phase based approach for estimation and tracking of locally variable delays,” in *Proceedings of the IEEE International Ultrasonics Symposium*, pp. 1583–1585, 2007.
- [28] T.-A. Tangen, *Imaging of nonlinear scattering using dual-frequency band ultrasound*. Phd, Department of Engineering Cybernetics, Norwegian University of Science and Technology, Trondheim, Norway, 2010. ISBN 978-82-471-2518-2.
- [29] W. P. Mason, *Electromechanical Transducers and Wave filters*. D. Van Nostrand Company, Inc, 1948.

- [30] B. N. Taylor and C. E. Kuyatt, “Guidelines for evaluating and expressing the uncertainty of nist measurement results,” 1994. Nat. Inst. Stand. Technol. , Tech. Note, pp. 1-20.

# Design and test of a dual frequency band transducer for extracting nonlinear propagation effects through steel

Tarjei Rommetveit<sup>1</sup>, Tonni F. Johansen<sup>2</sup>, Roy Johnsen<sup>1</sup> and Bjørn Angelsen<sup>2</sup>

<sup>1</sup>Department of Engineering Design and Materials, NTNU, Trondheim, Norway,

<sup>2</sup>Department of Circulation and Medical Imaging, NTNU, Trondheim, Norway

## Abstract

In this work, a dual frequency band transducer that can be utilized for extracting nonlinear propagation effects from low impedance materials through steel is designed and tested through theory, simulations and experiments. The method is based on transmitting a dual frequency pulse complex where the high frequency (HF) pulse is propagating under the influence of the low frequency (LF) pulse. Based on this interaction, a nonlinear delay,  $\tau$ , is obtained from the nonlinear medium beneath steel. The delay opens for a new pulse-echo imaging modality which can isolate the weak echo of interest *in situ* without using any reference signals. This modality aims at suppressing the internal reverberations in the transducer and steel, assuming they are linear, relative to the desired echo which has experienced the nonlinear propagation. The transducer design is based on a bi-layer solution where two piezoelectric layers are stacked on top of each other, resulting in a coaxial solution with common aperture for the two frequency bands. To transmit sufficient LF energy through steel, it is aimed at transmitting a narrowband LF pulse that generates a half wave resonance in the transducer and steel. Results from finite element method simulations and water tank measurements show that approximately plane LF waves are generated in a narrow frequency band which corresponds well to electrical impedance measurements.  $\tau$  is obtained experimentally through steel in the water tank and in pulse-echo mode from a water layer, and it is shown through simulations and measurements how  $\tau$  vary as a function of the water layer thickness. The suggested imaging modality works well, and the unwanted reverberations are considerably suppressed relative to the preferred signal.

Is not included due to copyright

